Process Strategies for Batch Preferential Crystallization

Dissertation
zur Erlangung des akademischen Grades

Doktoringenieur
(Dr.-Ing.)

von: M.Sc., Dipl.-Ing.(FH) Matthias J. Eicke
geb. am: 09. Juli 1979 in Hamburg

genehmigt durch die Fakultät für Verfahrens- und Systemtechnik
der Otto-von-Guericke-Universität Magdeburg

Promotionskommission:

Apl. Prof. Dr. rer. nat. Heike Lorenz	(Vorsitz)
Prof. Dr.-Ing. habil. Dr. h.c. Andreas Seidel-Morgenstern	(Gutachter)
Prof. Dr. Adrian Flood	(Gutachter)
Prof. Dr. rer. nat. Martin Peter Elsner	(Gutachter)

eingereicht am: 04. März 2016
Promotionskolloquium am: 13. Juni 2016

Forschungsberichte aus dem Max-Planck-Institut
für Dynamik komplexer technischer Systeme

Band 47

Matthias J. Eicke

Process Strategies for Batch Preferential Crystallization

Shaker Verlag
Aachen 2016

Bibliographic information published by the Deutsche Nationalbibliothek
The Deutsche Nationalbibliothek lists this publication in the Deutsche Nationalbibliografie; detailed bibliographic data are available in the Internet at http://dnb.d-nb.de.

Zugl.: Magdeburg, Univ., Diss., 2016

Copyright Shaker Verlag 2016
All rights reserved. No part of this publication may be reproduced, stored in a retrieval system, or transmitted, in any form or by any means, electronic, mechanical, photocopying, recording or otherwise, without the prior permission of the publishers.

Printed in Germany.

ISBN 978-3-8440-4896-4
ISSN 1439-4804

Shaker Verlag GmbH • P.O. BOX 101818 • D-52018 Aachen
Phone: 0049/2407/9596-0 • Telefax: 0049/2407/9596-9
Internet: www.shaker.de • e-mail: info@shaker.de

Abstract

An abundance of molecules belongs to the class of chiral compounds that exist in two possible three-dimensional mirrored conformations (enantiomers). Apart from the spatial arrangement they are virtually identical sharing the same physical and chemical properties. Over the course of evolution, nature eventually favored one of two enantiomers of a molecule to build living organisms. This is commonly referred to as homochirality of life. As a consequence, every biological entity is capable to distinguish between enantiomers. This can have fatal consequences especially when chiral molecules are used in pharmaceutical drugs. The most prominent example for such a failure was the thalidomide tragedy, which led to the insight that chiral active pharmaceutical ingredients have to be provided as single enantiomers and not as a 50:50 mixture (racemate). Access is, however, complicated by their identity. It is possible to selectively synthesize one enantiomer by chemical means with significant effort. In many cases the final product has to be in the solid state though requiring additional steps such as crystallization or precipitation.

An alternative strategy is the separation of the racemate. Apart from chromatography, which results in a highly pure but very dilute product stream, crystallization is an attractive process combining separation and solid formation in one step. The enantiomers of a certain class of chiral molecules can be separated by so-called preferential crystallization. This technique allows direct crystallization of single enantiomers from a racemic solution.

The focus of this work is a systematic experimental and theoretical investigation of preferential crystallization. The aim is to increase robustness and yield as well as the optimization of process conditions, which involves the study of novel operating modes.

Kurzreferat

Eine Vielzahl an Molekülen gehört zu der Klasse chiraler Verbindungen, die sich dadurch auszeichnen, dass es jeweils zwei räumliche Anordnungen gibt, die spiegelbildlich zueinander sind. Es handelt sich daher um praktisch identische Moleküle (Enantiomere), die sich lediglich in der dreidimensionalen Anordnung der Atome unterscheiden, ansonsten aber identische physikalische und chemische Eigenschaften besitzen. Im Laufe der Evolution hat sich die Natur bei der Entstehung lebender Organismen letztendlich für eines der möglichen Enantiomere eines solchen chiralen Moleküls entschieden, was gemeinhin als Homochiralität des Lebens bezeichnet wird. Aus diesem Grund sind jegliche biologischen Organismen, so auch der Mensch, in der Lage zwischen Enantiomeren zu unterscheiden. Dies kann fatale Folgen haben, wenn es sich bei den Molekülen um pharmazeutisch aktive Substanzen handelt, wie es bei dem Medikament Thalidomid (Contergan) der Fall war. Es ist daher vor allem in der Pharmaindustrie notwendig reine Enantiomere, anstelle von 50:50 Gemischen beider Moleküle (Racemate) zu verwenden. Der Zugang gestaltet sich aufgrund der Ähnlichkeit jedoch als schwierig. Auf chemischem Weg ist es mit beträchtlichem Aufwand möglich, eines der beiden Spiegelbilder selektiv zu synthetisieren. Letztendlich soll jedoch das Endprodukt

häufig als Feststoff zur weiteren Verarbeitung vorliegen, weshalb zusätzliche Prozessschritte, wie Kristallisation oder Fällung notwendig sind.

Alternativ zur selektiven Synthese reiner Enantiomere gibt es die Möglichkeit, das Racemat durch Trennverfahren zu spalten. Neben der Chromatografie, die zunächst ein hochreines aber stark verdünntes gelöstes Produkt erzeugt, gibt es Kristallisationsverfahren, die in der Lage sind Trennung und Feststoffbildung in einem Prozessschritt zu vereinen. Für eine bestimmte Klasse chiraler Moleküle kann die sogenannte bevorzugte Kristallisation verwendet werden, mit der es möglich ist, aus einer übersättigten racemischen Lösung reines Enantiomer in kristalliner Form zu gewinnen.

Die bevorzugte Kristallisation ist Gegenstand der vorliegenden Arbeit. Im Vordergrund systematischer experimenteller und theoretischer Studien stehen dabei die Erhöhung der Robustheit und Ausbeute, die Optimierung der Prozessbedingungen, sowie die Untersuchung neuartiger Betriebsweisen.

Acknowlegements

The work compiled in this thesis is the result of my rather extensive and rewarding time at the Max Planck Institute for Dynamics of Complex Technical Systems in Magdeburg, Germany. In the summer of 2008 I was given the unique opportunity to move from Hamburg to Magdeburg where I joined the research group Physical and Chemical Foundations of Process Engineering. headed by Andreas Seidel-Morgenstern. There I was able to dive into the interesting topic of preferential crystallization in a truly stimulating and open research environment. I would like to thank Andreas Seidel-Morgenstern for this opportunity and his support throughout the years of my Ph.D.

Having been my immediate supervisor during the first half I thank Martin Peter Elsner for giving me an excellent primer on the topic of crystallization and his time for invaluable discussions. During later stages of my work I could rely on the expertise of Heike Lorenz who kindly agreed to be chair on my defense, which I am very grateful for.

Time would not have been so much fun without a bunch of great colleagues of whom some became very good friends over the years. I thank Luise Borchert for her effort and the good spirit in and outside the lab. Thanks to Jacqueline Kaufmann and Stefanie Leuchtenberg many analyses crucial for this work were done, sometimes on very short notice. I thank the entire PCG group for creating such a good environment, which was not only centered around work.

Special thanks go out to my colleagues Erik, Holger and Guillaume for their friendship and the fun time discussing interesting topics at various locations. At last I thank my parents as well as my brother and his small family for being an anchor to hold on to.

Göttingen, November 6th 2016

Contents

Abstract ... III

Kurzreferat ... III

Nomenclature ... VIII

1 Introduction ... 2

- 1.1 Significance of enantiomers ... 3
- 1.2 Strategies to obtain single enantiomers ... 4
- 1.3 Objectives and outline ... 4

2 Principles of preferential crystallization ... 7

- 2.1 Thermodynamic properties of chiral compounds ... 9
- 2.2 Kinetic properties ... 12
- 2.3 Conventional isothermal batch preferential crystallization ... 16
- 2.4 Coupled isothermal batch preferential crystallization ... 19
- 2.5 Coupling preferential crystallization with selective dissolution ... 20
- 2.6 Preferential crystallization with fines dissolution ... 21
- 2.7 Status of preferential crystallization ... 22

3 Theoretical part ... 23

- 3.1 Modeling and simulation ... 25
  - 3.1.1 Model overview ... 25
  - 3.1.2 The disperse phase ... 27
  - 3.1.3 The continuous phase ... 28
  - 3.1.4 Kinetics formulation ... 30
  - 3.1.5 Moment transformation of the population balance equation ... 32
  - 3.1.6 Numerical aspects ... 33
  - 3.1.7 Balance equations for fines dissolution ... 35
  - 3.1.8 Parameter estimation ... 37
- 3.2 Process control and optimization ... 38
  - 3.2.1 Control objectives ... 38
  - 3.2.2 Symmetry control ... 39
  - 3.2.3 Constant supersaturation control ... 41
  - 3.2.4 Process optimization ... 41
- 3.3 List of model parameters ... 44

4 Experimental part 46
  4.1 Model system DL-threonine-water 48
    4.1.1 Solubility and metastable zone width of threonine 48
  4.2 Plant setup 49
  4.3 Process observation and balancing 51
  4.4 Data logging and process control 53
  4.5 Seed crystal preparation 54
  4.6 Conventional batch operation and general experimental procedures 54
  4.7 Coupled batch operation 55
  4.8 Fines dissolution 56
  4.9 Overview of experiments 57
5 Results and discussion 58
  5.1 Parameter estimation and preliminary simulation study 60
    5.1.1 Parameter estimation 60
    5.1.2 Simulation of conventional PC 68
  5.2 Conventional batch preferential crystallization 72
    5.2.1 Isothermal benchmark experiment 72
    5.2.2 Effect of fines dissolution on conventional PC 74
    5.2.3 Summary of conventional PC experiments 79
  5.3 Coupled batch preferential crystallization 80
    5.3.1 Isothermal benchmark experiment 80
    5.3.2 Comparison of coupled and conventional benchmark experiments 83
    5.3.3 Effect of fines dissolution on coupled PC 83
    5.3.4 Conclusions from the experiments with fines dissolution 85
    5.3.5 Polythermal operation of coupled preferential crystallization 86
  5.4 Control and optimization of coupled batch preferential crystallization 91
    5.4.1 Compensation of initial disturbances through control 91
    5.4.2 Constant supersaturation control 96
    5.4.3 Optimized polythermal operation of CPC 99
  5.5 Coupling preferential crystallization and selective dissolution 107
  5.6 Conclusions and comparison of conventional and improved process strategies 113
  5.7 Results of complementary simulation studies 114
    5.7.1 Limits of conventional and coupled preferential crystallization 114

5.7.2 Limits of coupled preferential crystallization with selective dissolution..... 118
5.7.3 Conclusions from the simulation studies 121
6 Conclusions 124
7 Appendix 130
7.1 Experimental conditions of conventional and coupled PC experiments................. 132
7.2 Experimental conditions of coupled preferential crystallization with dissolution... 134
7.3 Metastable zone width measurements of threonine 135
7.4 Seed crystal size distributions 135
7.5 Model parameters used for the optimization of CPC... 136
7.6 Further analysis of the optimization results 137
7.7 Temperature control during optimized CPC 138
7.8 Product sieve analysis of optimized CPC experiments... 139
7.9 Crystal shape evolution 140
References 142
List of figures 147
List of tables 152
List of publications.. 154
Curriculum vitae.. 156

Nomenclature

α_L	:=	optical rotation angle of the liquid phase	[°]
a_1	:=	parameter of the solubility correlation	[-]
a_1	:=	parameter of the solubility correlation	[-]
$A_{I,norm}$	:=	scaling factor for crystal size distribution	[-]
A_{prim}	:=	coefficient of primary nucleation kinetics	$[m^{-2n\mu 2}]$
A_W	:=	heat exchange area of crystallizer	$[m^2]$
B_{Iprim0}	:=	primary nucleation rate from classical nucleation theory of I	$[s^{-1}]$
B_{Iprim}	:=	primary nucleation rate of component I	$[s^{-1}]$
B_{Isec}	:=	secondary nucleation rate of component I	$[s^{-1}]$
B_I	:=	overall nucleation rate of component I	$[s^{-1}]$
b_{sec}	:=	power-law exponent of secondary nucleation kinetics	[-]
b_{sol}	:=	parameter of the solubility correlation	[-]
C_{IL}	:=	liquid phase concentration of component I	$[kg\ m^{-3}]$
c_{pL}	:=	mean specific heat capacity of threonine solutions	$[J\ kg^{-1}\ K^{-1}]$
d	:=	power-law exponent of dissolution kinetics	[-]
d_{FD}	:=	filter cut-off size	[m]
D_I	:=	dissolution rate of component I	$[m\,s^{-1}]$
e	:=	control deviation	[-]
ee	:=	enantiomeric excess	[-]
E_{Ag}	:=	activation energy for crystal growth	$[kJ\ mol^{-1}]$
E_{Absec}	:=	activation energy for secondary nucleation	$[kJ\ mol^{-1}]$
F_A	:=	analytics flow rate	$[ml\ min^{-1}]$
F_{ex}	:=	solution exchange flow rate	$[ml\ min^{-1}]$
F_{FD}	:=	fines dissolution flow rate	$[ml\ min^{-1}]$
f_{NI}	:=	number density of component I	$[m^{-1}]$
g	:=	power-law exponent of growth kinetics	[-]
G_I	:=	size independent crystal growth rate of component I	$[m\,s^{-1}]$
Δh_{cryst}	:=	specific crystallization enthalpy	$[kJ\ kg^{-1}]$
J	:=	objective function, unit depends on type of optimization	
K_1	:=	parameter of density correlation	$[cm^3\ g^{-1}]$
K_2	:=	parameter of density correlation	$[cm^3\ g^{-1}\ °C^{-2}]$
K_3	:=	parameter of density correlation	$[g\ cm^{-3}]$
k_{bprim1}	:=	pre-exponential coefficient of primary nucleation kinetics	$[m^7 s^{-1} K^{-1} kg^{-7/3}]$
k_{bprim2}	:=	exponential coefficient of primary nucleation kinetics	[-]

k_{bsec0} := pre-exponential coefficient of secondary nucleation kinetics [s^{-1}]

k_{bsec} := rate constant of secondary nucleation kinetics [s^{-1}]

k_d := dissolution rate constant [$m\ s^{-1}$]

k_d := calibration parameter of the density meter [$m^3\ kg^{-1}$]

k_{g0} := pre-exponential coefficient of growth kinetics [$m\ s^{-1}\ s^{ng}$]

k_{pol} := calibration parameter of the polarimeter [1/°]

K_{Tvisc} := viscosity related parameter (primary nucleation) [K]

k_V := volumetric shape factor [-]

k_W := heat transfer coefficient [$J\ (s\ K\ m^2)^{-1}$]

K_{Wvisc} := viscosity related parameter (primary nucleation) [-]

L := maximum length of discretization scheme [m]

m_{IL} := mass of component I in liquid phase [kg]

m_{IS} := mass of component I in solid phase [kg]

$\dot{m}_{IL}$:= mass flow of dissolved component I [$kg\ s^{-1}$]

$\dot{m}_{IS}$:= mass flow of solid component I [$kg\ s^{-1}$]

m_{Iseeds} := mass of seeds of component I [kg]

m_{sol} := parameter of the solubility correlation [$°C^{-1}$]

μ_{iI} := i^{th} moment of the crystal size distribution of comp. I, i = 0…3 [m^i]

N_{dat} := number of measurement points [-]

N_{exp} := number of experiments [-]

n_{bsec} := parameter of stirrer speed correlation of sec. nucl. kinetics [$rad\ s^{-1}$]

n_g := exponent of stirrer speed correlation in growth kinetics [-]

$n_{\mu 2}$:= exponent of second moment dependency (primary nucleation) [-]

$n_{\mu 3}$:= exponent of third moment dependency (secondary nucleation) [-]

N_{St} := stirrer speed [min^{-1}]

Pr_I := productivity with respect to component I [$g\ kg^{-1}\ h^{-1}$]

Pr_{Iw} := weighted productivity with respect to component I [$g\ kg^{-1}\ h^{-1}$]

Pu_I := purity of solid component I [%], [-]

ρ_L := density of liquid phase [$kg\,m^{-3}$]

R := gas constant [$J\ mol^{-1}\ K^{-1}$]

R_{FD} := S-shaped function of fines dissolution filter cut-off [-]

σ_I := standard deviation of log-normal distribution [-]

S_I := supersaturation of component I [-]

T_{cryst} := crystallization temperature [K], [°C]

T_L := liquid phase temperature [K], [°C]

u_{FD} := flow velocity of suspension in fines dissolution unit [$m\ s^{-1}$]

V_{cryst} := volume of a single crystal [m^3]

$\dot{V}_{ex}$:= volumetric exchange flow rate [$m^3\ s^{-1}$]

$\dot{V}_{FD}$:= volumetric fines dissolution flow rate [$m^3\ s^{-1}$]

V_L := liquid phase volume [m^3]

V_S := solid phase volume [m^3]

w_{IL} := mass fraction of component I in liquid phase [$kg_{solute}/kg_{solution}$]

Y_I := relative yield of component I [%], [-]

z_1 := characteristic size (length) [m]

z_2 := characteristic size (width) [m]

$\bar{z}_I$:= mean crystal size of component I [m]

$\bar{z}_{I,seeds}$:= median of the seed crystal size distribution of component I [m]

Subscripts

0 := initial condition (unless subscript of kinetics parameters)

A := analytics

cs := control sample

E1 := enantiomer 1 (L-threonine)

E2 := enantiomer 2 (D-threonine)

eq := equilibrium

ex := exchange path of coupled crystallizers

FD := fines dissolution

H2O := water (solvent)

I := component I = E1, E2

in := inlet of a subsystem

L := liquid phase

out := outlet of a subsystem

prim := primary nucleation

rac := racemate

sec := secondary nucleation

seeds := seeds

S := solid phase

tot := total amount of a quantity or component

w := setpoint (except when in Pr_w)

Superscripts

k := denotes preferred or counter enantiomer, k = p, c

j := subsystem Tank 1, Tank 2 or fines dissolution unit, j = T1, T2, FD

T1 := Tank 1

T2 := Tank 2

Abbreviations

CPC	coupled preferential crystallization
CPC-D	coupled preferential crystallization with selective dissolution
CSD	crystal size distribution
MZW	metastable zone width
PC	conventional preferential crystallization in one crystallizer

1 Introduction

1.1 Significance of enantiomers

An abundance of molecules contains atoms with four different substituents bonded to them. Such atoms are called chiral centers or asymmetric atoms and result in the existence of two possible three-dimensional arrangements of the four different groups around them. These two molecular conformations are mirror images of each other and possess identical physical and chemical properties. Up to now, the reasons and origins are unknown but nature seems to have a tendency to favor one of the possible spatial arrangements. Proteins, for example, consist almost exclusively of L-amino acids, although there are exceptions (Kreil (1997)). The backbone of the genetic information, the DNA, is entirely made of D-deoxyribonucleic acid and not the L-form. At some point an evolutionary decision was apparently made to build life preferably based on one kind of molecule, which is known as the homochirality of life (Meierhenrich (2008), Podlech (2001)).

As a consequence, every biological organism is able to distinguish between the enantiomers of a chiral molecule. Their existence poses a challenge, especially to medical health care, where pharmaceutical drugs are often required for the treatment of an illness. Many active pharmaceutical ingredients (API) are chiral molecules. Because living organisms discriminate between the three-dimensional mirror images, each enantiomer may lead to different biochemical responses. Three examples are given in Figure 1.1. The enantiomers of carvone (a) and limonene (b) have distinct odors, indicated below each molecule. When used in fragrances, it is thus important to have access to only one of the two species.

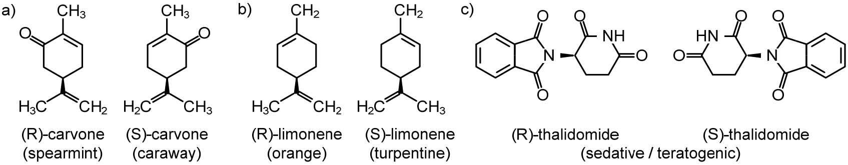

Figure 1.1: Examples of chiral molecules and their different effects in biological organisms.

The third molecule, thalidomide (Figure 1.1c), is far more critical and is probably the most prominent example of an API that resulted in severe side effects. It was initially intended as a sedative and for treating nausea of pregnant women but was soon identified to be the cause of birth defects. Due to its chirality, it was assumed that only one of the enantiomers, namely the S-isomer, was responsible for the teratogenicity that led to the deformations of extremities of the born children. However, it was later shown that thalidomide undergoes rapid racemization in the body, which results in the conversion of one enantiomer into the other, creating a racemic 50:50 mixture. As of now it is thus impossible to clearly attribute the teratogenic effect to a single enantiomer of thalidomide (Ito, et al. (2011)). Still, the thalidomide tragedy led to the insight that chiral APIs have to be investigated even more rigorously and provided as single enantiomers, unless it is beyond doubt that the racemate has no adverse effects. Therefore, it had strong implications on the development and manufacturing of new drugs. Nowadays, most chiral APIs are sold only in their enantiopure form (Agranat, et al. (2002)). Apart from pharmaceutical companies, other branches such as food and agrochemical industries face the same challenge. In almost all cases where chiral molecules are involved, it is necessary to gain access to the pure enantiomers. Since there is no single method of choice for every chiral molecule, it is important to have an array of different techniques that can perform the task.

1.2 Strategies to obtain single enantiomers

Generally there are two overall possibilities to obtain pure enantiomers (Lorenz, et al. (2014)). One is the stereoselective production, which can involve a selective chemical synthesis or the use of bioprocesses. These techniques directly yield the target enantiomer. In case of microbial fermentation processes, it is the homochirality of life that results in the specific formation of one enantiomer. The second possibility aims at separating the racemate, i.e. the 50:50 or equimolar mixture of enantiomers. The approach is complicated by the identical physical and chemical properties of enantiomers in an *achiral* environment. A very powerful and versatile technique is chromatography, which can perform complex separation tasks. It can be regarded as the last option when other techniques fail. However, the product stream is dilute, requiring additional enrichment steps. Other separation processes involve the use of membranes or enzymatically catalyzed resolutions that may also require subsequent steps.

Among the processes directed at the separation of enantiomers, crystallization is an attractive option because it combines separation and solid formation in one process step (Coquerel (2007)). The most widely used method known as *classical resolution* relies on the formation of diastereomers, which are the product of a chemical reaction between the enantiomers and an additional chiral molecule. The two diastereomeric salts no longer possess identical properties – particularly in terms of solubility – and can thus be readily separated by crystallization in a very robust process. A requirement for this option is, however, the availability of an enantiopure resolving agent that can react with the enantiomers.

The challenge of a crystallization based separation of enantiomers lies not only in the identical properties of the two species regarding solubility and kinetics. It is also due to the different possible solid-liquid equilibria of the ternary system consisting of the two molecules and the solvent (see chapter 2). Most enantiomeric systems belong to the compound forming type (Jacques, et al. (1981)), which cannot be directly separated by crystallization; they require a preceding enrichment of the racemate. A certain type, however, i.e. conglomerate forming systems, allows the use of preferential crystallization, which does not involve any resolving agents or other means to break the symmetry. The only requirement is the availability of crystals of the preferred enantiomer. Subsequently, a single enantiomer can be directly crystallized from a racemic solution. Preferential crystallization is therefore a very easy and efficient separation process that still has a large potential for improvements.

1.3 Objectives and outline

The subject of this work is a systematic experimental and theoretical investigation of process strategies to obtain pure enantiomers from a racemic mixture by batch preferential crystallization. Although being mainly limited to conglomerate forming systems, it is an attractive alternative for the separation of this class of chiral molecules due to the simplicity of the required equipment.

The aim is to study preferential crystallization from a process engineering point of view to improve robustness and productivity. The coupling of crystallizers, for example, has been the subject of previous studies by Elsner, et al. (2009) that showed great benefit. Herein, this improvement will be particularly emphasized on as a logical and simple improvement of preferential crystallization enabling advanced process operations.

The amino acid threonine representing conglomerate forming systems will be employed to study three different process strategies.

First, preferential crystallization will be investigated in its simplest implementation using a single crystallizer since this process strategy clearly demonstrates the challenge of purifying a 50:50 mixture of molecules sharing identical properties. Although being the least favorable option in terms of yield and robustness, it is the easiest to handle experimentally. Its investigation will cover means to extend the limited time span available for production of pure enantiomers.

The second strategy exploits the benefits of crystallizing the enantiomers in separate vessels connected only via the liquid phase. This work aims at significantly enhancing yield and productivity of coupled preferential crystallization by investigating polythermal operation and different control strategies developed in collaboration with the group of Prof. Jörg Raisch at the Technical University, Berlin. Ultimately, a dynamic optimization is done to reveal the full potential of this process but also to test a theoretical model.

The third process strategy can be regarded as a combination of the previous two. It exploits the coupling of two crystallizers that are, however, operated at different temperatures. Preferential crystallization is carried out in a vessel while constantly circulating the solution through another containing saturated racemic suspension. Through selective dissolution of the crystallizing enantiomer from the solid racemate it is possible to obtain two pure enantiomers. The advantage of coupled preferential crystallization with selective dissolution is the need of only one pure enantiomer. The downside is the chance of nucleation of the impurity under productive process conditions. However, it will be shown that it is superior over conventional preferential crystallization in one vessel.

The experimental and theoretical investigations presented in this work attempt to contribute to a better understanding of the possibilities and limitations of preferential crystallization of conglomerate forming systems. It is shown that this separation process can be significantly improved in terms of yield, productivity and robustness by employing different strategies to connect and operate standard equipment. The experimental results also provide new data for further improvement of the theoretical model, which is used to provide a more general understanding of the advanced coupled processes by identifying optimal operating regions.

The subsequent parts of this work are organized as follows.

Chapter 2 introduces basic aspects of crystallization such as different types of solid-liquid equilibria and the kinetic phenomena involved in the phase change from liquid to solid. These general considerations are followed by a description of the three investigated process strategies. Finally a brief overview of other possibilities to perform preferential crystallization is given.

The first part of chapter 3 covers the population balance model used for the simulation of the processes as well as the numerical procedure employed for parameter estimation. The second part is devoted to the control and optimization procedures and outlines the control concepts developed in the group of Prof. Jörg Raisch (Technical University, Berlin). A detailed account on these will be available in the dissertation of Steffen Hofmann.

Chapter 4 describes Materials and Methods.

The innovative core of this work is found in chapter 5, which first covers parameter estimation using experimental data of selected processes. Subsequently, results of the three process strategies are discussed in detail. The last section returns to theoretical investigations and comparisons providing a broader picture of the enantioselective resolution processes. Chapter 6 summarizes the main results and concludes this work.

2 Principles of preferential crystallization

2.1 Thermodynamic properties of chiral compounds

Every pair of enantiomers can be assigned to one of three known general types, based on their binary melting point phase diagrams (Jacques, et al. (1981)). In Figure 2.1, the three known solid liquid equilibria (SLE) of mixtures of two arbitrary enantiomers E1 and E2 are depicted. The most abundant are of the conglomerate and the compound forming type (Figure 2.1a, b respectively), whereas the latter is commonly estimated to make up more than 90% of all enantiomeric systems (Collet (1999)).

Conglomerate forming systems (Figure 2.1a) exhibit a single eutectic point. It corresponds to a minimum in melting temperature T, which occurs at equimolar (racemic) composition of the mixture, i.e. when the molar fractions are identical ($x_{E1} = x_{E2}$). Below the eutectic temperature T_e, only solid exists. A characteristic property of conglomerates is their complete chiral discrimination in the solid state. As a consequence, each crystal consists of one enantiomer only, solid E1 or solid E2 (E1(S), E2(S) in Figure 2.1). In principle, it would thus be possible to separate the enantiomers by mechanical means such as sieving or manual sorting as done by Louis Pasteur (Pasteur (1848)). Above temperature T_e, two scenarios are possible. The system either consists of a single phase (the area above the liquidus curve), or it can enter one of the two regions enclosed by the liquidus and solidus curves, in which two phases, solid and liquid, coexist.

If temperature T is higher than the melting point T_m of either one of the pure enantiomers, any composition x_{E1} yields a single phase. Below T_m, the composition, which still yields a single molten phase, is restricted by the liquidus curve. Upon entering a two-phase region, the equilibrium composition of the melt travels along the liquidus curve as the temperature is further decreased towards T_e. The initial enantiomeric excess of the melt determines which one of the two enantiomers crystallizes first. When the eutectic temperature is reached, the less abundant enantiomer enters the solid state as well. For a melt of racemic composition, both enantiomers start to crystallize simultaneously at the minimum melting point T_e. Exactly at the eutectic point, two solid phases are in equilibrium with the racemic melt.

The situation becomes more complicated in case of *compound forming systems* (Figure 2.1b), as they can form three distinct solid phases.

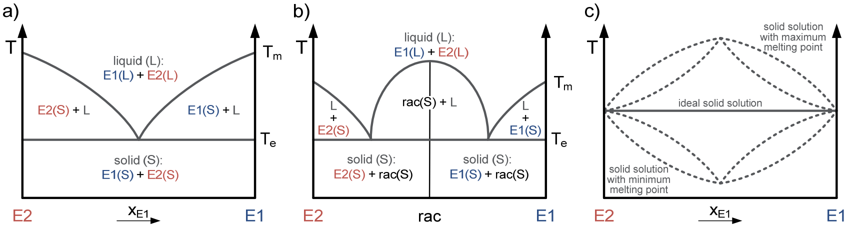

Figure 2.1: Binary melting point phase diagrams of the three known general systems: a) conglomerate, b) racemic compound, c) solid solution (pseudoracemate) of Roozeboom Type I (ideal solid solution), Type II (maximum melting point at racemic composition) and Type III (minimum melting point at racemic composition).

Apart from the two pure enantiomers E1 and E2, a third compound appears in the solid state at equimolar composition – the racemic compound. Its crystal lattice is composed of equal amounts of E1 and E2. This is in contrast to conglomerates, where the solid state is merely a physical mixture of separate, homochiral crystals. For this reason, compound forming systems are sometimes called true racemates. The binary phase diagram of a compound forming system contains an additional two-phase region around the racemic composition, where crystals of the compound are in equilibrium with the melt. The extent of this region depends on the melting point of the racemic compound. In some cases, where it is significantly lower than the melting point of the pure enantiomers, the region can be very small, making it difficult to identify the system as being of a compound forming type. The existence of the racemic compound has profound implications on the applicability of preferential crystallization, as we will discuss briefly in subsequent paragraphs.

The third type of system, termed *pseudoracemate* (Figure 2.1c), is rarely encountered. In this case, the enantiomers form a solid solution, resulting in crystals of varying composition. They are completely miscible in both, the liquid and the solid state over the entire range of composition. Although the solid phase can be racemic, both molecules are distributed statistically in the crystal lattice. As a result, a small fragment of an otherwise racemic crystal might not necessarily contain equal amounts of both enantiomers, unlike crystals belonging to the compound forming type. There are three different kinds of pseudoracemates, which were identified by Bakhuis-Roozeboom (1899). When any mixture of both enantiomers solidifies (or melts) at the same temperature, the solid solution is ideal. Apart from that, a maximum or minimum melting point can occur at racemic composition. For the remainder of this work, solid solutions are neglected, since they cannot be separated by preferential crystallization.

Based on the binary melting point phase diagrams, we can conclude that a prerequisite for applying preferential crystallization is immiscibility in the solid state (complete or at least partial). Since this work addresses crystallization from solution, it is necessary to further consider the enantiomeric systems in the presence of a third component – the solvent. For the sake of clarity, we shall first consider the solubility of one enantiomer in a solvent at a given temperature.

In the binary solubility diagram, illustrated schematically in Figure 2.2, the black curve represents the dependence of solubility (expressed in terms of liquid phase mass fraction w_L) on temperature T. To the right of the solubility curve, e.g. at point A, any solution is undersaturated and therefore stable. By lowering the temperature in such a way that the new state is represented by point B, the solution becomes saturated. Adding pure, solid enantiomer at this point, does not change the state of the solution. Further subcooling yields a supersaturated liquid (point C). At this temperature, the equilibrium composition has shifted to point C’ on the solubility curve. There is however a region between the solubility curve and the metastable border, in which the solution is supersaturated but remains clear. It is referred to as the metastable zone, where crystallization is kinetically inhibited (see section 2.2). Subcooling beyond the metastable border (e.g., to point D), results in an immediate phase separation until the new equilibrium composition of the liquid phase is reached (point D’).

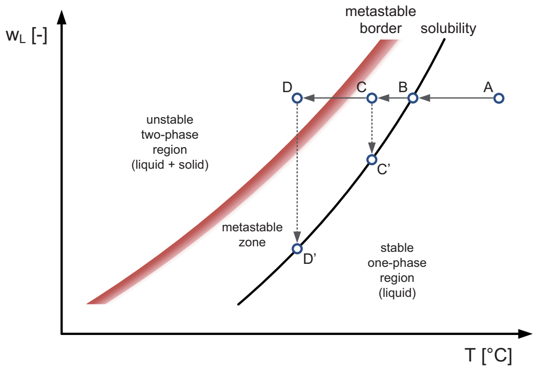
w$_L$ [-]
metastable border
solubility
D
C
B
A
unstable two-phase region (liquid + solid)
C'
metastable zone
D'
stable one-phase region (liquid)
T [°C]

Figure 2.2: Schematic representation of a solubility diagram for a binary system, consisting of solute and solvent.

It should be kept in mind that the diagram in Figure 2.2 represents only a small region of the entire phase diagram of solute and solvent, namely the part which is of importance for cooling crystallization from solution.

In order to understand the thermodynamic behavior of a mixture of both enantiomers and the solvent, we have to combine the information contained in the binary melting point phase diagram (Figure 2.1) and the solubility diagrams (Figure 2.2) of each enantiomer. A convenient way to visualize the solid liquid equilibria of these ternary mixtures, is shown in Figure 2.3. Considered are the ternary phase diagrams of a conglomerate (a) and a compound forming system (b). Each vertex of the equilateral triangles represents a pure component: the enantiomers E1 and E2 and the solvent sol. A ternary mixture results in a point inside the diagram, while a binary mixture is represented by a point on one of the sides. The composition is usually given in terms of mole or mass fractions.

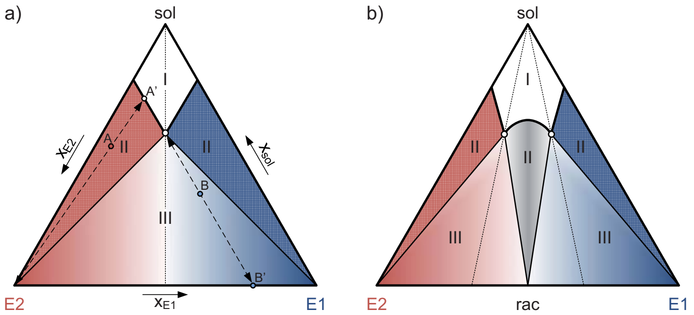
a)
sol
I
A'
A
II
II
x$_{E2}$
x$_{sol}$
B
III
B'
E2
x$_{E1}$
E1
b)
sol
I
II
II
II
III
III
E2
rac
E1

Figure 2.3: Ternary phase diagram of a conglomerate (a) and a compound forming system (b). The dotted lines represent the eutectic compositions. The number of coexisting phases in each region is indicated by Roman numerals.

For a *conglomerate forming system* (Figure 2.3a), the solubility diagram is divided into four regions. Above the solubility isotherm (bold black line), a clear solution is obtained. Below the isotherm, three different solid liquid equilibria are possible. A solution enriched with enantiomer E2 (point A) can, upon subcooling, enter the two-phase region on the left, in which pure solid E2 crystallizes. The resulting liquid phase has a composition represented by point A'. Solutions in the three-phase region will always partition into a liquid phase of eutectic composition (here racemic) and two solid phases composed of pure E1 and E2. If the initial solution were represented by point B, the solid phase would have a composition B'. Usually, the raw material for preferential crystallization has no enantiomeric excess. Subcooling such a solution, yields solid and liquid of racemic composition at equilibrium.

Compound forming systems (Figure 2.3b) show five different equilibrium states, due to the existence of the racemic compound and the two resulting eutectic points. Contrary to conglomerates, the eutectic compositions are not racemic but lie on lines with a certain enantiomeric excess, which is specific for the respective molecule. The ratio between E1 and E2 at eutectic composition is not necessarily constant. Some systems show a temperature dependency, which gives rise to interesting separation strategies (Kaemmerer, et al. (2009), Lorenz, et al. (2013)).

It is obvious from the solubility diagram of a compound forming system, that a racemic solution will always yield the racemic compound in the solid phase. To the left and the right of the central two-phase region, one can either obtain a physical mixture of one of the pure enantiomers and the compound or, when entering the two-phase regions located to the far left and right, pure E1 or E2. In order to reach the three-phase regions, a preceding enrichment is necessary.

The investigation of the thermodynamic properties is an important step towards the design of a separation process. Knowledge about the type of a ternary system is crucial, when preferential crystallization is to be applied. Once a conglomerate forming system has been identified, the chances are high that preferential crystallization can lead to a successful separation. If, however, a compound is detected, resolution is more challenging, because an additional enrichment is mandatory to leave the two-phase region, in which only the racemic compound crystallizes.

Apart from knowing the type of system, it is usually important to obtain detailed information on the solubility of the enantiomers in the respective solvent. Not only does this allow for an estimate of the possible yield under certain operating conditions such as temperature or initial concentration. It is also important due to practical reasons, as the solubility dictates the temperatures that have to be chosen to prevent encrustation in peripheral equipment around the crystallizer.

2.2 Kinetic properties

Thermodynamics defines the final state of a process but contains no information about the path leading to equilibrium. Trajectories of the state of a process towards equilibrium are influenced by kinetics, which is the key to successful preferential crystallization. The main goal is to achieve an enrichment in the solid phase with respect to the product. Several mechanisms lead to the creation and growth of crystals from a solution or melt. Figure 2.4 is intended to give a simplified overview of the main processes involved in the complex phase transition taking place during crystallization and its counterpart, dissolution.

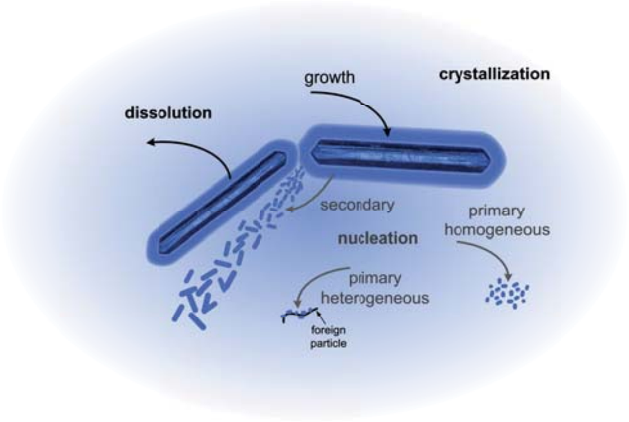

Figure 2.4: Crystallization consists of two major processes. Nucleation is responsible for the appearance of the new solid phase from a clear solution. Growth is the process by which the addition of solute molecules to the existing solid phase results in an increase in particle size. Dissolution can be considered as the opposite and eventually causes the disappearance of the solid phase.

Starting from a clear solution, represented by some point in the one-phase region of either Figure 2.2 or Figure 2.3, crystallization can be induced by cooling below the saturation temperature. By doing so, supersaturation is created, which acts as the driving force for crystallization. According to thermodynamics, such a solution should instantaneously reacquire equilibrium, by depositing the dissolved excess in the solid phase, since a single phase is an unstable state below saturation temperature for most systems. This, however, does not happen immediately, because the rate of solid formation is finite. Depending on the kind of molecule, solvent, the degree of supersaturation, temperature, power input by agitation as well as the vessel size and geometry, the system remains in a metastable state for a certain amount of time, because kinetics inhibit the phase transition. Only because of this phenomenon, can preferential crystallization be used to resolve a mixture of two enantiomers.

At some point, most supersaturated systems crystallize spontaneously by a pronounced nucleation shower, during which a high number of particles is created. What exactly happens, just before and during this event, is still not entirely understood. Classical nucleation theory has been widely used, to quantify the spontaneous (liquid to solid) phase transition of various systems. Its applicability to preferential crystallization is discussed in later sections of this work.

Given a supersaturated solution, a new solid phase appears, in the absence of any solid surface, due to *primary homogeneous nucleation* (cf. Figure 2.4). It is most likely to be caused by minor fluctuations in the local density of the solute in solution that can lead to the formation of clusters (Kashchiev, et al. (2003)). In a stagnant homogeneous solution, a solute molecule travels through the bulk phase in a stochastic manner due to Brownian motion. Random collisions of two or more molecules, result in the transient appearance of such clusters, which immediately vanish, unless they reach a certain size (Mullin (2001)). Figure 2.5 depicts the thermodynamic basis of classical nucleation theory (CNT) (Volmer, et al.

(1926)). The overall free energy ΔG of a cluster depends on its size d, which can be the diameter assuming a spherical shape at the very early stage of nucleation. According to classical nucleation theory, the overall free energy ΔG determines the size, at which a cluster becomes stable and thus, whether nucleation leads to the new solid phase or not. It consists of two contributions: surface free energy ΔG_A and volume free energy ΔG_V.

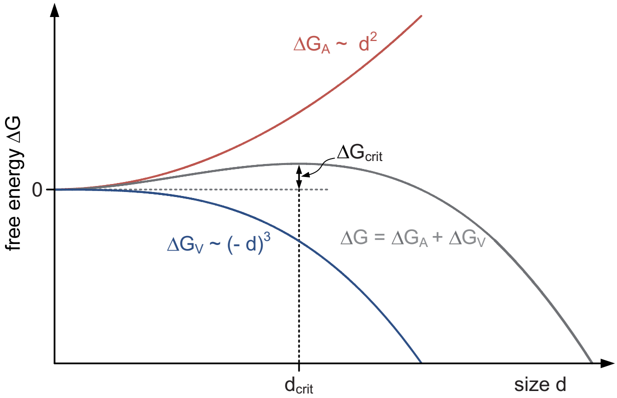

Figure 2.5: Change of the overall free energy ΔG as a function of cluster size d for homogeneous nucleation.

As the surface extents, ΔG_A increases proportionally to the square of the cluster diameter. This can be illustrated in the sense that more and more molecules take an energetically unfavorable position at the interface between liquid and solid phase. Alternatively, one could think of energy being spent, in order to perform the work needed to build the surface and overcome the force of the surface tension.

In contrast, the volume free energy ΔG_V decreases proportionally to the cube of the cluster diameter. It can be conjectured that, as molecules are incorporated into the bulk of the cluster, they attain a lower energy level, as the number of neighboring species is maximized.

The opposing trends of both, ΔG_A and ΔG_V result in a maximum in overall free energy at ΔG_{crit}, which represents the energy barrier that has to be overcome for primary nucleation to proceed spontaneously. Just above the critical size, denoted as d_{crit} in Figure 2.5, the formed clusters are stable and can further grow, because the overall free energy ΔG is minimized from this point forward. At an infinitesimally smaller diameter than d_{crit}, the clusters disappear, since ΔG has a negative slope in this direction as well. The disappearance, or dissolution, of clusters below the critical diameter can be explained by the Gibbs-Thomson relation (also referred to as Ostwald-Freundlich relation), which essentially states that small particles have a higher solubility than larger ones (Mullin (2001), Nývlt (1985)).

So far, nucleation was considered in the absence of any additional solid surface. Usually, this is difficult to realize in a laboratory, since foreign, insoluble particles, like dust, will almost always be present in a solution next to the solvent and solute. This undefined matrix can promote *primary heterogeneous nucleation*. Similarly to the homogeneous case, clusters have to overcome an energy barrier ΔG_{crit} to grow beyond a critical size. However, this barrier is much lower, because the heterogeneous surface can catalyze the formation of clusters. Therefore, heterogeneous nucleation also occurs at lower levels of supersaturation (Mullin (2001)).

The third mechanism responsible for the creation of new particles is *secondary nucleation*. It occurs at even lower degrees of supersaturation than heterogeneous nucleation and requires the presence of crystals of the solute itself. As Figure 2.4 suggests, it can be induced by collisions of crystals , during which clusters or cluster-like units are torn out of the boundary layer that surrounds each crystal (Mullin (2001)). Depending on their size, they will either dissolve after they enter the bulk solution ($d < d_{crit}$), or they can act as nuclei that further develop into new crystals ($d > d_{crit}$). Collisions of crystals with the stirrer, crystallizer wall or any other installed equipment can produce the same effect. On a much larger scale, crystal breakage and attrition also lead to an increase in particle number. Although the term nucleation suggests the creation of minute structures, the formation of macroscopic fragments, resulting from the aforementioned events, is assigned to secondary nucleation as well.

After the creation of a new solid phase the individual particles increase in size due to *crystal growth*. In general, this requires solute molecules (or growth units) to first be transported towards the boundary layer at the interface between the crystal surface and the surrounding solution. Subsequently they have to travel through the layer by diffusion and eventually “find” an energetically favorable site on the crystal surface to which they can bind and thus be integrated into the crystal lattice.

There are different theories to explain and also mathematically describe the mechanisms involved in crystal growth. Nyvlt (Nývlt (1985)) distinguishes between two major groups with various degrees of detail. The first group contains theories that try to derive the final crystal shape based on thermodynamic considerations. A crystal at equilibrium with the surrounding fluid phase will have undergone a minimization of its total surface free energy, which results in a specific final crystal habit. By changing the system state, e.g. by generation of supersaturation, the crystal will regain equilibrium through attachment of growth units to those crystal faces that provide a maximum release of energy. The rate at which the specific equilibrium shape is assumed is, however, not captured by these theories. They are therefore not suitable for the calculation of growth rates.

The second group of theories accounts for the influence of external parameters, such as supersaturation, temperature and hydrodynamics of the fluid phase on the rate, at which crystals evolve. Among these are theories that postulate mechanisms about how favorable attachment sites on the crystal surface appear and propagate. The underlying assumption is the successive growth of layers that provide these sites in the form of steps and kinks. According to the birth and spread model, a two-dimensional nucleation event on the surface is necessary to provide an initial starting point for further growth of such layers. A problem of the models involving such surface nucleation events is, however, their failure to predict growth rates at low levels of supersaturation, which are common during seeded, and particularly preferential crystallization.

The Burton-Cabrera-Frank model (Burton, et al. (1951)) tries to circumvent this difficulty by postulating a screw dislocation mechanism. It essentially results in a spiral staircase on the crystal surface that continuously provides steps to which new molecules can attach. An extension of the BCF model was done, e.g. by Chernov (Nývlt (1985)) to account for the possibility that the integration of molecules into the crystal lattice is not the only rate determining step during growth. Apart from the screw dislocation mechanism, it additionally considers the presence of a boundary layer around the crystal surface, through which molecules have to diffuse prior to being attached to the surface. As a result, this type of model is more applicable to describe crystallization from solution since such bulk diffusion is likely to be the limiting factor. A much simpler approach than the aforementioned theories is the diffusion layer model. It refrains from postulating any specific surface mechanism but rather approximates the integration step by a power law, which links the rate of mass deposition on the crystal to a concentration gradient. Mass transport towards the crystal surface by diffusion through the boundary layer is approximated by Fick's first law, which in the end yields a model containing two resistances in series, i.e. diffusion and integration.

The above mentioned theories represent mechanistic approaches in the sense that they postulate a mechanism (surface nucleation, screw dislocation) and provide a mathematical model, able to quantify the evolution of a crystal surface. Although crystals might grow according to one of these mechanisms under ideal conditions (e.g., a perfect crystal floating in a stagnant, supersaturated, homogeneous solution without any impurities), bulk crystallization in a stirred tank reactor will likely proceed by a combination of many different phenomena. As crystals experience abrasion and breakage, their surfaces might differ significantly from those on the same, but perfectly grown, type of crystal. As a consequence, the way new growth units attach to such imperfect crystals can hardly be put into a deterministic mathematical framework unless considerable efforts are made.

Despite the complexity of crystallization with all the involved sub-processes leading to the creation of a solid phase, it is still possible to describe bulk crystallization with reasonable accuracy without a detailed knowledge of the mechanisms. The mathematical model addressed in chapter 3 rests on empirical equations to account for nucleation and growth kinetics which is sufficient to simulate the process strategies investigated in this work.

2.3 Conventional isothermal batch preferential crystallization

In order to understand enantioseparation by preferential crystallization (PC), we first consider the simplest process strategy, which involves a single crystallizer, operated under isothermal conditions. Subsequently, it shall serve as a benchmark for the more advanced concepts. In this work, we define that the temperature trajectory *after* seeding determines whether the process is iso- or polythermal. Furthermore, we denote the unseeded species as the counter and the seeded as the preferred enantiomer. After preparation of a racemic solution, PC essentially consists of the following three stages and events, which are schematically depicted in Figure 2.6:

- generation of supersaturation (here by supercooling)
    - t_0: seeding with crystals of the target enantiomer

- crystallization of the target enantiomer
    - t_1: nucleation of the counter enantiomer (impurity)
- crystallization of both enantiomers
    - t_∞: thermodynamic equilibrium

The initial degree of supercooling has to be chosen carefully to avoid spontaneous, unspecific nucleation, which happens when the metastable zone width is exceeded. As mentioned in the previous sections, it is specific for every molecule/solvent combination and also depends on the cooling rate, the reactor geometry, installed equipment and fluid dynamics.

Once, a metastable racemic solution has been created, the addition of enantiopure (homochiral) seed crystals of the preferred enantiomer (here E1) at t_0 initiates preferential crystallization. Pure product accumulates in the solid phase due to crystal growth and secondary nucleation until the process is disturbed by the onset of nucleation of the unseeded enantiomer E2 at t_1. Subsequently, both molecules crystallize, until the supersaturation is depleted, leaving a saturated racemic solution and a nearly racemic solid phase (t_∞).

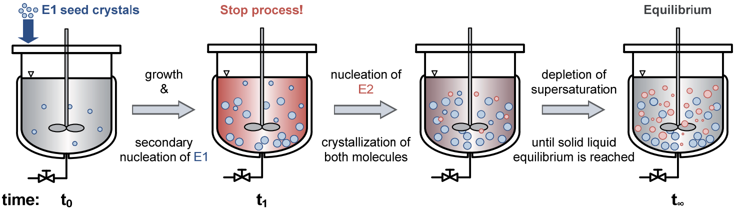
E1 seed crystals
Stop process!
Equilibrium
growth &
secondary nucleation of E1
nucleation of E2
crystallization of both molecules
depletion of supersaturation
until solid liquid equilibrium is reached
time: t_0
t_1
t_∞

Figure 2.6: Principle of preferential crystallization. From t_0 to t_1, pure E1 can be obtained. Nucleation of the counter enantiomer E2 occurs just after t_1, which leads to a gradual contamination of the product until the new equilibrium is reached.

In order to prevent product contamination by the counter enantiomer, the process has to be stopped by separating the obtained crystals from the solution at or just before t_1. This is usually done by filtration and washing of the filter cake to remove any adhering mother liquor, which would otherwise evaporate and cause nucleation of the counter enantiomer. Unfortunately, the induction period $\Delta t_{ind} \approx t_1 - t_0$, i.e. the time required for the unseeded enantiomer to nucleate, cannot be reliably predicted, due to the stochastic nature of this event. A rough estimate can be made by performing a series of identical experiments that are long enough to reveal the onset of E2-nucleation. By doing so, one can obtain mean induction times for specific operating conditions if the number of repetitions is sufficiently large. However, if the process is changed by any means, these values might not be valid anymore.

The fact, that the unseeded enantiomer shares identical properties with the product and makes up 50% of the raw material, imposes strong limitations on the process. By nature, the maximum theoretically attainable yield is 50% if one were able to crystallize the entire target enantiomer from the initial solution. Practically, the yield can take on values between 2% and 25% considering crystallization from solution. It is first and foremost restricted by the metastable zone width and thus by the nucleation of the counter enantiomer. These are the basic but also most difficult challenges of preferential crystallization. Others, which are, however, of no importance for the substance system considered here (see chapter 4.1), can be the occurrence of polymorphs or solvates, as well as the appearance of a metastable compound. In order to illustrate the basic challenges, we consider a typical isothermal preferential crystallization process as depicted in Figure 2.7. At t_0 in Figure 2.7a, the racemic, supersaturated solution is seeded with E1 crystals. Compared to the entire duration of the process, that is, until the new equilibrium is reached at t_∞, only a short period is available to produce pure E1 crystals. At t_1, the counter enantiomer E2 nucleates, while a large amount of E1 is still dissolved.

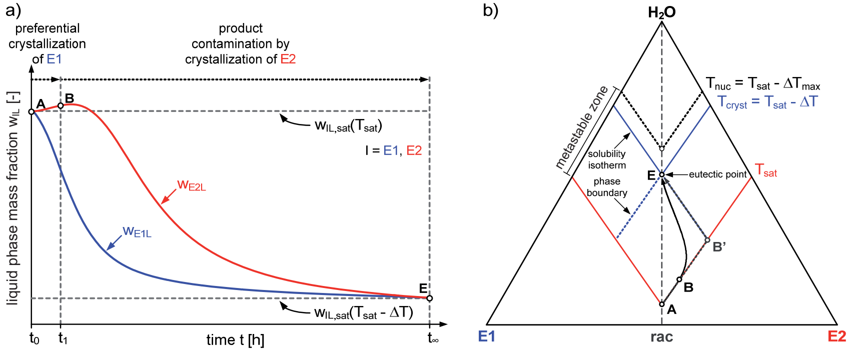

Figure 2.7: Typical time trend of the liquid mass fractions of the seeded (E1, blue) and unseeded (E2, red) enantiomers (a) and the corresponding trajectory in a small region of the ternary phase diagram (b).

The resulting trajectory in a small region close to the solvent corner of the ternary phase diagram is shown in Figure 2.7b. From point A to B, only E1 crystallizes. After E2 nucleates, the trajectory is immediately diverted to the common attractor, the eutectic point E. Ideally, the composition would change from A to E via point B', which corresponds to the metastable solubility of enantiomer E1. In this case, the maximum possible yield, with respect to the seeded species, at the chosen temperature T_{cryst}, would be obtained, if the process were stopped at B'. Whether or not this point can be reached also depends on how fast the seeded enantiomer can crystallize; apart from the metastable zone width (or the induction time for nucleation). In general it is therefore beneficial to provide a large solid surface, either by increasing the mass of seeds or by reducing the seed size. However, this might be in conflict with product quality specifications. Although smaller seeds allow for faster crystallization, they might not be able to grow to the desired size, given the relatively short time until the counter enantiomer nucleates. It is therefore imperative to provide alternative process strategies that offer a wider operating window.

In the following chapters, we will look at options to improve the performance of PC. The main goal is to increase the yield obtained in a single batch run and, at the same time, reduce the risk of nucleation. At first, we consider an expansion of the process setup by integrating an additional crystallizer, followed by the introduction of an external fines dissolution loop.

2.4 Coupled isothermal batch preferential crystallization

Conventional PC is an essentially unstable process with respect to purity, since the equilibrium is racemic and the supersaturation of the unseeded enantiomer remains at a high level during the separation. A simple consideration will reveal a process strategy, which reduces the supersaturation of the counter enantiomer and eventually leads to higher product yields. Consider two separate crystallizers that contain identical racemic solutions. Upon supercooling to the same temperatures, each is seeded with one enantiomer. In that manner, E1 crystallizes in tank 1, while E2 crystallizes in tank 2. Of course, these are merely two classical PC processes working in parallel. However, both enantiomers now crystallize in a separate subsystem, each reducing its supersaturation.

In the next step, both crystallizers are connected via the liquid phase, by a continuous exchange of crystal free solution between both tanks as described in Elsner, et al. (2009). If the exchange is fast enough, both vessels share nearly the same ideally mixed liquid phase. As a result, the supersaturation of the respective counter enantiomer in each tank is continuously reduced as it crystallizes in the other tank. Figure 2.8 shows a schematic representation of this process, which we denote as coupled preferential crystallization (CPC).

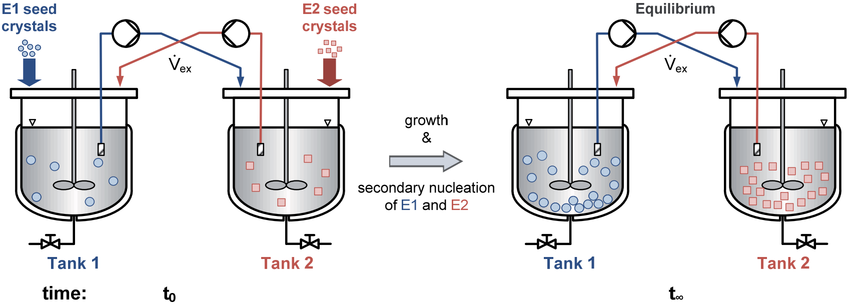

Figure 2.8: Principle of coupled preferential crystallization. Both crystallizers are connected via the liquid phase by a continuous exchange of crystal free solution. E1 and E2 crystallize separately in each crystallizer. Under ideal conditions, no nucleation of the respective counter enantiomer occurs.

Under well-chosen conditions, the liquid phase remains racemic throughout the process and nucleation of the respective counter enantiomer can be avoided. It is therefore possible to reach the new equilibrium at t_∞ and obtain two homochiral products. As depicted in Figure 2.9a, the concentrations of each enantiomer follow a common trajectory (solid line). As a consequence, the supersaturation of the seeded enantiomer in each tank is increased, while the driving force for crystallization of the counter enantiomer is reduced compared to classical PC (dashed lines). This is true, when the seeded enantiomers crystallize at the same rate and primary nucleation is absent. In this sense, CPC essentially mimics a racemization in the liquid phase. The resulting trajectory in the ternary phase diagram (Figure 2.9b) is now a straight line from point A to the eutectic at point E.

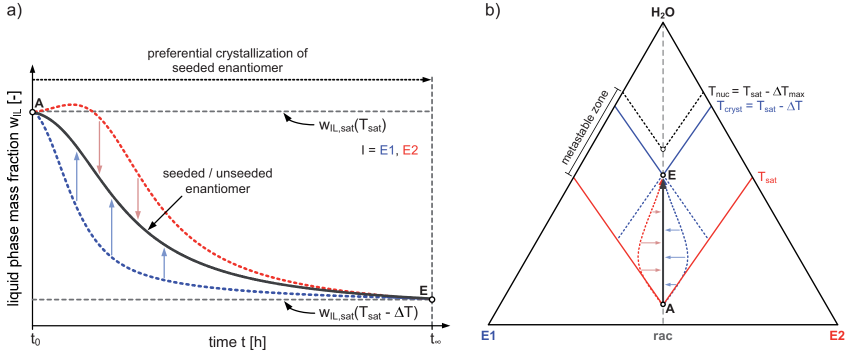

Figure 2.9: Typical time trend of the liquid mass fractions of the respective seeded enantiomer in each crystallizer (grey bold line) (a) and the corresponding trajectory in a small region of the ternary phase diagram (b).

In case the system to be crystallized belongs to the compound forming type, CPC can be applied, after a pre enrichment step has shifted the liquid phase into the three phase region (compare Figure 2.3b). It is then possible to crystallize the pure enantiomer and the racemic compound separately in each vessel. Compared to conventional PC, coupled preferential crystallization is by far less restricted in terms of polythermal operation. Since the process can be sustained for a much longer duration, with virtually no nucleation of the impurity, it is easier to implement cooling policies to further increase the yield.

2.5 Coupling preferential crystallization with selective dissolution

A variant of the coupled process to separate conglomerate forming enantiomers can be realized by operating two coupled crystallizers at different, but constant temperatures. This process will be denoted as coupled preferential crystallization with selective dissolution (CPC-D). The idea has been described in Krieger, et al. (1965) but has not received much attention in the literature since then. In this work we will investigate this new option systematically from an experimental and theoretical perspective. Partly, the results have been published in Levilain, et al. (2012) and Eicke, et al. (2013).

Its basic working principle is outlined in Figure 2.10. Tank 1 is operated at supersaturation (within the metastable zone), while the other is kept at the initial saturation temperature. The initial solutions are racemic and identical in composition. Solid racemate (E1+E2) is added to tank 2 to create a racemic suspension. The process is started by seeding tank 1 with homochiral crystals (here E1) at t_0. As preferential crystallization progresses in tank 1, E1 becomes transiently undersaturated in tank 2 due to the exchange of particle free solution. As a consequence, it selectively dissolves from the provided racemic solid phase, which is gradually purified with respect to the non-crystallizing enantiomer E2. Tank 1 is thus continuously fed with fresh racemic solution. After quantitative dissolution of E1 in tank 2 at t_1, both vessels contain homochiral solid phases.

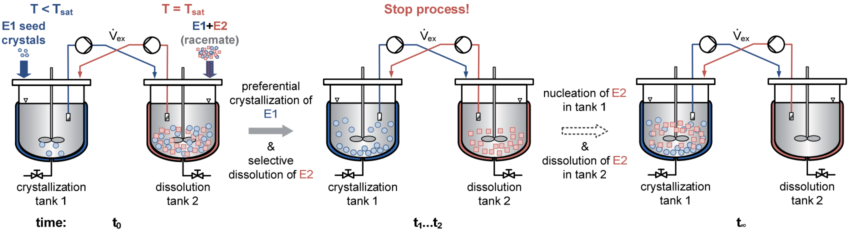

Figure 2.10: Principle of coupling preferential crystallization and selective dissolution. The solution in tank 1 is kept below saturation temperature, while tank 2 remains at the initial saturation temperature.

The advantage over CPC, introduced in the previous chapter, is the need of only one pure enantiomer. However, since only one species crystallizes during CPC-D, there is again the chance of nucleation of the other (here E2), just like during conventional PC. Nucleation of E2 in tank 1 (between t_1 and t_2) leads to its dissolution from the remaining solid phase in tank 2. Once equilibrium is reached at t_∞, all solid will have been transported from tank 2 to the crystallization vessel, leaving the latter with an almost racemic solid phase. Obviously the process has to be stopped before this event. Up to this point, though, it is possible to crystallize far more E1 than during conventional preferential crystallization.

2.6 Preferential crystallization with fines dissolution

So far we have introduced possibilities to improve preferential crystallization in terms of productivity, yield and robustness. No attention was paid to the quality of the final crystals, which is an important issue concerning further processing and handling of the solid material. In this section a simple means of influencing crystal size by fines destruction is introduced, which can in principle be applied to all three process strategies discussed above.

Seeded crystallization often leads to a wide distribution, which is not unimodal, since primary and secondary nucleation can occur next to growth of the seed fraction. In many cases the crystalline product should not only have a high purity (crucial for preferential crystallization) but also exhibit a certain crystal size distribution. The appearance of nuclei can for example be suppressed by operating at very low levels of supersaturation. However, a reduction in yield and productivity has to be accepted. Alternatively, small particles can be continuously removed, dissolved and recycled to the crystallizer via an external fines destruction loop.

This technique provides a twofold benefit for preferential crystallization. Keeping in mind that the unseeded enantiomer first occurs due to nucleation and thus in the form of minute particles, one can easily conclude that their removal and dissolution can lead to longer operating times of conventional PC. At the same time, the resulting product size distribution is able to attain larger sizes and possibly be void of smaller fractions.

Coupled preferential crystallization is in itself already a safer process concerning contamination by nucleation. The primary benefit of fines dissolution is thus shaping of the crystal size distribution.

In this work we will investigate the experimental feasibility of fines dissolution by applying it to conventional and coupled preferential crystallization. It can be readily assumed that also CPC-D will benefit from fines removal; however this was not further examined.

Apart from the described process options other means to operate preferential crystallization are available and studied. A non-exhaustive overview is given in the following chapter.

2.7 Status of preferential crystallization

Preferential crystallization is not a novel separation technique. In fact it has been discovered by one of Pasteur's students in 1866. Since then it has been studied intensively and brought to industrial application. Generally, chiral resolution requires means to break the symmetry between the two enantiomers. The processes investigated in this work do so by exploiting metastability and the selective crystallization of homochiral seeds. Naturally, there are other possibilities. A detailed account on chiral resolution by crystallization, complemented with historical experiments that already hinted at improved process strategies is compiled in the book of Jacques, et al. (1981). For a more recent account on scientific advances in this field the reader is referred to the book published by Sakai, et al. (2007) and the review of Lorenz and Seidel-Morgenstern (2014).

Apart from classical resolution via the formation of diastereomers it is possible to enforce a discrimination of two enantiomers by providing a *chiral* environment. Such an approach was investigated, for example by Tulashie, et al. (2008) who studied the feasibility of chiral solvents. Although differences in thermodynamics could not be measured it was shown that kinetics may be affected (Tulashie, et al. (2009)) facilitating resolution. These two examples directly aim at influencing the physico-chemical properties of enantiomers.

A different approach exploits *in situ* racemization by, e.g. enzymatic (Wurges, et al. (2009)) or mechanically supported means reviewed in Levilain, et al. (2009). These can be very powerful techniques and have the potential to overcome the yield limitation of 50% since the counter enantiomer is constantly transformed to its mirror image as a result of the racemization. The first option, however, requires the identification and subsequent production of a suitable enzyme able to catalyze racemization under the specific operating conditions of the crystallization process. The second option is limited to chiral compounds that can racemize under certain conditions.

The methods described so far all require the use of additional means, (bio)chemical or mechanical. Preferential crystallization can, however, be improved simply by exploiting different operating modes of the standard equipment as reported in, e.g. Polenske, et al. (2006). An interesting option is the generation of seeds from solution by polythermal operation (Ndzie, et al. (1997)), which was shown to be beneficial for reproducibility. It was further studied theoretically in Czapla, et al. (2009b) and applied to a cyclic operation of preferential crystallization (Czapla, et al. (2010)). The coupling of crystallizers studied systematically in Elsner, et al. (2007) and Elsner, et al. (2011) holds the greatest potential for improvement of preferential crystallization. It is therefore the key strategy investigated further in this work.

3 Theoretical part

3.1 Modeling and simulation

3.1.1 Model overview

Every thermal process can be described in terms of its equilibrium state, once an appropriate thermodynamic state equation is available. In the case of crystallization from solution, this state is determined by the solid-liquid equilibrium (SLE), which presents the crucial core of every attempt to model crystallization processes. Together with mass balances around the system boundaries, it is possible to estimate yield, productivity as well as purity and thus gain important preliminary information about the outcome of a process. In order to accurately describe preferential crystallization (PC), it is however necessary to consider more than just the equilibrium state, since this process operates successfully only due to kinetics. Furthermore, in order to design, control and optimize PC, the dynamic path leading to the SLE contains the key information, and this is governed by kinetics.

A general scheme of the modeling task is given in Figure 3.1. The depicted coupled process consists of two subsystems T1 and T2 that are connected via the continuous phase L, while the disperse phases S crystallize separately in each tank. The system boundaries are defined by the inner reaction volume of each vessel. Taking a closer look at a volume element inside a subsystem (here subsystem T2), one can identify the fluxes entering and leaving the solid and liquid phase.

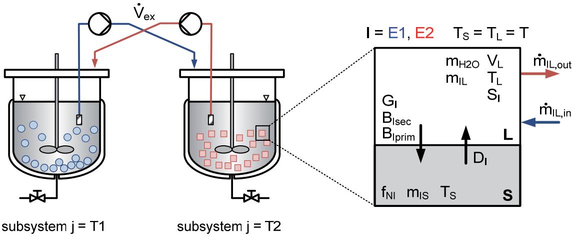

Figure 3.1: System of two coupled subsystems and a representative volume element.

Across the subsystem boundary, solvent H_2O and solute I are exchanged with the second vessel ($\dot{m}_{IL,in}$ and $\dot{m}_{IL,out}$,), while solute alone only crosses the interface between the solid and liquid phase due to growth (G_I), nucleation (B_{Isec}, B_{Iprim}) and dissolution (D_I). The current state of the liquid phase is defined by:

• mass of solute I (I = E1, E2)	m_{IL}	[kg]
• mass of solvent H_2O	m_{H2O}	[kg]
• inlet mass flow	$\dot{m}_{IL,in}$	[kg s^{-1}]
• outlet mass flow	$\dot{m}_{IL,out}$	[kg s^{-1}]
• solution volume	V_L	[m^3]
• solution temperature	T_L	[K]

and above all the solid liquid equilibrium, which determines the magnitude of the driving force. When the in- and outlet flows between both crystallizers are zero (i.e., $\dot{V}_{ex} = 0$), the model falls back to the description of two independent batch processes without any exchange.

The mass transfer between liquid and solid phase is a result of the driving force, which is characterized by the degree of supersaturation S_I. This driving force subsequently translates into the rate of crystallization that results from

• crystal growth,	G_I	[m s^{-1}]
• secondary nucleation,	B_{Isec}	[s^{-1}]
• and primary nucleation,	B_{Iprim}	[s^{-1}]

kinetics. In case of undersaturation, the driving force results in a dissolution rate D_I with unit [m s^{-1}]. Since the mass of solute I in the liquid phase is a scalar quantity and assuming ideal mixing, a time dependent mass balance is sufficient for its calculation. The solid phase in contrast is not only characterized in terms of mass. Since it usually does not consist of uniformly sized crystals it is useful to consider populations of particles along an internal property coordinate. If one were to count the number of particles within discrete intervals along, e.g. a characteristic length coordinate z_1, a histogram as depicted in Figure 3.2 can be constructed.

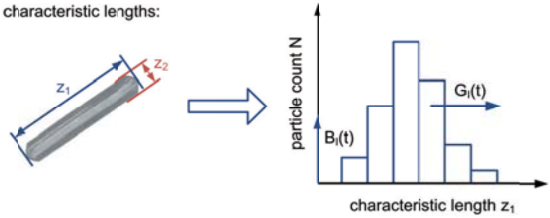

Figure 3.2: Definition of characteristic lengths for the quantification of particle properties.

The temporal evolution of the histogram along the characteristic length z_1, can be captured by considering the crystal growth rate G_I, which is essentially the speed at which the population travels along the internal coordinate, and the creation of new particles through nucleation (B_I) at the left boundary of the internal property grid. In order to simulate the dynamics of a population, the histogram is usually approximated by a continuous density function f_{NI} whose dynamics along a characteristic length can be calculated by a population balance equation (PBE). In this work a one-dimensional PBE is used for each enantiomer considering the characteristic length z_1 as defined in Figure 3.2. In order to calculate volume and mass of a crystal its shape was approximated by a cuboid assuming a constant ratio z_1/z_2, which leads to the expression,

$$V_{cryst} = z_1^{\,3} \left(\frac{z_1}{z_2} \right)^{-2} = z_1^{\,3} k_V \,, \tag{3.1}$$

containing a constant volumetric shape factor k_V. In the following we define $z = z_1$ and omit the index. To complement this brief overview, a description of all involved model equations is provided subsequently. The following sections cover the solid and liquid phase balances, kinetics formulations and auxiliary equations required to simulate the process concepts. For better readability, superscripts (k,j) contained in the equations are omitted in the continuous text.

3.1.2 The disperse phase

The concept of population balances was described in detail by Ramkrishna (2000) as well as by Randolph, et al. (1988). For a batch process, the following PBE describes the evolution of the number density function f_{NI} for enantiomer I ($I = E1, E2$), which can be the preferred ($k = p$) or the counter enantiomer ($k = c$), in subsystem j ($j = T1, T2$).

$$\frac{\partial f_{NI}^{(k,j)}}{\partial t} = -\frac{\partial}{\partial z}\left(G_I^{(k,j)} f_{NI}^{(k,j)}\right) \tag{3.2}$$

The hyperbolic partial differential eq. (3.2) consists of an accumulation term on the left hand side (lhs) and an advection term on the right hand side (rhs). Since we consider a batch process, no crystals are added (except during seeding) or removed. The corresponding input and output terms therefore do not appear on the rhs of eq. (3.2).

The velocity at which f_{NI} propagates along the internal property coordinate z ($z = z_I$) is given by the crystal growth rate G_I (eq. (3.18)), which is specific for each enantiomer in the respective subsystem j. G_I itself can be a function of z (size dependent growth rate) to account for possible growth anomalies. When dissolution is considered, G_I is replaced by the respective dissolution rate D_I (eq. (3.24)).

In order to solve eq. (3.2) boundary and initial conditions are required. The boundary condition for crystallization,

$$f_{NI}^{(k,j)}(z=0,t) = \frac{B_I^{(k,j)}}{G_I^{(k,j)}(z_0)} \tag{3.3}$$

reflects the assumption that nuclei are of negligible size and thus appear at $z = z_0 = 0$ due to nucleation at the rate B_I. It vanishes in case of dissolution assuming that particles disappear at zero size.

A major simplification implied by eq. (3.2) is the absence of any source or sink terms. New particles can only enter or leave particle state space via the left boundary but cannot appear at any other point. Phenomena such as breakage or aggregation are thus neglected as they are difficult to be quantified experimentally. Beyond that, the needle like crystals might primarily follow the streamlines created by stirring. As a consequence crystal-stirrer and crystal-crystal collisions leading to breakage are thought to occur only seldom, a conclusion also made by Mullin (2001).

Since preferential crystallization is initiated by seeding of the preferred (p) enantiomer, the initial condition,

$$f_{NI}^{(p,j)}(z,t=0) = f_{NI,seeds}^{(j)}, \tag{3.4}$$

is equal to the number density function $f_{NI,seeds}$ which describes the seed population. Equation (3.4) becomes zero when no seeds are present. The crystal size distribution (CSD) of the seeds is approximated by a log-normal distribution,

$$f_{NI,seeds}^{(j)} = \frac{A_{I,norm}^{(j)}}{\sqrt{2\pi} \cdot z \cdot \sigma_I} \cdot \exp\left[-\frac{1}{2} \left(\frac{\ln z - \ln \bar{z}_{I,seeds}}{\sigma_I} \right)^2 \right], \tag{3.5}$$

with parameters σ_I and $\bar{z}_{I,seeds}$. These are specific for each batch of seed material and are obtained by parameter fitting. The parameter $A_{I,norm}$,

$$A_{I,norm}^{(j)} = \frac{m_{Iseeds}^{(j)}}{k_V \rho_S \int_0^\infty f_{NI,cs}^{(p,j)}} = \frac{m_{Iseeds}^{(j)}}{m_{Ics}^{(p,j)}}, \tag{3.6}$$

is a scaling factor needed to calculate the seed CSD for a given mass of seeds, m_{Iseeds}, based on the distribution function, $f_{NI,cs}$, of the respective control sample (*cs*), which is determined based on a few hundred representative crystals.

3.1.3 The continuous phase

The solid phase is supplied with new material from the supersaturated solution. In case of dissolution the material stream is reversed at the expense of the crystalline phase. The accumulation of the mass of solute *I* in the liquid phase, m_{IL}, is calculated by the following mass balance:

$$\frac{dm_{IL}^{(k,j)}(t)}{dt} = \dot{m}_{IL,in}^{(k,j)}(t) - \dot{m}_{IL,out}^{(k,j)}(t) - 3k_V \rho_S \cdot \int_0^\infty z^2 G_I^{(k,j)} f_{NI}^{(k,j)}(z,t) dz. \tag{3.7}$$

The rhs of eq. (3.7) contains, to begin with, the input and output mass flow rates $\dot{m}_{IL,in}$ and $\dot{m}_{IL,out}$, respectively, which appear only when solution is exchanged with the second crystallizer.

$$\dot{m}_{IL,in}^{(k,j)}(t) = \dot{V}_{ex} \cdot \rho_L^{(j^*)} \cdot w_{IL}^{(k,j^*)} = \dot{V}_{ex} \cdot C_{IL}^{(k,j^*)}, j^* = T1, T2; j^* \neq j. \tag{3.8}$$

Solute *I* enters tank *j* with a volumetric exchange flow rate $\dot{V}_{ex}$. The current solution density ρ_L and the liquid mass fraction w_{IL} in the other crystallizer j^*, determine the mass concentration, C_{IL}, of dissolved enantiomer *I* at the system boundary of tank *j*. In the same manner enantiomer *I* leaves tank *j*, supplying the second subsystem with particle free solution.

$$\dot{m}_{IL,out}^{(k,j)}(t) = \dot{V}_{ex} \cdot \rho_L^{(j)} \cdot w_{IL}^{(k,j)} = \dot{V}_{ex} \cdot C_{IL}^{(k,j)} \tag{3.9}$$

The current solution density, ρ_L, is calculated via the empirical relationship,

$$\rho_L^{(j)} = \rho_{H2O}^{(j)} + K_3 \cdot \sum_I w_{IL}^{(j)}, I = E1, E2, \tag{3.10}$$

which depends on the total concentration of all dissolved solute species and the density of water, whose temperature dependence is determined by

$$\rho_{H2O}^{(j)}(T_L^{(j)}) = \frac{1}{K_1 + K_2 \cdot \left(T_L^{(j)}\right)^2}. \tag{3.11}$$

The parameters K_i in eqs. (3.10) and (3.11), were obtained experimentally by Elsner et al. (2011).

The connection between the PBE (eq. (3.2)) and the mass balance (eq. (3.7)) is accomplished by introducing the integral term on the rhs of eq. (3.7) which is essentially the temporal change in solid mass. It includes a volumetric shape factor k_V, the density of a crystal ρ_S and the integration over the entire internal coordinate z. Considering growth rate G_I to be independent of size, the integral is identical to the second moment of the population f_{NI} (compare eq. (3.25)).

The above integro-differential equation can be solved with the initial condition,

$$m_{IL}^{(k,j)}(t=0)=m_{IL,0}^{(k,j)}\,, \tag{3.12}$$

which is simply the initially dissolved mass $m_{IL,0}$ of each component I.

When considering polythermal operation, the following simplified energy balance was used to capture the dynamics of the absolute solution temperature:

$$\frac{dT_L^{(j)}}{dt}=\frac{k_W A_W}{c_{pL}m_{tot}^{(j)}}\left(T_{DJ}^{(j)}-T_L^{(j)}\right)-\frac{\Delta h_{cryst}}{c_{pL}m_{tot}^{(j)}}\frac{dm_S^{(j)}}{dt}\,. \tag{3.13}$$

It includes the heat transfer between the double jacket (DJ) and the interior of the crystallizer, which is characterized by the heat transfer coefficient, k_W and the heat exchange surface A_W, as well as the heat of crystallization. The latter is linked to the change of total solid mass, m_S, via the specific enthalpy Δh_{cryst}. The heat capacity of the solution, c_{pL}, is assumed to be constant and equal to that of water. The mass of the suspension, m_{tot}, is the sum of all component masses in liquid and solid phase. Additional input and output terms that would appear due to the exchange of solution when considering two coupled crystallizers are neglected, since the temperatures of the streams entering and leaving each vessel have approximately the same temperature as the solutions inside. Furthermore, temperature was measured and controlled in all experiments. Therefore, eq. (3.13) was frequently replaced by,

$$T_L^{(j)}=T_{Lw}^{(j)}\,, \tag{3.14}$$

were T_{Lw} denotes the temperature setpoint.

Before turning to the involved kinetics, it is necessary to define the driving force for crystallization. As mentioned earlier it can be quantified in terms of supersaturation

$$S_I^{(k,j)}(T)=\frac{w_{IL}^{(k,j)}(t)}{w_{IL,eq}^{(k,j)}(T)}\,, \tag{3.15}$$

which is the ratio of the current mass fraction w_{IL} and the equilibrium mass fraction $w_{IL,eq}$ in the liquid phase. The first is defined by,

$$w_{IL}^{(k,j)}(t)=\frac{m_{IL}^{(k,j)}}{m_{H2O}^{(j)}+\sum_I m_{IL}^{(k,j)}}\,, \tag{3.16}$$

while the latter is captured by the empirical solubility equation,

$$w_{IL,eq}^{(k,j)}(T)=-a_2\cdot\left(w_{I^*L}^{(k,j)}\right)^2-a_1\cdot w_{I^*L}^{(k,j)}+m_{sol}\cdot T_L^{(j)}+b_{sol}\,,\quad I^*=E1,E2;I^*\neq I\,, \tag{3.17}$$

which contains a linear dependence on temperature T_L (with unit °C) and additionally considers an interaction between the two enantiomers. In that sense, at constant temperature, the presence of one enantiomer (I^*) in the liquid phase slightly reduces the solubility of the other (I). It should be kept in mind that eq. (3.17) is specific to the model compound threonine in water (cf. section 5.1) and the temperature range considered. From eq. (3.15) one can deduce that crystallization occurs when $S_I > 1$ and dissolution when $S_I < 1$. At equilibrium the supersaturation thus has to be equal to one.

3.1.4 Kinetics formulation

The process of phase separation during crystallization involves complex phenomena which can be approximated by semi empirical equations. As we are interested in the macroscopic process, there is no need to model on a physically detailed level in the first place. Instead, lumped parameters occur in the kinetics equations that capture overall effects which are accessible rather easily by experiments.

During seeded crystallization, crystal growth is the predominant kinetics. It is quantified by an overall crystal growth rate G_I, in this case resulting in an increase of the characteristic length defined earlier. The compact power law,

$$G_I^{(k,j)}(t) = k_g^{(j)}(\omega, T) \cdot \left(S_I^{(k,j)}(t) - 1\right)^g, \tag{3.18}$$

contains an overall crystal growth coefficient, k_g, and an exponent g to account for a non-linear dependence of the growth rate on the overall driving force determined by the supersaturation of the bulk phase.

The crystal growth coefficient k_g further depends on temperature and the degree of agitation.

$$k_g^{(j)}(\omega, T) = k_{g0} \cdot {\omega_{St}}^{n_g} \cdot \exp\left(-\frac{E_{Ag}}{R \cdot T_L^{(j)}(t)}\right) \tag{3.19}$$

Equation (3.19) contains an Arrhenius formulation with the activation energy E_{Ag} for crystal growth and a dependence on the rotational stirrer speed ω_{St}. The exponent n_g is usually greater than zero since it can be assumed that the diffusional resistances are inversely proportional to the degree of agitation. This can be interpreted by a reduction of the diffusional layer thickness when the velocity difference between the solution and a crystal is increased.

The creation of new particles is caused by nucleation. At moderate levels of supersaturation, secondary rather than primary nucleation is predominant. Its dependence on supersaturation is again captured by a power law given by,

$$B_{I\sec}^{(k,j)}(t) = k_{b\sec}^{(j)}(\omega, T) \cdot \left(S_I^{(k,j)}(t) - 1\right)^{b_{\sec}} \cdot \left(\mu_{3I}^{(k,j)}(t)\right)^{n_{\mu 3}}. \tag{3.20}$$

Furthermore, it can be assumed that secondary nucleation increases with larger amounts of the respective crystals. This is considered by the last term containing the third moment. Therefore, secondary nucleation can only occur, if a solid phase exists and is initially zero in case of the unseeded enantiomer. The secondary nucleation coefficient, k_{bsec}, is assumed to depend on temperature and the degree of agitation.

$$k_{b\sec}^{(j)}(\omega,T) = k_{b\sec 0}\cdot\exp\left(-\frac{n_{b\sec}}{\omega_{St}}\right)\cdot\exp\left(-\frac{E_{Ab\sec}}{R\cdot T_L^{(j)}(t)}\right) \tag{3.21}$$

Analogous to eq. (3.19), temperature affects secondary nucleation by an Arrhenius equation with activation energy E_{Absec}. The influence of the stirring rate on growth and secondary nucleation in eqs.(3.19) and (3.20) were determined experimentally and reported by Angelov, et al. (2008b).

At higher levels of supersaturation, primary nucleation leads to the creation of particles directly from the solution. In particular, the unseeded enantiomer eventually appears in the solid phase due to this mechanism. The following equation is based on classical nucleation theory and represents an adaptation of the original model described in Mersmann (2001). The derivation can be found in Elsner, et al. (2011).

$$\begin{aligned} B_{Iprim0}^{(k,j)}(t) = {} & k_{bprim1}\cdot T_L^{(j)}(t)\cdot\exp\left(-\frac{K_{Tvisc}}{T_L^{(j)}(t)}\right)\cdot\exp\left(-\frac{\sum_I w_{IL}^{(j)}(t)}{K_{wvisc}}\right)\cdot\sqrt{\ln\left(\frac{\rho_S}{C_{IL,eq}^{(k,j)}(T)}\right)}\cdot \\ & \left(S_I^{(k,j)}(t)\cdot C_{IL,eq}^{(k,j)}(T)\right)^{7/3}\cdot\exp\left(-k_{bprim2}\cdot\left(\ln\left(\frac{\rho_S}{C_{IL,eq}^{(k,j)}(T)}\right)\right)^3\cdot\frac{1}{\left(\ln S_I^{(k,j)}(t)\right)^2}\right) \end{aligned} \tag{3.22}$$

During parameter estimation studies it was found that eq. (3.22) alone was not able to sufficiently reproduce the nucleation events observed experimentally. Therefore, the overall primary nucleation rate,

$$B_{Iprim}^{(k,j)}(t) = B_{Iprim0}^{(k,j)}(t)\cdot\left(1 + A_{prim}\left(\mu_{2I^*}^{(k,j)}(t)\right)^{n_{\mu 2}}\right), \tag{3.23}$$

contains an additional term based on the assumption that in preferential crystallization, the seeded enantiomer represents the largest heterogeneous surface, which can catalyze primary nucleation of the unseeded species. To account for this influence, the additional term contains the second moment μ_{2I*}, which is a measure for the total crystal surface area. The parameter A_{prim} is a gain factor that determines the magnitude of influence. The second parameter $n_{\mu 2}$ accounts for non-linearities. The sum of eqs. (3.20) and (3.23) is the total rate of nucleation B_I contained in the boundary condition of the PBE (eq. (3.3)).

Apart from crystallization, dissolution has to be considered for the process option involving preferential crystallization coupled with selective dissolution (cf. section 2.4). The rate of dissolution D_I is given by a simple power law,

$$D_I^{(k,j)}(t) = k_d\cdot\left(S_I^{(k,j)} - 1\right)^d \tag{3.24}$$

and was assumed to depend linearly on supersaturation ($d = 1$). The rate constant k_d was adjusted using concentration data recorded during the preparation of experiments, where both enantiomers were dissolved to create the initial solutions. Since dissolution is generally faster than crystallization, it was considered to have no rate limiting effects on the overall process. Therefore, in this work, a very simple kinetic approach was chosen.

3.1.5 Moment transformation of the population balance equation

The PBE (eq. (3.2)) can be transformed to provide condensed information represented by the moments of the number density function f_{NI}. Especially when knowledge about the entire particle distribution is not needed and size independent growth is assumed, it is sufficient to use a moment model to describe the solid phase evolution. This model reduction technique known as the method of moments (MOM) drastically reduces computing time but a loss of information has to be taken into account.

The ith moment of the distribution of component *I* is defined as

$$\mu_{iI}^{(k,j)} = \int_{z=0}^{\infty} z^i \cdot f_{NI}^{(k,j)} dz \,. \tag{3.25}$$

Each of the first four moments can be assigned a physical meaning as follows:

-	μ_{0I}	total number of crystals	[-]
-	μ_{1I}	cumulative length of all crystals	[m]
-	μ_{2I}	proportional to total surface area of crystals	[m^2]
-	μ_{3I}	proportional to combined crystal volume	[m^3]

Higher moments are more difficult to be interpreted physically but can be used to reconstruct the complete crystal size distribution as described in Qamar, et al. (2008).

Based on the definition given by eq. (3.25) and the PBE (eq. (3.2)) one can derive a set of ODEs. The population balance is therefore multiplied by the ith power of the property coordinate *z* and integrated over the semi-infinite interval [0,∞) to yield

$$\int_0^{\infty} z^i \cdot \frac{\partial (f_{NI}^{(k,j)})}{\partial t} dz = -\int_0^{\infty} z^i \cdot \frac{\partial (G_I^{(k,j)} f_{NI}^{(k,j)})}{\partial z} dz \,. \tag{3.26}$$

According to *Leibnitz' rule* for differentiating integrals, the order of integration and differentiation on the lhs of eq. (3.26) can be reversed since the integration limits are constant. The resulting expression contains the definition of the ith moment (eq. (3.25)) and thus gives

$$\frac{d}{dt} \int_0^{\infty} z^i \cdot f_{NI}^{(k,j)} dz = \frac{d\mu_{iI}^{(k,j)}}{dt} \,. \tag{3.27}$$

The integral on the rhs of eq. (3.26) is evaluated assuming that the growth rate G_I does not depend on the internal coordinate *z*. In this case integration by parts yields

$$G_I^{(k,j)} \int_0^{\infty} z^i \cdot \frac{\partial f_{NI}^{(k,j)}}{\partial z} dz = G_I^{(k,j)} \left(\left[z^i f_{NI}^{(k,j)} \right]_0^{\infty} - \int_0^{\infty} i \cdot z^{i-1} f_{NI}^{(k,j)} dz \right). \tag{3.28}$$

Considering the regularity condition, which states that $f_{NI}(z \rightarrow \infty) = 0$, the combination of eqs. (3.26), (3.27) and (3.28) leads to a set of ODEs,

$$\frac{d\mu_{iI}^{(k,j)}}{dt} = 0^i \cdot G_I^{(k,j)} f_{NI}^{(k,j)}(z_0) + i \cdot G_I^{(k,j)} \cdot \mu_{i-1I}^{(k,j)}. \tag{3.29}$$

for the first i moments. The 0th moment, μ_{0I}, is obtained by defining that $0^0 = 1$ and by introducing the boundary condition given in eq. (3.3), which leads to the following equation:

$$\frac{d\mu_{0I}^{(k,j)}}{dt} = B_I^{(k,j)}. \tag{3.30}$$

The remaining three moments are calculated as,

$$\frac{d\mu_{iI}^{(k,j)}}{dt} = i \cdot G_I^{(k,j)} \mu_{i-1I}^{(k,j)}, i = 1,2,3. \tag{3.31}$$

Since the moment model is computationally far less expensive than the full PBE model, it was used in this work for parameter estimation and process optimization.

3.1.6 Numerical aspects

The PBE model introduced in sections 3.1.2-3.1.4 contains highly non-linear terms. An analytical solution is therefore not available; thus it has to be solved numerically. In this thesis the numerical computing environment MATLAB was used, which provides Runge-Kutta based solvers for ordinary differential equations. In particular the solvers ode45 and ode15s were used to obtain solutions in the time domain. The latter was applied in case of stiff problems, i.e. when dissolution was considered, or in case ode45 did not produce reasonable results (e.g. oscillating solutions, negative masses). The internal property coordinate, z, was discretized using the finite volume method (FVM). This technique, were all dimensions but one are discretized is called the method of lines. In the following, the discretization of the PBE (eq. (3.2)) is briefly explained. A more detailed treatment of FVM is given in Versteeg, et al. (1995). Figure 3.3 shows the discretization around an inner CV.

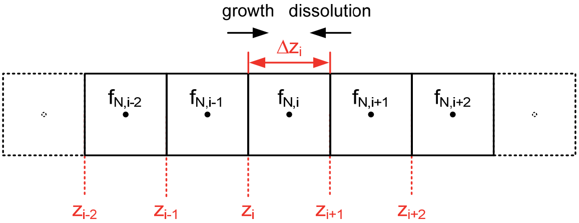

Figure 3.3: Central control volume element.

The first step is to divide the internal coordinate, z, into n discrete control volumes (CV). The simplest means is to generate an equidistant grid. For some problems it might, however, be more suitable to use an unevenly spaced grid. For example, in regions were high gradients are expected, it can be beneficial to increase the number of discretes to obtain higher accuracy. In this work, an equidistant grid was used. Usually, the number of discretes was chosen to be n = 2000 for a maximum characteristic length $z_{n+1} = L = 0.03$ m (cf. Figure 3.4).

The distance between the boundaries of each CV, Δz_i, was thus constant. In the following, the PBE is integrated over the interval $[z_i, z_{i+1}]$:

$$\underbrace{\int_{z_i}^{z_{i+1}} \frac{\partial f_N}{\partial t} dz}_{accumulation} = \underbrace{-G \int_{z_i}^{z_{i+1}} \frac{\partial f_N}{\partial z} dz}_{convection} . \tag{3.32}$$

Assuming piecewise constant profiles, the integrals can be evaluated to yield,

$$\int_{z_i}^{z_{i+1}} \frac{\partial f_N}{\partial t} dz = \frac{df_{N,i}}{dt} \Delta z_i , \tag{3.33}$$

for the accumulation term and,

$$-G \int_{z_i}^{z_{i+1}} \frac{\partial f_N}{\partial z} dz = -G\left(f_N\big|_{z_{i+1}} - f_N\big|_{z_i} \right), \tag{3.34}$$

for the convection term. Applying the upwind scheme to eq. (3.34) allows us to indicate the fluxes crossing the CV boundaries for growth and dissolution. In case of crystallization, the internal property f_N moves from left to right in case of dissolution in the opposite direction. The values of f_N at the boundaries z_{i+1} and z_i therefore are,

$$-G\left(f_N\big|_{z_{i+1}} - f_N\big|_{z_i} \right) = \begin{cases} -G\left(f_{N,i} - f_{N,i-1} \right), crystallization \\ -D\left(f_{N,i+1} - f_{N,i} \right), dissolution \end{cases} . \tag{3.35}$$

Combining eqs. (3.33) and (3.35) leads to a set of n-1 ODEs for crystallization,

$$\frac{df_{N,i}}{dt} = -G \frac{\left(f_{N,i} - f_{N,i-1} \right)}{\Delta z_i} , \tag{3.36}$$

and dissolution,

$$\frac{df_{N,i}}{dt} = -D \frac{\left(f_{N,i+1} - f_{N,i} \right)}{\Delta z_i} . \tag{3.37}$$

The boundary elements shown in Figure 3.4 have to be treated separately considering the respective boundary conditions.

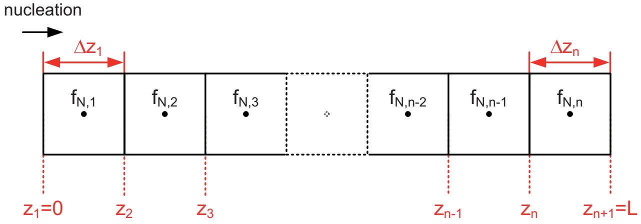

Figure 3.4: Boundary control volume elements.

During crystallization, particles enter the first CV via the boundary at z_1 due to nucleation. The resulting ODE is given as,

$$\frac{df_{N,1}}{dt} = -G\frac{\left(f_{N,1} - f_{N,0}\right)}{\Delta z_1} = -G\frac{f_{N,1}}{\Delta z_1} + \frac{B}{\Delta z_1}, \tag{3.38}$$

where $f_{N,0}$ contains the boundary condition introduced in eq. (3.3). For dissolution, the right most CV has to be considered. It is assumed, due to the regularity condition, that no particles enter via the boundary at z_{n+1} ($f_{N,n+1} = 0$). The ODE for dissolution is then given by,

$$\frac{df_{N,n}}{dt} = -D\frac{\left(f_{N,n+1} - f_{N,n}\right)}{\Delta z_n} = -D\frac{\left(-f_{N,n}\right)}{\Delta z_n}. \tag{3.39}$$

3.1.7 Balance equations for fines dissolution

In order to simulate the process options involving fines dissolution (FD, cf. section 2.6), the model has to be slightly adapted to include the additional fines withdrawal unit as shown in Figure 3.5. A constant stream of suspension is removed via a filter with a certain cut-off size, cycled through the heated tube and fed back to the respective crystallizer as a clear solution.

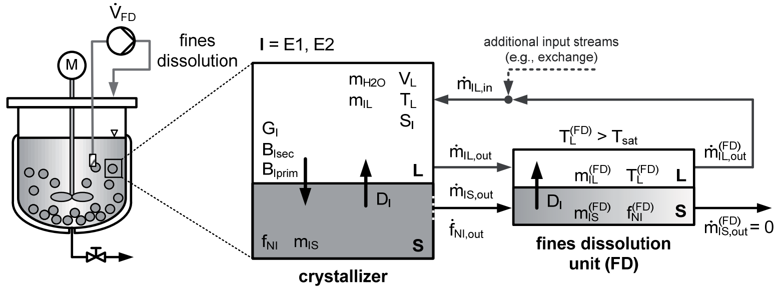
$\dot{V}_{FD}$
fines dissolution
M
I = E1, E2
m_{H2O}
V_L
m_{IL}
T_L
S_I
G_I
B_{Isec}
B_{Iprim}
L
D_I
f_{NI}
m_{IS}
S
crystallizer
additional input streams (e.g., exchange)
$\dot{m}_{IL,in}$
$\dot{m}_{IL,out}$
$\dot{m}_{IS,out}$
$\dot{f}_{NI,out}$
$T_L^{(FD)} > T_{sat}$
$\dot{m}_{IL,out}^{(FD)}$
$m_{IL}^{(FD)}$
$T_L^{(FD)}$
L
D_I
$m_{IS}^{(FD)}$
$f_{NI}^{(FD)}$
S
fines dissolution unit (FD)
$\dot{m}_{IS,out}^{(FD)} = 0$

Figure 3.5: Crystallizer with an attached fines dissolution unit and the resulting in- and output streams.

The PBE eq. (3.2) is therefore extended by a second term on the rhs to include the removal of a fraction of the entire population containing small crystals:

$$\frac{\partial f_{NI}^{(k,j)}}{\partial t} = -\frac{\partial}{\partial z}\left(G_I^{(k,j)} f_{NI}^{(k,j)}\right) - \frac{\dot{V}_{FD}}{V_L^{(j)}} R_{FD}(z) f_{NI}^{(k,j)}. \tag{3.40}$$

As a first approximation, the volumetric fines dissolution flow rate $\dot{V}_{FD}$ and the liquid phase volume V_L determine the mean residence time of crystals in the suspension that can pass through the filter. The S-shaped function R_{FD},

$$R_{FD}(z) = \exp\left(-\left(\frac{z}{d_{FD}}\right)^{n_{FD}}\right), \tag{3.41}$$

characterizes the fines dissolution filter with parameter d_{FD} as the cut-off size. Particles with a characteristic length $z < d_{FD}$ can enter the fines dissolution unit. The exponent n_{FD} determines the steepness of the curve. Assuming that all particles below the size d_{FD} have the same residence time,

$$\dot{m}_{IS,out}^{(k,j)} = \frac{\dot{V}_{FD}}{V_L^{(j)}} k_V \rho_S \int_{z=0}^{\infty} z^3 R_{FD}(z) f_{NI}^{(k,j)} dz\,, \tag{3.42}$$

is the solid mass output stream of enantiomer I from the crystallizer to the fines dissolution unit. The corresponding liquid mass flow results from,

$$\dot{m}_{IL,out}^{(k,j)} = \dot{V}_{FD} \cdot \rho_L^{(j)} \cdot w_{IL}^{(k,j)} = \dot{V}_{FD} \cdot C_{IL}^{(k,j)}\,. \tag{3.43}$$

It is further assumed that all solid entering the fines dissolution unit is immediately dissolved. Additionally, the mean residence time of the solution travelling through the unit is very small compared to the time constants of the overall process. Delay effects are therefore neglected. In consequence of these assumptions, the mass stream leaving the fines dissolution unit,

$$\dot{m}_{IL,out}^{(k,FD)} = \dot{m}_{IS,in}^{(k,FD)} + \dot{m}_{IL,in}^{(k,FD)} = \dot{m}_{IS,out}^{(k,j)} + \dot{m}_{IL,out}^{(k,j)}\,, \tag{3.44}$$

consists only of clear solution and can be calculated directly as the sum of the solid and liquid streams leaving the crystallizers. The mass balance of the continuous phase of a single, uncoupled crystallizer is then

$$\frac{dm_{IL}^{(k,j)}(t)}{dt} = \dot{m}_{IL,in}^{(k,j)}(t) - \dot{m}_{IL,out}^{(k,j)}(t) - 3k_V \rho_S \cdot \int_0^{\infty} z^2 G_I^{(k,j)} f_{NI}^{(k,j)}(z,t) dz\,, \tag{3.45}$$

with the input stream,

$$\dot{m}_{IL,in}^{(k,j)}(t) = \dot{m}_{IL,out}^{(k,FD)}\,. \tag{3.46}$$

The above model was used for a first theoretical investigation of PC with fines dissolution (Eicke, et al. (2009b)). Naturally, the assumptions made are not valid anymore when the residence time inside the fines dissolution unit becomes significantly large or when crystals are not dissolved quantitatively. In such cases, a second set of population balance equations has to be introduced, which considers the transport through the unit as well as dissolution kinetics. The unit can be approximated by a plug flow tubular reactor, leading to the transport equation,

$$\frac{\partial f_{NI}^{(FD)}}{\partial t} = -u_{FD} \underbrace{\frac{\partial f_{NI}^{(FD)}}{\partial x}}_{\substack{\text{change}\\\text{along}\\\text{external}\\\text{coordinate}}} - D \underbrace{\frac{\partial f_{NI}^{(FD)}}{\partial z}}_{\substack{\text{change}\\\text{along}\\\text{internal}\\\text{coordinate}}}\,. \tag{3.47}$$

Due to the additional differential equations, the numerical solution of the model becomes computationally very expensive. Such a high degree of detail is also not necessary for a first investigation of the process as done in this work, especially when the assumptions made are in fact justified due to the experimental setup.

3.1.8 Parameter estimation

With available experimental data, an attempt was made to improve the predictive capabilities of the model described above. This was done by adjusting the values of a set of kinetic parameters, ***p***, while minimizing an objective function (OF), *J*, using the method of least squares. The optimization problem is thus,

$$\min_{\mathbf{p}} J \ , \tag{3.48}$$

with $\boldsymbol{p} = (p_1, p_2, \dots, p_i)$.

For a single experiment performed in one crystallizer, the experimental data contains the dynamic concentration profiles of both enantiomers I, consisting of i data points. In that case, the OF has the form,

$$J = \sum_{I} \frac{1}{N_{dat}} \sum_{i=1}^{N_{dat}} \left(w_{IL,sim,i}^{(k,j)} - w_{IL,\exp,i}^{(k,j)} \right)^2 \ , \tag{3.49}$$

with N_{dat} as the number of data points for each enantiomer, which becomes important when more than one experiment is used for the parameter estimation. In this work, multiple experiments were eventually used to cover a larger range of operating conditions. In most cases, a very good model fit can be achieved when only one experiment is considered. The obtained kinetic parameter values, however, are often not sufficient for other process conditions. Therefore, a combination of 11 experiments was chosen, which consisted of conventional and coupled preferential crystallization under iso- and polythermal conditions. The OF is extended accordingly to,

$$J = \sum_{m=1}^{N_{\exp}} \frac{1}{N_{\exp}} \sum_{I} \frac{1}{N_{dat,m}} \sum_{i=1}^{N_{dat}} \left(w_{IL,sim,i}^{(k,j)} - w_{IL,\exp,i}^{(k,j)} \right)^2 \ . \tag{3.50}$$

The OF of each individual experiment, m, is now weighted by its number of data points, $N_{dat,m}$, to avoid any bias. For some of the experiments, the final purity $Pu_{exp}(t_{end})$ of the product served as additional information, which was included in the optimization problem. This was especially the case for the coupled experiments, since they contain redundant data: their concentration measurements are ambiguous in the sense that a drop in concentration of one enantiomer can either be caused by its growing seeds or because it nucleates in the other vessel. This cannot be distinguished via the liquid phase. Therefore, purity was considered in the form of a nonlinear constraint leading to the following optimization problem:

$$\begin{aligned} &\min_{\mathbf{p}} && J \\ &\textit{subject to}: && Pu_{\exp}(t_{end}) \le Pu_{sim}(t_{end}) \end{aligned} \ . \tag{3.51}$$

The OF was minimized using the global optimization toolbox in MATLAB. Since one optimization run usually did not converge to a satisfactory solution, a combination of different optimizers was used, while adapting lower and upper bounds for each individual parameter as well as the starting point. In particular, the global optimizer PATTERNSEARCH was used to cover a broad range of parameter values. The final optimal parameter set was then taken to initiate a subsequent run using the local optimizer FMINSEARCH (Nelder-Mead simplex algorithm) to further refine the parameters. The optimal point from the local optimization was then again used as the initial point for PATTERNSEARCH, which usually resulted in a further improvement of the OF. This procedure was repeated, until the optimal point resulted in a reasonable fit of the model.

3.2 Process control and optimization

Parts of this work are the result of a collaboration with the Control Systems Group of Prof. Jörg Raisch from the Technical University, Berlin. This recently finished DFG funded joint project ("Prozessführungsstrategien bei der Trennung racemischer Gemische mittels Bevorzugter Kristallisation.") consisted of the development and experimental verification of control concepts for preferential crystallization. At later stages of this thesis, theoretical studies of the Berlin group on the optimization of classical PC were adapted to be used for coupled PC and investigated experimentally at the Max Planck Institute in Magdeburg.

3.2.1 Control objectives

Two different control objectives are pursued, both using temperature as the manipulating variable to realize the respective control task. The first aims at controlling coupled preferential crystallization (CPC) so that both seeded enantiomers crystallize at the same rate. The whole idea behind CPC is the reduction of supersaturation of the respective unseeded enantiomer. This works best, when symmetrical crystallization in both tanks is maintained throughout the process. In most cases, however, the two different seed batches used for the individual crystallizers are not identical in terms of their size distribution. On top of that, one has little control over the quality with respect to the surface of the seed crystals. Some may have smooth, others roughened surfaces.

All of these factors result in different total surface areas that have a direct impact on the rate at which these seeds crystallize. Thus, when both coupled crystallizers are operated at the same isothermal temperature, one enantiomer might crystallize faster than the other. This, in turn, leads to an enrichment of the liquid phase with respect to the slowly crystallizing enantiomer. Since in that case its supersaturation remains at a higher level, the chance of nucleation is elevated and the process becomes less robust. This is particularly important when one enantiomer has a strong influence on the solubility of the other.

The second control objective aims at the productivity of CPC by controlling the supersaturation. An isothermal CPC process gradually becomes less productive as the driving force is diminished. Permanent further cooling is therefore an attractive option to maintain a certain level of supersaturation (see section 5.3.5 regarding polythermal operation). However, again care needs to be taken to stay in the metastable zone. When this information is available, a safe level can be chosen as a setpoint for constant supersaturation control.

3.2.2 Symmetry control

The working principle of the symmetry controller is shown in Figure 3.6. It is implemented using a MATLAB workstation, which receives concentration and temperature measurements from the plant. Based on these values, updated temperature setpoints are sent back to the respective thermostat, which controls the crystallization temperature. The control strategy uses a master-slave configuration where the master tank provides the reference trajectory, which the slave vessel follows. The symbols for each tank (j = T1, T2) in Figure 3.6 have the following meanings:

$\alpha_L^{(j)}$	optical rotation angle (physical quantity)	[°]
$\rho_L^{(j)}$	solution density (physical quantity)	[g/cm^3]
$\tilde{\alpha}_L^{(j)}$	measured optical rotation angle	[°]
$\tilde{\rho}_L^{(j)}$	measured solution density	[g/cm^3]
$\tilde{w}_{E1L}^{(j)}, \tilde{w}_{E2L}^{(j)}$	measured liquid mass fraction from calibration curve	[g/g]
$\hat{w}_{E1L}^{(j)}, \hat{w}_{E2L}^{(j)}$	liquid mass fraction obtained from the estimator/filter	[g/g]
$\hat{e}^{(p)}$	estimated control deviation	[g/g]
$T^{(j)}$	crystallizer temperature	[K]
$T_w^{(j)}$	setpoint for crystallizer temperature	[K]
ΔT	controller output	[K]

In the setup shown in the figure, tank 2 is the master. This means that the liquid mass fraction of the seeded enantiomer (here E2) of this vessel serves as a setpoint trajectory for the mass fraction of the seeded enantiomer (E1) in the slave vessel (T1). Tank 2 is operated at an isothermal temperature with setpoint $T_w^{(T2)}$. The temperature in the slave vessel is continuously adjusted by the symmetry controller to minimize the control deviation,

$$\hat{e}^{(p)} = \hat{w}_{E2L}^{(p,T2)} - \hat{w}_{E1L}^{(p,T1)}, \tag{3.52}$$

between the concentration trajectories of the seeded enantiomers.

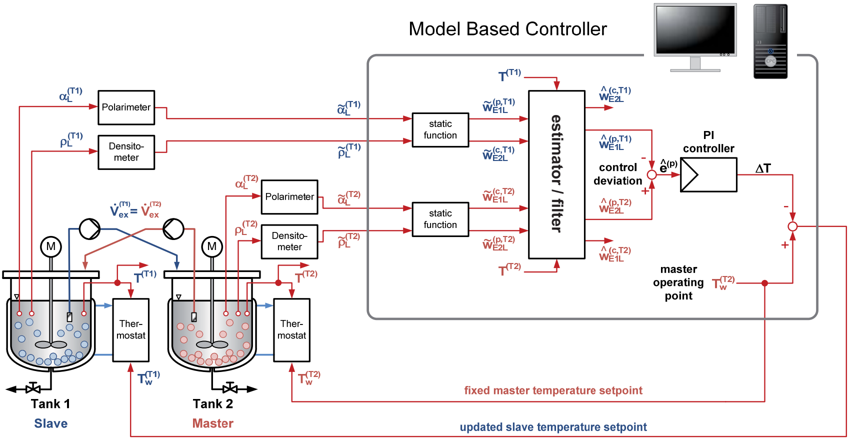
Model Based Controller
$\alpha_L^{(T1)}$
Polarimeter
$\rho_L^{(T1)}$
Densito-meter
$\dot{V}_{ex}^{(T1)} = \dot{V}_{ex}^{(T2)}$
$\alpha_L^{(T2)}$
Polarimeter
$\rho_L^{(T2)}$
Densito-meter
M
M
$T^{(T1)}$
Ther-mostat
$T^{(T2)}$
Ther-mostat
$T_w^{(T1)}$
$T_w^{(T2)}$
Tank 1
Slave
Tank 2
Master
$\tilde{\alpha}_L^{(T1)}$
$\tilde{\rho}_L^{(T1)}$
$\tilde{\alpha}_L^{(T2)}$
$\tilde{\rho}_L^{(T2)}$
static function
static function
$T^{(T1)}$
$\tilde{w}_{E1L}^{(p,T1)}$
$\tilde{w}_{E2L}^{(c,T1)}$
$\tilde{w}_{E1L}^{(c,T2)}$
$\tilde{w}_{E2L}^{(p,T2)}$
$T^{(T2)}$
estimator / filter
$\hat{w}_{E2L}^{(c,T1)}$
$\hat{w}_{E1L}^{(p,T1)}$
$\hat{w}_{E2L}^{(p,T2)}$
$\hat{w}_{E1L}^{(c,T2)}$
control deviation
$\hat{e}^{(p)}$
PI controller
ΔT
master operating point
$T_w^{(T2)}$
fixed master temperature setpoint
updated slave temperature setpoint

Figure 3.6: Controller structure for symmetry control of coupled preferential crystallization.

The control task could in principle be realized without the use of the additional estimator/filter. In that case the control deviation,

$$\tilde{e}^{(p)} = \tilde{w}_{E2L}^{(p,T2)} - \tilde{w}_{E1L}^{(p,T1)}, \tag{3.53}$$

would be directly calculated from the measured liquid mass fractions. However, this might lead to an unstable or oscillating control, since the measurement contains noise and outliers. These sudden signal changes cannot be handled well by the PI-controller and a smooth signal is therefore necessary. How this is generated is briefly described in the following. A more detailed account is given in Hofmann, et al. (2010) as well as in the dissertation written by Hofmann.

Both, the optical rotation angle α_L and the solution density ρ_L are processed by a static function, which is essentially the calibration curve of the polarimeter and the densitometer (see section 5.3). The resulting current liquid mass fractions $\tilde{w}_{IL}^{(j)}$, along with the temperatures $T^{(j)}$, serve as the input for the estimator/filter, which calculates the estimated liquid mass fractions $\hat{w}_{IL}^{(j)}$ based on a mathematical model of the process. Every time, a new measurement is available (typically every minute), the estimator/filter also decides whether to keep or discard the values. In most cases, outliers are caused by air bubbles in the analytical paths. At times, it can happen that no valid measurement is available for a prolonged period of time. In such a case, the solution of the internal model of the crystallization process is used to predict the evolution of the mass fractions. This ensures that the PI-controller still receives realistic control deviations. The output of the model based controller,

$$T_w^{(T1)} = T_w^{(T2)} - \Delta T, \tag{3.54}$$

is the continuously updated temperature setpoint for the slave crystallizer. It consists of the isothermal operating point $T_w^{(T2)}$ of the master tank and the output ΔT of the PI-controller. For the first implementation and testing of the model based controller, the mathematical description of the process is kept very simple and only considers growth of the seeded enantiomers. For every time step, a valid measurement is available the initial conditions (liquid phase concentrations, masses of seeds) of the model are fitted by applying recursive Least-Squares-Estimation. In that way, the model solution is permanently updated, to reflect the current and past measured process states.

3.2.3 Constant supersaturation control

The second control strategy uses the same approach as the previous one concerning the computation of a smooth signal for the input of the PI-controller. In this case, since both coupled crystallizers are operated at constant supersaturation, the estimator/filter calculates estimates of the current supersaturation of the respective counter enantiomers, $\hat{S}_I^{(c,j)}$, in each tank j. Figure 3.7 shows the core of the controller structure. Again, the analytical devices provide measurements of the liquid phase concentration, which are processed to compute the control errors,

$$\hat{e}^{(c,j)} = \hat{S}_I^{(c,j)} - S_w^{(c,j)}, \tag{3.55}$$

where S$_w$ denotes the supersaturation setpoint.

The temperature outputs of the PI-controllers, $\Delta T^{(j)}$, are then added to the respective operating point, $\hat{T}_{sat}^{(c,j)}$, which is an estimate of the current saturation temperature of each counter enantiomer. The new setpoints, $T_w^{(j)}$, are subsequently passed to each of the two thermostats that control the crystallizer temperatures.

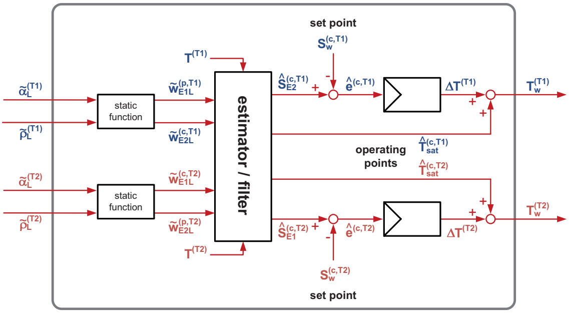
set point
$S_w^{(c,T1)}$
$T^{(T1)}$
$\tilde{\alpha}_L^{(T1)}$
$\tilde{w}_{E1L}^{(p,T1)}$
static function
$\tilde{\rho}_L^{(T1)}$
$\tilde{w}_{E2L}^{(c,T1)}$
estimator / filter
$\hat{S}_{E2}^{(c,T1)}$
+
-
$\hat{e}^{(c,T1)}$
$\Delta T^{(T1)}$
+
+
$T_w^{(T1)}$
operating points
$\hat{T}_{sat}^{(c,T1)}$
$\hat{T}_{sat}^{(c,T2)}$
$\tilde{\alpha}_L^{(T2)}$
$\tilde{w}_{E1L}^{(c,T2)}$
static function
$\tilde{\rho}_L^{(T2)}$
$\tilde{w}_{E2L}^{(p,T2)}$
$\hat{S}_{E1}^{(c,T2)}$
+
-
$\hat{e}^{(c,T2)}$
+
+
$\Delta T^{(T2)}$
$T_w^{(T2)}$
$T^{(T2)}$
$S_w^{(c,T2)}$
set point

Figure 3.7: Controller structure for constant supersaturation control of coupled PC.

3.2.4 Process optimization

In the two previous sections, a simple mathematical description of the process was used to realize feedback control strategies that can improve the performance of CPC. In this section, an optimization procedure is introduced, which uses the complete (moment) model (cf. section 3.1.5) with all available kinetic descriptions. The aim is to calculate a temperature trajectory that maximizes the solid mass of preferred enantiomer at the end of a fixed batch duration, while maintaining a certain product purity. The optimization problem can thus be formulated as,

$$\begin{aligned} &\max_{T^{(j)}(t)} && m_{IS}^{(p,j)}(t_{end}) \\ &subject\ to: && Pu_{\min} \le Pu^{(p,j)}(t_{end}) \end{aligned} . \tag{3.56}$$

It would be very inefficient though to vary the temperature trajectory at every individual time step of the ODE solver to find an optimal curve. In order to keep the computational effort reasonably low, it was approximated. One way to do so is to discretize the time domain and assume constant, linear or nonlinear profiles in each time interval. This is a very straight forward and easy to implement approach and essentially turns the dynamic optimization into a parameter estimation problem.

Here we follow a procedure, which uses spline interpolation in order to calculate optimal temperature profiles for CPC. The routine is based on the optimization of conventional PC described in Angelov, et al. (2008a) where B-Splines (de Boor (1972)) were used to parameterize the temperature trajectory. This approach again leads to a parameter estimation problem. The B-Spline curve B(t), shown in Figure 3.8a, is a polynomial function that will eventually represent the optimal temperature profile. It is a function of a parameter, here the process time t, and is a linear combination,

$$B(t) = \sum_{i=0}^{n} C_i N_{i,d}(t)\,. \tag{3.57}$$

of a set of basis functions $N_{i,d}(t)$ of degree d. The coefficients C_i control the shape of the curve B(t) and are those parameters that will be varied during the optimization. In the example shown in Figure 3.8a, the underlying basis functions are third degree polynomials, i.e. d = 3. Each k^{th} degree basis function is calculated for all t with the recursion formula,

$$N_{i,k}(t) = \frac{t - u_i}{u_{i+k} - u_i} N_{i,k-1}(t) + \frac{u_{i+k+1} - t}{u_{i+k+1} - u_{i+1}} N_{i+1,k-1}(t), \quad k = 1,\ldots,d\,. \tag{3.58}$$

The algorithm starts with the definition,

$$N_{i,0}(t) = \begin{cases} 1, & u_i \le t < u_{i+1} \\ 0, & otherwise \end{cases} \tag{3.59}$$

for the zeroth degree (k = 0) basis function. The knot vector U = {u_0, u_1, …, u_i, …, u_m} is essentially a discretized version of parameter t and determines, on which interval [u_i, u_{i+1}], each basis function $N_{i,d}(t)$ becomes nonzero. The vector U contains m+1 entries, where m = n + d + 1, with n+1 being the number of control points C_i and d the highest chosen polynomial degree.

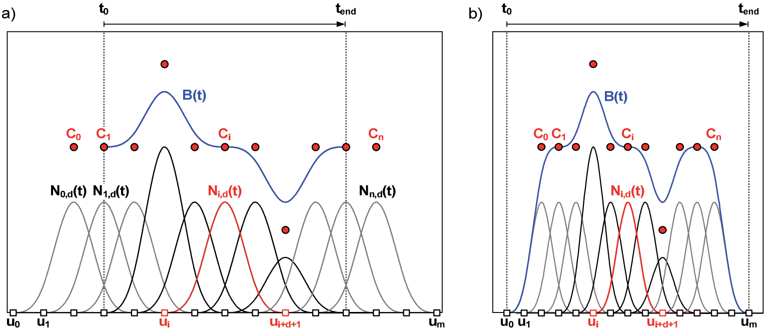

Figure 3.8: Clamped (a) and open (b) B-Spline curves B(t), and their underlying basis functions $N_{i,d}(t)$.

The curve B(t) in Figure 3.8a is a so called clamped B-Spline curve. Usually the knot sequence spans the range of the parameter, i.e. $u_0 = t_0$ and $u_m = t_{end}$, which results in an open B-Spline curve as shown in Figure 3.8b. Due to the algorithm (eqs. (3.58) and (3.59)), the curve starts and ends at a value of Zero, which is not always applicable for a temperature trajectory to be used for the intended crystallization process. To let the curve begin and finish at practically reasonable values, the first and last d knots (here d = 3) are moved outside the domain of t to obtain the curve in Figure 3.8a. The de Boor-algorithm in eqs. (3.58) and (3.59) is visualized in Figure 3.9 as a triangle diagram for more clarity. In the specific example, a cubic B-Spline curve (d = 3) with a total of five (n = 4) control points C_i is calculated. This requires nine knots u_i (m = 8). On the far left, the knot intervals are indicated for i = 0…m. The control points C_i for i = 0…n are on the far right. Obviously, each control point is associated with one of the n+1 third degree basis functions. Starting at d = 0, it can be seen that with increasing degree, the basis functions $N_{i,k}$ cover wider knot intervals across which they are nonzero. The highlighted function $N_{1,3}$, for example, spans the interval $[u_1, u_5]$, whereas $N_{1,0}$ has local support on $[u_1, u_2]$. In general, a basis function $N_{i,d}$ extends across an interval $[u_i, u_{i+d+1}]$ as is also shown in Figure 3.8. This results in the property of B-Splines called local support, which is one of their main advantages. Thus, changing the value of one control point only affects the curve within a certain interval but does not change the shape over the entire domain of the parameter t or the knot sequence U, respectively.

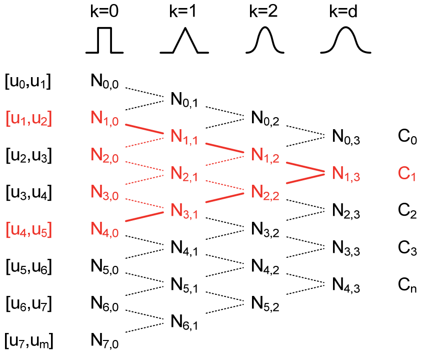

Figure 3.9: Triangle diagram, visualizing the de Boor-algorithm (eqs. (3.58), (3.59)). The construction of the third degree basis function for i = 1, $N_{1,3}$, is highlighted. Clearly, $N_{1,3}$ is nonzero across the interval $[u_1, u_5]$.

The optimization problem stated at the beginning (eq. (3.56)), can now be formulated in terms of the free parameters C_i,

$$\begin{array}{ll} \max\limits_{C_i^{(j)}} & m_{IS}^{(p,j)}(t_{end}) \\ subject\ to: & Pu_{\min} \le Pu^{(p,j)}(t_{end}) \\ & \dfrac{dT^{(j)}(t)}{dt} \le \left|\dot{T}_{\max}\right| \\ & T^{(j)}(t) \ge T_{\min} \end{array} \tag{3.60}$$

The additional constraints indicate the maximum cooling (or heating) rate, $\dot{T}_{\max}$, of the respective thermostat, as well as the lowest allowed temperature $T_{\min}$. Optimization was done over many iterations using the GLOBALSEARCH and PATTERNSEARCH algorithms contained in the global optimization toolbox of Matlab. The initial conditions of the liquid and solid phase were based on the experimental conditions of the coupled benchmark experiment discussed in chapter 5.3.1. Additional model parameters specific to threonine are given in the following chapter.

3.3 List of model parameters

The model described by eqs. (3.2) - (3.24), contains parameters specific to threonine that have been determined in previous works (Elsner, et al. (2011)). Table 3.1 summarizes all parameters and their values used for the simulations in this work. Ten specific parameters related to growth, secondary and primary nucleation were estimated using experiments discussed in chapter 5. The optimal values are given in Table 5.2 therein.

Table 3.1: Model parameters for the simulation of preferential crystallization of threonine.

parameter	*value*	*unit*	*description*
a_2	-0.1043	-	solubility correlation, influence of opposite enantiomer
a_1	-0.078	-	solubility correlation, influence of opposite enantiomer
m_{sol}	1.15e-3	1/°C	solubility correlation, temperature influence
b_{sol}	5.9601e-2	-	solubility correlation, temperature influence
k_V	0.122	-	volumetric shape factor (value corresponds to seeds)
ρ_S	1250	kg/m^3	density of solid threonine
K_1	1.00023	cm^3/g	water density correlation
K_2	4.681e-6	$cm^3/(g\ °C^2)$	water density correlation
K_3	0.3652	g/cm^3	solution density correlation
k_W	135.5	$J/(s\ K\ m^2)$	heat transfer coefficient
A_W	3.02e-2	m^2	heat exchange area of the inner crystallizer wall
c_{pL}	4183.2	J/(kg K)	mean specific heat capacity of threonine solutions
Δh_{cryst}	-73.5e-3	kJ/kg	specific crystallization enthalpy
k_{g0}	**estimated**	$m\ s^{-1} s^{n_g}$	pre-exponential coefficient (growth)
E_{Ag}	**estimated**	kJ/mol	activation energy (growth)
n_g	0.4573	-	stirrer speed correlation (growth)
g	**estimated**	-	power-law exponent (growth)
k_{bsec0}	**estimated**	$s^{-1} m^{-3n_{\mu 3}}$	pre-exponential coefficient (sec. nucleation)
E_{Absec}	63.83	kJ/mol	activation energy (sec. nucleation)
n_{bsec}	30.377	rad/s	stirrer speed correlation (sec. nucleation)
b_{sec}	**estimated**	-	power-law exponent (sec. nucleation)
$n_{\mu 3}$	**estimated**	-	exponent of third moment (sec. nucleation)
k_{bprim1}	**estimated**	$s^{-1} K^{-1} m^7 kg^{-7/3}$	pre-exponential coefficient (prim. nucleation)
k_{bprim2}	**estimated**	-	exponential coefficient (prim. nucleation)
K_{Tvisc}	1874.4	K	viscosity related parameter (prim. nucleation)
K_{wvisc}	0.29	-	viscosity related parameter (prim. nucleation)
A_{prim}	**estimated**	$m^{-2n_{\mu 2}}$	coefficient of heterogeneous contribution (prim. nucleation)
$n_{\mu 2}$	**estimated**	-	exponent of heterogeneous contribution (prim. nucleation)
k_d	3e-5	$m\ s^{-1}$	dissolution rate constant (dissolution)
d	1	-	power-law exponent (dissolution)

4 Experimental part

4.1 Model system DL-threonine-water

L-Threonine belongs to the group of proteinogenic α-amino acids with an uncharged polar side chain. It is one of the nine essential amino acids that have to be provided by proper nutrition, since humans and most other mammals are not able to synthesize them [Löffler, Petrides]. Especially in the livestock industry it is therefore used as a dietary supplement, since many crops contain insufficient amounts of essential amino acids.

When looking at the chemical structure of threonine in Figure 4.1, we notice two carbon atoms (C_α (2) and C_β (3)), each with four different substituents. These two chiral centers result in the existence of four stereoisomers.

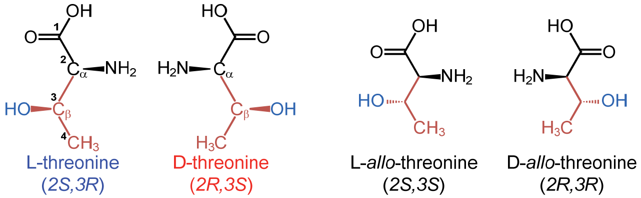

Figure 4.1: The four stereoisomers of threonine result from the two stereogenic (chiral) centers.

Owing to the polar nature, which is contributed by the hydroxyl group, threonine is moderately soluble in water. It is, however, virtually insoluble in ethanol. The enantiomers D- and L-threonine in water were selected as a model system to study batch PC because it is well characterized regarding solubility (Profir, et al. (2000)), Sapoundjiev, et al. (2006)) and metastable zone width (Lorenz, et al. (2006)). Furthermore, it forms a racemic conglomerate, which makes it a perfect candidate for a crystallization based separation.

The raw material used to prepare the initial racemic solutions for all experiments was purchased from Sigma-Aldrich and consisted either of the two pure enantiomers (L- and D-Thr, purity > 98%) or the racemate (DL-Thr, purity > 98%).

4.1.1 Solubility and metastable zone width of threonine

The solubility of threonine in water is shown in Figure 4.2 for different temperatures and compositions. All values are given in terms of weight fractions (i.e., mass solute per mass solution). Figure 4.2a shows the solubility of pure L-Thr (E1) and the racemate (rac) in water. The solid lines represent the calculated solubility based on the correlation fitted in the course of this work,

$$w_{IL,eq}^{(k,j)}(T) = \underbrace{-0.1043}_{a_2} \cdot \left(w_{I^*L}^{(k,j)}\right)^2 \underbrace{-0.078}_{a_1} \cdot w_{I^*L}^{(k,j)} + \underbrace{1.15 \cdot 10^{-3}}_{m_{sol}} \cdot T^{(j)} + \underbrace{5.96 \cdot 10^{-2}}_{b_{sol}}, \qquad (4.1)$$

(compare eq. (3.17)). Threonine behaves nearly ideally since the solubility of the racemate is almost double (α = 2) that of the single enantiomer. This ideal case is indicated by the dashed line in Figure 4.2a. The actual mean value is α = 1.84 for the investigated temperature range (10 – 50 °C). Additional equilibrium compositions are shown in the ternary phase diagram in

Figure 4.2b. This representation further illustrates the fact that threonine belongs to the group of conglomerates, showing a single eutectic point for each temperature.

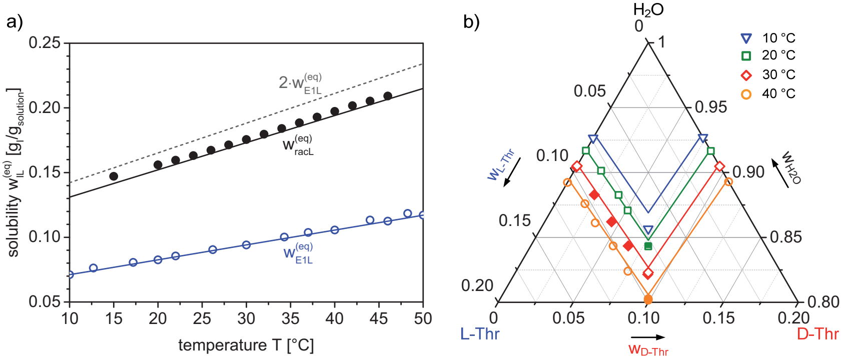

Figure 4.2: a) Solubility of L-Thr and the racemate in water. Symbols are measured, lines calculated values using the fitted solubility correlation (eq. (3.17)). b) Ternary phase diagram of the DL-Thr/water system for a temperature range of 10 to 40 °C. Open symbols represent solubility data reported by Sapoundjiev et al. (2006). Solid symbols in b) are own measurements. The lines are calculated values (eq. (3.17)).

The data represented by open symbols were obtained by Sapoundjiev et al. (2006), whereas solid symbols show own measurements performed in the crystallizers used in this work (see section 4.2). The solid lines again show the calculated solubility (eq. (3.17)).

Apart from solubility, the metastable zone width (MZW) is a crucial quantity for preferential crystallization. As soon as a solution is below the saturation temperature, the chance of primary nucleation is elevated and increases with further cooling. Commonly, the MZW is given for a fictitious cooling rate of 0 K/h as a safe band. Solutions saturated at various temperatures are subcooled at different cooling rates and the temperatures T_{nuc}, at which the nucleation event is detected is used to calculate the corresponding temperature difference $\Delta T = T_{sat} - T_{nuc}$ (Nývlt (1985)). The maximum possible degree of supercooling ΔT_{MZW} is obtained by extrapolation.

Values for the metastable zone width of DL-threonine are reported to be in the range of 8 - 9 K (Lorenz, et al. (2006), Polenske (2010)) for a cooling rate of 0 K/h. At higher rates (i.e., > 15 K/h), it can exceed a width of 20 K (Polenske (2003)), which was also confirmed by measurements performed in the crystallizers used in this work. (see Appendix 7.3).

4.2 Plant setup

All crystallization experiments were performed in either one (conventional PC) or two (CPC, CPC-D) identical jacketed glass reaction vessels with a working volume of 450 ml and an inner diameter of 100 mm. Figure 4.3 and Table 4.1 provide an overview of the plant and the peripheral instrumentation. Each crystallizer was equipped with a thermostat for closed-loop temperature control of the suspension. Mixing was done with teflon coated 3-blade propeller type stirrers with a diameter of 70 mm. The reconstruction of the enantiomer concentrations was based on two at-line measurement signals, density and optical rotation angle (QIR, DIR). Crystal free liquid was continuously pumped through the analytical path and back to the crystallizer by peristaltic pumps (F_A). The teflon tubes were heated to at least 0.5 K above the initial solution saturation temperature to prevent blockage.

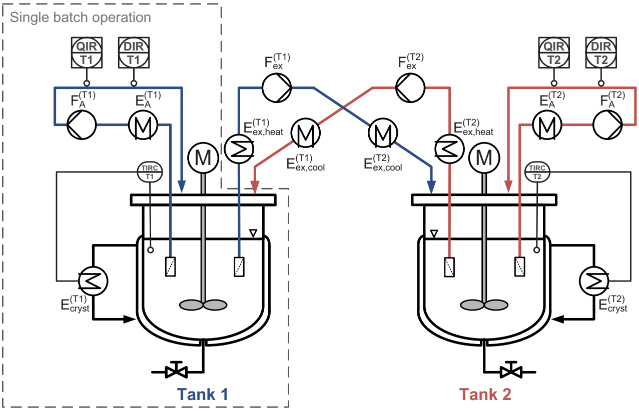

Figure 4.3: PI flow diagram of the crystallization plant used for single and coupled batch operation. Fines removal loops are not shown (compare Figure 4.5).

In coupled mode, both vessels were connected via the liquid phase by a continuous exchange of crystal free solution through heated silicon tubes. The peristaltic pumps F_{ex} were identical to those of the analytical loops. In all cases where particle free solution was transported (analytics, exchange), HPLC frits with a pore size of 0.22 µm were used. For the solution exchange, each crystallizer was equipped with two frits connected to the exchange path via three-way valves to facilitate replacement of blocked filters.

Table 4.1: List of the plant instrumentation.

instrument	*PI label*	*function*	*manufacturer*	*model*
Crystallizer	Tank j	reaction vessel	HWS-Labortechnik	-
Stirrer motor	M	mixing	Heidolph	RZR 2102 control
Thermostat	E_{cryst}	crystallizer heating/cooling	Lauda	Proline RP 845
	$E_{ex,heat}$	exchange tube heating	Julabo	FS 18
	$E_{ex,cool}$	exchange tube recooling	Lauda	Ecoline RE 104
	E_A	analytics heating	Julabo	FS 18
Pt-100	TIRC	temperature indication, registration, control	Alhorn	-
Peristaltic pump	F_{ex}	volumetric exchange flow rate	Heidolph	PD 5201 SP Quick
	F_A	volumetric analytics flow rate	Heidolph	PD 5201 SP Quick
Density meter	DIR	density, indication, registration	Mettler Toledo	DE40
Polarimeter	QIR	optical rotation angle, indication, registration	IBZ Messtechnik	POLARmonitor

4.3 Process observation and balancing

As mentioned in the previous section, the concentration of each enantiomer in the liquid phase was monitored by measurement of the optical rotation angle and the density. The angle of rotation is measured by passing linearly polarized light with a wave length of 589 nm through the sample, which in the case of optically active substances, rotates the plane in which the light waves oscillate. The sample cell used in the experiments had a length of 5 cm and was kept at a temperature above saturation. The density of the solution was measured using the principle of an oscillating U-tube.

For balancing and subsequent modeling of the PC processes, the liquid phase monitoring was used to track the dynamic composition and concentration of the liquid phase with respect to both enantiomers. Since there are two unknown concentrations expressed as mass fractions w_{IL} (g solute I / g solution), two signals are required. The solution density ρ_L reflects the sum of both concentrations, w_{IL}, while the optical rotation angle α_L provides the difference. This can be expressed by the following two linear equations for density,

$$\rho_L = k_d \cdot (w_{E1L} + w_{E2L}) + \rho_0 , \tag{4.2}$$

and the optical rotation angle,

$$\alpha_L = k_{pol} \cdot (w_{E2L} - w_{E1L}) \tag{4.3}$$

that relate the measured quantity with the mass fractions of the dissolved enantiomers. They contain the parameters k_d, ρ_0 and k_{pol}, which have to be determined by calibration. By combining eqs. (4.2) and (4.3), we get two equations for the unknown mass fractions w_{E1L},

$$w_{E1L}(t) = \frac{1}{2}\left(\frac{\rho_L(t) - \rho_0}{k_d} - \frac{\alpha_L(t)}{k_{pol}} \right), \tag{4.4}$$

and w_{E2L},

$$w_{E2L}(t) = \frac{1}{2}\left(\frac{\rho_L(t) - \rho_0}{k_d} + \frac{\alpha_L(t)}{k_{pol}} \right). \tag{4.5}$$

With the closure condition,

$$\sum_I w_{IL} = 1, \qquad I = E1, E2, H2O , \tag{4.6}$$

the mass fraction of the solvent H_2O is known . Using the definition of mass fractions in the liquid phase,

$$w_{IL}(t) = \frac{m_{IL}(t)}{\sum_{I=1}^{2} m_{IL}(t) + m_{H2O}} , \tag{4.7}$$

and assuming that the mass of solvent m_{H2O} remains constant (i.e., no evaporation), it is possible to obtain the dissolved masses of each enantiomer,

$$m_{IL}(t)=\frac{w_{IL}(t)\cdot m_{H2O}}{1-\sum_{I=1}^{2}w_{IL}(t)}\,. \tag{4.8}$$

Since the initially dissolved mass of racemate m_{racL0} is known, one can also calculate the evolution of the solid masses for each enantiomer, m_{IS},

$$m_{IS}(t)=\frac{1}{2}m_{racL0}-m_{IL}(t)+m_{Iseeds}\,, \tag{4.9}$$

which contains the mass of seeds m_{Iseeds} added to the system. In case of the coupled process it has to be assumed that the exchange is infinitely high in order to use eq. (4.9). This assumption is approximately valid in the experiments. As a result, the liquid mass of one enantiomer can be assumed to decrease by the same amount in each of the two crystallizers j = T1, T2. With double the amount of raw material the equation then becomes,

$$m_{IS}^{(j)}(t)=m_{racL0}^{(j)}-2m_{IL}^{(j)}(t)+m_{Iseeds}^{(j)}\,. \tag{4.10}$$

Finally, three important performance quantities can be reconstructed. The relative yield is defined as,

$$Y_I(t)=\frac{m_{IS}(t)-m_{Iseeds}}{m_{IS,eq}(T)}\,, \tag{4.11}$$

and contains the maximum amount of solid, $m_{IS,eq}$, that can crystallize at a given temperature under the chosen process conditions. It is calculated on the basis of the eutectic equilibrium concentration. The purity of the solid phase with respect to enantiomer I is given by,

$$Pu_I(t)=\frac{m_{IS}(t)}{\sum_{I=1}^{2}m_{IS}(t)}\,. \tag{4.12}$$

The productivity of the process is defined as,

$$\mathrm{Pr}_I(t)=\frac{m_{IS}(t)-m_{Iseeds}}{0.5\,m_{racL0}\cdot\left(t+t_{idle}\right)}\,, \tag{4.13}$$

and indicates the amount of pure enantiomer I obtained from half the mass of racemic starting material per unit time. The time for preparation of a batch process, t_{idle}, was estimated to take 2 h for all process options presented in this work. It includes cleaning, dissolution of the raw material, subcooling and seeding.

In many cases, a process will yield a high productivity, which is, however, accompanied by a low purity. To account for this it may be reasonable to use a weighted productivity Pr_{Iw},

$$\mathrm{Pr}_{Iw}(t)=\mathrm{Pr}_I(t)\cdot Pu_I(t)\,. \tag{4.14}$$

The weighted productivity is more suitable to directly compare the performance of different preferential crystallization runs.

In chapter 5.7 the enantiomeric excess of the solid phases is used in the context of a theoretical analysis of the process concepts. It is defined for each tank j as,

$$ee^{(j)} = \frac{\left|m_{E1S}^{(j)} - m_{E2S}^{(j)}\right|}{m_{E1S}^{(j)} + m_{E2S}^{(j)}}. \tag{4.15}$$

The above equations (4.2) - (4.14) are applicable to all process concepts treated in this thesis. However, care has to be taken when calculating the liquid and solid masses in case of coupled preferential crystallization (CPC). Because of the exchange of solution between both crystallizers, the decrease in concentration of one enantiomer can either be the result of the seeds growing or it can be caused by a nucleation event of the same enantiomer in the opposite crystallizer. The calculated masses of dissolved enantiomer only reflect the real masses when no nucleation of the respective counter enantiomer occurs. Otherwise, it is not possible to reconstruct the true masses and additional information about the current composition of the solid phases accumulating in each vessel is necessary. At times, the reconstructed masses are used to calculate productivity trends based on the analytical signals. Keeping in mind the above mentioned difficulty, they still present valuable information about the process performance, especially when the final product purity was found to be very high.

4.4 Data logging and process control

In chapter 3.2, the working principles of symmetry and constant supersaturation control where introduced. The technical implementation, in particular the communication of the involved computers with the plant, is illustrated in Figure 5.6. The densitometers and polarimeters (analytics) where connected to a data logging computer via RS-232 connections. Due to stability issues, the controllers implemented in MATLAB where run on a separate computer directly linked to the crystallizer thermostats. Data exchange between both workstations was done via the local network.

For the uncontrolled processes, crystallizer temperatures and the optical rotation angles were recorded by the software AMR WinControl (akrobit software GmbH, Gera). Density signals were registered with separate software (Data Capture, Mettler-Toledo GmbH).

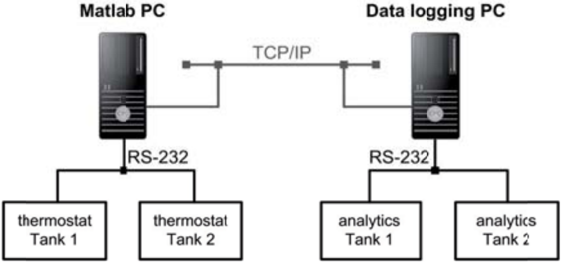

Figure 4.4: Signal network for symmetry and constant supersaturation control.

4.5 Seed crystal preparation

Enantiopure seeds were obtained by sieving of the raw material purchased from Sigma-Aldrich. For every batch of seeds the sieve fraction 150 – 200 µm was taken and washed with ice cold water and ethanol. The crystal size distribution was subsequently determined by manual measurement using digital microscopy (Stemi 2000-C, Zeiss AG). The obtained histograms are shown in Appendix 7.4. Resulting parameters of the fitted log-normal distributions with respect to the characteristic length z_1 (cf. section 3.1) are summarized in Table 4.2. Due to the needle-like shape of threonine crystals the aspect ratio z_1/z_2 is $\gg 1$. As a consequence, the medians of the characteristic length z_1 are larger than the chosen sieve mesh size.

Table 4.2: Seed crystal batches and their log-normal size distribution parameters $\bar{z}_{l,seeds}$ and $\sigma_{l,seeds}$.

	L-threonine		*D-threonine*	
Batch No.	$\bar{z}_{E1,seeds}$ *[µm]*	$\sigma_{E1,seeds}$ *[-]*	$\bar{z}_{E1,seeds}$ *[µm]*	$\sigma_{E2,seeds}$ *[-]*
1	513	0.347	-	-
2	235	0.517	510	0.394
3	534	0.437	392	0.479
4	528	0.382	463	0.514
5	350	0.481	325	0.519

4.6 Conventional batch operation and general experimental procedures

The procedures concerning preparation and execution of an experiment as well as the subsequent processing of the obtained product are generally the same for all process options considered in this work. They are therefore mentioned in the context of conventional batch operation. Steps that are specific to the other processes are pointed out in the respective sections of chapter 5.

The term conventional batch operation is used here to denote all experiments performed in a single crystallizer. Table 4.3 summarizes the standard operating conditions for conventional PC. Experimental conditions that differ from these default values are mentioned explicitly for the respective experiment in section 6. In all cases, purified water (Milli-Q) was used as solvent.

The preparation of every experiment was done according to the following procedure. The total amount of each enantiomer was split into at least four parts for the calibration of the analytical devices. The indicated amount of water was added and heated to 50 °C to ensure quantitative dissolution. Once all temperatures (crystallizer, analytics) were at steady state, threonine standards were added one at a time and the system was allowed to equilibrate for at least 10 min following each addition. The resulting density and optical rotation angle values together with the added amounts of each enantiomer were then used to construct the calibration curves. The values of the calibration parameters k_d, ρ_0 and k_{pol} in eqs. (4.2) and (4.3) were obtained by linear regression.

Table 4.3: Standard (initial) operating conditions for conventional batch PC. L-Thr was the seeded enantiomer in most cases.

description	*process parameter*	*value*
mass of solvent	m_{H2O}	359.19 g
mass of L-Thr	m_{E1}	45.405 g
mass of D-Thr	m_{E2}	45.405 g
mass of L-Thr seeds	$m_{E1seeds}$	1.0 g
saturation temperature	T_{sat}	43.7 °C (eq. (3.17))
crystallization temperature	T_{cryst}	30 °C
subcooling rate	$\dot{T}$	-14 K/h or faster
stirrer speed	N_{St}	300 min^{-1}
analytics flow rate	F_A	3.5 ml min^{-1}
analytics temperature	T_A	46 °C

Subsequently the racemic solution was cooled to the final crystallization temperature T_{cryst} at a rate of at least -14 K/h. Seeds were added once the solution had reached a stable temperature. In order to stop the separation process, the slurry was discharged and immediately filtered using a Büchner funnel connected to a vacuum pump. The filter cake was washed with ice cooled water to remove remaining mother liquor from the crystals and ethanol to displace water residues. The product was then placed into a desiccator for drying until constant weight was reached, which was determined by an analytical balance (XS205, Mettler-Toledo). Depending on the amount of material, drying took two to five days. Subsequent characterization of the crystalline product comprised the determination of the crystal size distribution by optical microscopy and a purity analysis by HPLC (1260 Infinity, Agilent Technologies) using an analytical column for chiral separation (Astec Chirobiotic T, Sigma-Aldrich). The mobile phase consisted of a 70:30 v/v (Ethanol/H_2O) mixture.

4.7 Coupled batch operation

For the coupled PC processes, each of the two crystallizers and the analytics were prepared following the same procedure as described in the previous section regarding classical PC. The standard operating conditions were identical to those listed in Table 4.3. Additional process parameters that are specific to CPC are summarized in Table 4.4.

In order to avoid temperature fluctuations, once the solutions had reached the final crystallization temperature, the solution exchange was activated prior to subcooling. Both crystallizers were then seeded simultaneously. During the separation process, the main challenge was the blockage of the exchange filters. They were replaced by unused filters at least on an hourly basis to maintain constant equal flows and thereby avoid differences in solution volume between both crystallizers.

Table 4.4: Additional process parameters specific to coupled preferential crystallization.

description	*process parameter*	*value*
mass of E1 seeds Tank 1	$m_{E1seeds}^{(T1)}$	0.5 g
mass of E2 seeds Tank 2	$m_{E2seeds}^{(T2)}$	0.5 g
exchange flow rate	F_{ex}	50 ml min^{-1}
exchange path temperature	T_{ex}	46 °C

Mass and composition of the solid material adhering to the exchange filters were determined for all polythermal CPC processes performed at the later stage of this work. During early experiments this was not done.

All filters from each crystallizer were rinsed with purified water in an ultrasonic bath to dissolve the adhering crystals. Subsequently the solutions were placed in a rotary evaporator to remove the solvent and stored in a desiccator until constant weight was achieved. The composition was then determined by chiral HPLC analysis.

4.8 Fines dissolution

For the operation of conventional and coupled PC with fines dissolution, each crystallizer of the plant depicted in Figure 4.3 was equipped with an additional loop through which the suspension was circulated as shown in Figure 4.5a. The setup consisted of a silicon tube divided into a heated (length 2.16 m) and a cooled (length 3 m) section each with an inner diameter of 3.2 mm, to which the fines dissolution filter was connected (Figure 4.5b).

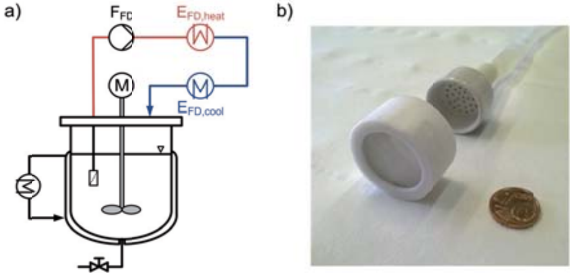

Figure 4.5: Crystallizer with the additional heated loop for fines dissolution (a). Fines dissolution filter built from a wire mesh with a spacing of 500 µm and a Büchner funnel for support of the cap (b).

The operating conditions of the fines dissolution unit are summarized in Table 4.5.

Table 4.5: Operating conditions of the fines dissolution unit.

description	*process parameter*	*value*
high temperature	$T_{FD,heat}$	60 °C
low temperature	$T_{FD,cool}$	25 °C
fines diss. flow rate	F_{FD}	40 ml min^{-1}
filter cut-off size	d_{FD}	500 µm

4.9 Overview of experiments

In this work three types of process strategies were investigated. Conventional preferential crystallization in a single crystallizer, coupled preferential crystallization and coupled preferential crystallization with selective dissolution. The first two concepts were additionally studied in connection with fines dissolution. A strong focus was put on the coupled concepts involving a detailed study of polythermal operation.

Table 4.6 summarizes the experiments discussed in chapter 5. A more detailed list including process conditions is given in Appendix 7.1 and 7.2.

Table 4.6: Overview of the investigated process strategies for preferential crystallization.

type	*description*	*chapter*
PC (conventional preferential crystallization)	isothermal benchmark experiment	5.2.1
PC-FD (conventional PC with fines dissolution)	investigation of fines dissolution	5.2.2
CPC (coupled preferential crystallization)	benchmark experiment	5.3.1
CPC-FD (coupled CPC with fines dissolution)	investigation of fines dissolution	5.3.3
CPC (coupled preferential crystallization)	polythermal operation	5.3.5
	symmetry control	5.4.1
	constant S-control	5.4.2
	optimized trajectory	5.4.3
CPC-D (coupled preferential crystallization with selective dissolution)	proof of principle	5.5

5 Results and discussion

5.1 Parameter estimation and preliminary simulation study

5.1.1 Parameter estimation

The mathematical model presented in chapter 3 contains an abundance of parameters that are not entirely accessible by experimental procedures. It is therefore necessary to obtain estimates for the values of these parameters through parameter optimization.

Previous works by Czapla (Czapla, et al. (2009b); Czapla (2010)) and Ziomek (Elsner, et al. (2011); Ziomek (2011)) have also addressed the issue of parameter estimation in the context of preferential crystallization. Since both authors performed experiments with threonine as well it would seem reasonable to use their models and parameters to simulate the processes done in this work. However, even though their models were calibrated using the same substance system, transferability is not straightforward. It turns out that the model is capable to predict experimental data from various process concepts but only to a certain extent. Each experiment naturally suffers from non-idealities that often cannot be put in a mathematical framework. As a result, a parameter estimation using an already semi-empirical model with lumped parameters will only yield a good fit for a set of experiments with similar imperfections.

Apart from experimental issues, differences in the model structure are another source for discrepancies. Over time, the model has been changed in order to improve its predictive capabilities. For this (and the above) reason, different sets of parameters exist with values specific to the respective model structure but also to the experimental conditions and setups.

In the work of Ziomek a model discrimination was done by successively adapting the primary nucleation kinetics as well as growth kinetics expressions. In particular, Ziomek implemented a size dependent growth rate as suggested by Abegg, et al. (1968) as well as the primary nucleation kinetics given in eq. (3.22). The latter was further adapted in his work to include an additional dependence on the second moment of the seeded enantiomer similar to eq. (3.23) in this work. Furthermore, secondary nucleation kinetics (compare eq. (3.21)) were treated individually for each enantiomer regarding the pre-exponential coefficient $k_{bsec,0}$, which leaves the model with additional degrees of freedom. The final model Ziomek used contained 11 free parameters, which were adjusted using experimental data of one conventional PC experiment. Although the final fit in his work (chapter 4.2.2 therein) is satisfactory, it is surprising that it did not converge to an even better solution. Based on the experience from this work it is generally possible to obtain an almost perfect fit, when only one experiment is used. It therefore seems likely that the parameter optimization done by Ziomek terminated in a local minimum.

In the dissertation of Czapla, nine polythermal experiments were used to perform a very detailed analysis of the parameter estimation problem. Five of them were based on the AS3PC (auto seeded polythermal programmed preferential crystallization) process patented by Coquerel, et al. (2000). Owing to the complex temperature profiles of these processes, a lot of information is contained in the dynamics. In addition, Czapla used an online monitoring of the solid phase to complement the concentration measurement. By doing so, he provided a much higher amount of experimental information, which should in principle lead to better estimates of the free parameters.

Compared to the model used in this work, Czapla's mathematical description slightly differs in terms of growth and nucleation kinetics as well as the calculation of the solubility. Figure 5.1 shows a simulation of the isothermal benchmark experiment, discussed in section 5.2.1, using the model and parameters published in Czapla, et al. (2009b) and Ziomek (2011), respectively. Process conditions for this experiment are summarized in Table 5.3. L-threonine seeds from batch 1 (see Table 5.2) were used for this process.

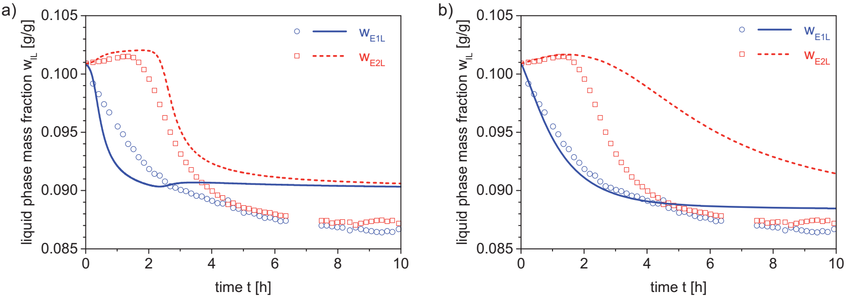

Figure 5.1: Simulation (solid and dashed lines) of the isothermal benchmark experiment (see section 5.2.1) using the model and parameter values reported by Czapla, et al. (2009b) (a) and Ziomek (2011) (b). Symbols denote experimental data from the benchmark experiment PC1 done in this work. E1 is the seeded enantiomer.

In both cases the predictions of the dynamics and final equilibrium state lead to some degree of model mismatch. In case of Czapla's model (Figure 5.1a) this is mainly due to the non-empirical solubility correlation, which predicts equilibrium concentrations that are 3% - 6% higher than the one calculated by the fitted polynomial used in this work (eq. 4.1). Additionally, it can be explained by the type of experiments he used for parameter estimation, which mostly involved the generation of seeds from a clear solution (AS3PC process) or the use of milled seeds. In either case the seed material consisted of very small particles that can show a significant degree of growth rate dispersion (Jones, et al. (1999); Ulrich (1989)). In combination with a slightly different solubility, it is not surprising that the simulation does not entirely predict the experiment.

The solution of the model reported by Ziomek shows better agreement regarding the seeded enantiomer E1, which can be expected since his experiments were performed in an almost identical setup to the one used in this work. Additionally, Ziomek used very similar process conditions regarding seed material, initial solution composition and temperature. The remaining model mismatch is quite small for the seeded enantiomer but still large concerning the dynamics of the unseeded species.

Given the results of these previous works, it seemed reasonable to further explore the capabilities of the model. This is essentially a continuation of the work of Ziomek, however, involving more experimental data from processes with different conditions, thus following the approach of Czapla. During initial parameter estimation attempts, the model was slightly changed compared to the version in Ziomek (2011). The adaptations eventually led to the model presented in chapter 4, which includes the following simplifications and changes:

- removal of size dependent growth (- 2 parameters)
- identical secondary nucleation kinetics for both enantiomers (- 1 parameter)
- modified primary nucleation kinetics (+ 1 parameter)
- modified solubility correlation

In summary, the model presented in chapter 4 is reduced by two degrees of freedom, concerning crystallization kinetics, compared to the final version in Ziomek (2011). Ten of the parameters summarized in Table 3.1 were chosen to be estimated using experimental data from this work. Their optimal values are given in Table 5.2 of this chapter.

Due to the highly non-linear model and cross correlated parameters an almost perfect fit of the model solution to a single experiment can be obtained. An illustrative example is shown in Figure 5.2a where the ten parameters were adjusted using only experiment PC2. Under slightly different process conditions, however, the same parameter values do not produce the same quality of agreement as shown in Figure 5.2b for experiment PC4.

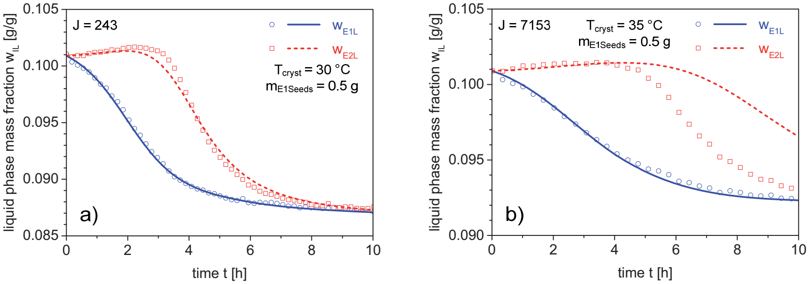

Figure 5.2: a) Resulting model fit when only experiment PC2 is used for parameter estimation. b) The obtained optimal parameter values applied to experiment PC4 do not produce the same quality of agreement, which is also reflected by the value of the objective function J (eq. 3.49).

In order to increase the amount of information about the behavior of preferential crystallization, six conventional and five coupled preferential crystallization experiments with different process conditions were selected and used simultaneously for the parameter estimation. The experiments and important experimental conditions are listed in Table 5.1. A full summary is given in Appendix 7.1.

The experiments were selected to be used for the parameter estimation on the basis of the crystallization temperature (T_{cryst}), mass (m_{seeds}) and size of the seeds ($\bar{z}_{I,seeds}$). The influence of the stirrer speed (N_{St}) was not a main focus although it is considered in the model and affects growth and secondary nucleation kinetics. Its values are listed for the sake of completeness. Crystallization temperatures in brackets signify polythermal experiments.

Table 5.1: Overview of important experimental conditions of conventional (PC) and coupled preferential crystallization (CPC) processes used for parameter estimation. The initial solutions all had a concentration of w_{IL0} = 0.1009 g/g, which corresponds to a saturation temperature of T_{sat} = 43.7 °C. Additional process conditions are given in Appendix 7.1. The PC processes were seeded with L-Thr. The CPC processes were seeded with L- and D-Thr in Tank 1 and Tank 2, respectively. Experiments CPC2 and 3 were not used for parameter estimation.

Experiment	T_{cryst} *[°C]*	m_{seeds} *[g]*	$\bar{z}_{I,seeds}^{(Batch)}$ *[μm]*		N_{St} *[min^{-1}]*
PC1	30	1.0	513 $^{(1)}$		300
PC2	30	0.5	528 $^{(4)}$		300
PC3	30	2.0	534 $^{(3)}$		250
PC4	35	0.5	260 $^{(*)}$		250
PC5	[30,22]	0.5	534 $^{(3)}$		250
PC6	[34,29]	0.5	534 $^{(3)}$		300
			Tank 1	*Tank 2*	
CPC1	30	0.5	534 $^{(3)}$	392 $^{(3)}$	250
CPC4	[30,10]	0.5	350 $^{(5)}$	325 $^{(5)}$	250
CPC5	[30,20]	0.5	350 $^{(5)}$	325 $^{(5)}$	250
CPC6	[30,20]	0.5	350 $^{(5)}$	325 $^{(5)}$	250
CPC7	[30,10]	0.5	350 $^{(5)}$	325 $^{(5)}$	250

$^{*)}$ Batch of L-Thr seeds used only in this particular experiment ($\sigma_{E1,seeds}$ = 0.734)

Initially all 11 experiments – conventional and coupled PC – were considered simultaneously for the estimation of the parameters. It was, however, not entirely possible to obtain a single set of parameter values that would satisfy both process strategies. Although very good fits could be produced regarding the liquid phase concentrations, the predicted purities of the solid phases in case of CPC differed significantly from the experimental observations. Apparently, there are differences between the two process types that are not yet considered by the model. This can partly be due to the fact that during conventional PC, the liquid phase is temporarily enriched with respect to the unseeded enantiomer, which is not the case during CPC where the liquid phase remains racemic. Whether this may affect the crystallization kinetics should be clarified in future works. Apart from this, the solution exchange necessary for coupled PC results in an unavoidable removal of solid material, whenever the filter frits are replaced after blockage. In chapter 5.3.5 it is shown that a significant amount of crystals can adhere to the filters, which also contains high amounts of nucleated impurity. This solid discharge is not considered in the mathematical model as it would require a detailed understanding of how the filter cake builds up in an agitated suspension and which fractions of the crystal populations are actually withdrawn. Regarding such technical issues, the conventional PC experiments are much closer to an ideal process because such artificial disturbances are avoided. With the current model, but also the experimental setup, it is therefore necessary to distinguish between the two different process options.

As a consequence, the six conventional PC experiments and the five coupled PC experiments were treated separately. The two resulting sets of optimal parameter values are given in Table 5.2. They were obtained according to the procedure described in chapter 3.1.8.

The objective function (OF) was calculated according to eq. (3.50) using the liquid phase concentrations, w_{IL}, measured by the atline analytics (cf. section 4.3). Its final optimal value was J = 1731 for the conventional PC experiments and J = 6633 for the coupled PC processes. The upper and lower bounds in Table 5.2 were chosen to ensure numerical stability during the optimization procedure. They are the result of empirical adjustments done over the course of many repeatedly performed optimization runs, since initial attempts tended to fail.

Table 5.2: Optimal parameter values obtained from estimation using the six conventional PC and five coupled PC experiments (PC and CPC). The index I = E1, E2 is omitted since the parameters apply to both enantiomers.

No.	*kinetics*	*parameter*	*optimal values PC*	*optimal values CPC*	*bounds*		*unit*
					lower	*upper*	
1	growth	$k_{g,0}$	3.6767e6	8.5109e6	1e5	5e7	$\mathrm{m\,s^{-1}s^{n_g}}$
2		E_{Ag}	76.0600	76.2560	70	80	kJ/mol
3		g	1.5002	1.8000	1	3	-
4	secondary nucleation	$k_{bsec,0}$	1.2400e20	1.6800e29	10	1e34	$\mathrm{s^{-1}(m^3)^{-n_{\mu 3}}}$
5		b_{sec}	4.3389	4.8200	1	10	-
6		$n_{\mu 3}$	0.8303	4.9500	0.1	5	-
7	primary nucleation	k_{bprim1}	1.2656e-5	1.1324e-5	1e-11	1e-4	$\mathrm{s^{-1}K^{-1}m^7kg^{-7/3}}$
8		k_{bprim2}	4.6510e-4	2.3926e-3	1e-5	6e-3	-
9		A_{prim}	1.8820e4	8500	10	2e4	$\mathrm{(m^2)^{-n_{\mu 2}}}$
10		$n_{\mu 2}$	1.6805	1.5000	0	2	-

The simulated concentration trends resulting from the optimal parameter values are shown in Figure 5.3 and Figure 5.4 for the six conventional PC and the five coupled PC experiments, respectively.

In the following, we will put an emphasis on the conventional PC processes because of the more complex dynamics and thus the higher amount of information. The duration of the experiments shown in Figure 5.3 was long enough to capture the nucleation event of the counter enantiomer D-Thr (E2) and – were possible – the equilibrium state. In all cases the model solution agrees best with the dynamics of the seeded enantiomer, which is an indication that crystal growth is sufficiently captured by the empirical eqs. (3.18) and (3.19). Growth anomalies such as growth rate dispersion (Ulrich (1989); Srisanga, et al. (2015)) may occur, however, they are probably undetectable by sole concentration measurement. In the model it is therefore assumed that such effects are not pronounced because the seed material consisted of already well defined crystals.

With the exception of PC3, nucleation of the counter enantiomer is predicted with good accuracy as well given the fact that it is a stochastic phenomenon, which is described by a deterministic model (eqs. (3.22) and (3.23)). Apparently, nucleation of the counter enantiomer is quite reproducible under seeded conditions where the seed crystals can act as a heterogeneous surface. In that sense the counter enantiomer seems to appear mainly due to primary heterogeneous rather than homogeneous nucleation. The last two experiments (PC5 and PC6) were included because of their polythermal operation mode and provide a means to further test the temperature dependencies of the kinetic expressions. It appears that the model is also able to predict more dynamic operating conditions. This feature was exploited by Angelov, et al. (2008a) for the calculation of optimal temperature profiles and was pursued in this work as discussed in section 5.4.3.

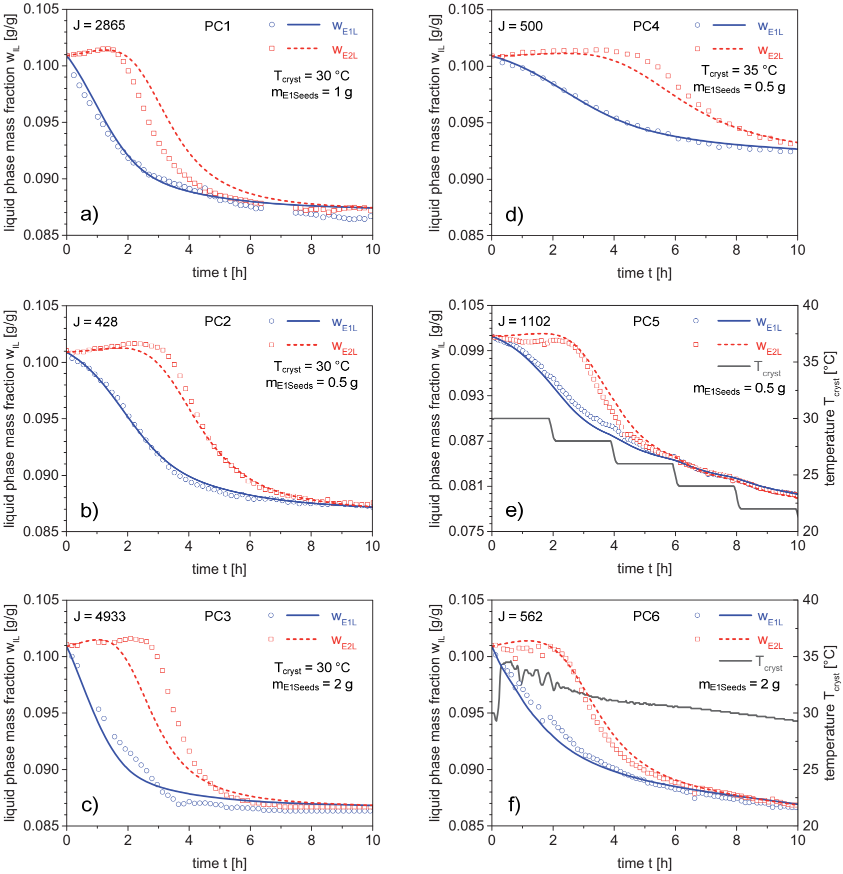

Figure 5.3: Measured (symbols) and simulated (lines) concentration profiles of six PC experiments (Table 5.1) used for the parameter estimation. The value of the objective function J is given for each individual experiment.

Figure 5.4 shows the simulation of the five coupled experiments using the optimal set of parameters for this process concept (Table 5.2, CPC). Due to the symmetry of the process, only the results from Tank 1 are shown, which was seeded with L-Thr. The concentration measurement of the second tank, seeded with D-Thr was, however, included during the estimation procedure, which is the reason why the values of objective function J sometimes appear unusually high although the fit is satisfactory for both crystallizers.

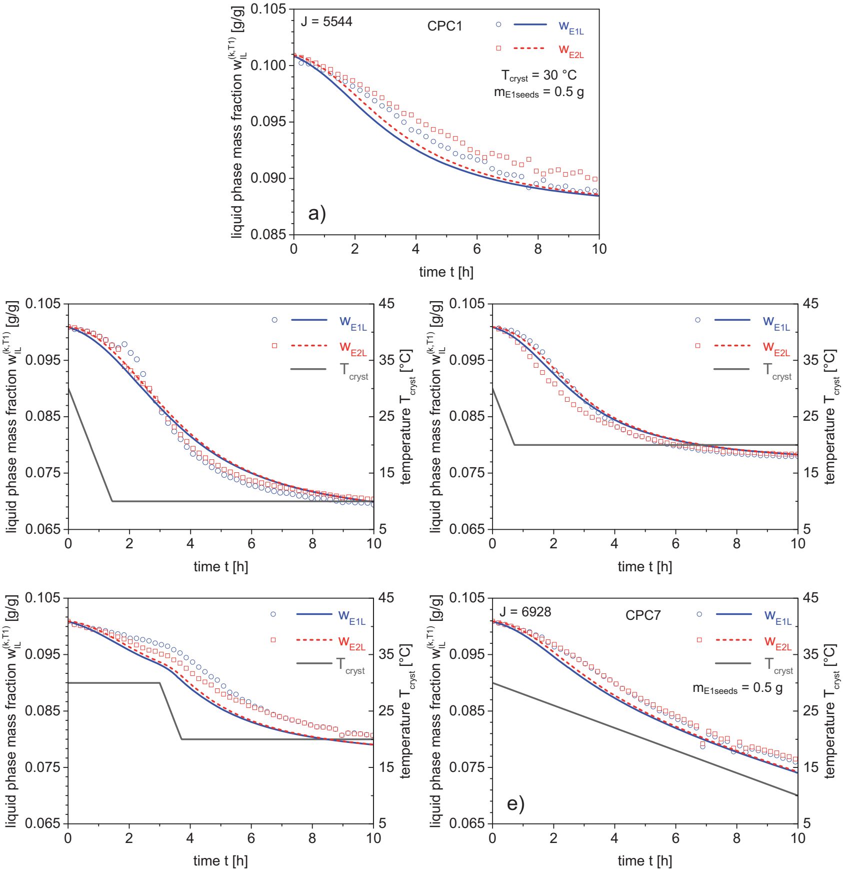

Figure 5.4: Measured (symbols) and simulated (lines) concentration profiles of five coupled preferential crystallization experiments (CPC) used for the parameter estimation. The value of the objective function J resulting from the simulation with the optimal parameters for CPC in Table 5.2 is indicated for each individual experiment.

The agreement between simulation and experiment is very acceptable in particular for the polythermal experiments, CPC4-7. In the coupled case, however, it is particularly important to also consider the predicted final state of the solid phase. It is clear that, at equilibrium, the conventional PC process will yield a solid phase with a purity of approximately 50%. Since CPC drastically reduces the chance of nucleation of the counter enantiomers, it usually shows much higher purities of the respective seeded enantiomers at equilibrium and we need to make sure that the predictions are reasonable. During parameter estimation it was observed that many combinations of parameter values result in local minima of the objective function. Although measured concentration trends were reproduced well, predicted purities were significantly lower and not supported by experimental results. Because of this, it is important to also consider purity predictions.

Table 5.3 summarizes the predicted product masses and purities of all 11 simulated experiments using the respective optimal parameter set for conventional and coupled preferential crystallization (Table 5.2). Since the conventional PC processes almost reached equilibrium after the simulated duration of 10 h, their product purities are close to 50%. As expected, the coupled experiments show higher purities with respect to the seeded enantiomers (L-Thr seeded in Tank1; D-Thr seeded in Tank 2). The predicted purities also follow an intuitive trend in relation to the applied cooling profiles: we expect higher nucleation rates at higher levels of supersaturation, which result from stronger cooling. This becomes evident when we consider the simulation results of the first three CPC processes listed in Table 5.5 in connection with their respective final crystallization temperatures: CPC1 (30 °C), CPC5 (20 °C) and CPC4 (10 °C). As the level of supersaturation increases, purity decreases, which is reasonable. The same holds for the predicted product masses: the simulation of the isothermal case CPC1 yields the lowest, followed by CPC5, whereas CPC4 shows the highest masses due to the strongest cooling. The last two – CPC6 and CPC7 – are located in between the isothermal experiment CPC1 and the polythermal experiment CPC4 regarding product mass and purity.

Table 5.3: Final solid masses m_{IS} and purities Pu_I predicted by simulation of conventional (PC) and coupled preferential crystallization (CPC) after 10 h process duration using the respective optimal parameter set.

Experiment	*product mass, m_{IS} [g]*		*product purity, Pu_I [%]*	
	Tank 1	*Tank 2*	*Tank 1*	*Tank 2*
PC1	15.2	-	52	-
PC2	15.4	-	52	-
PC3	17.3	-	56	-
PC4	9.4	-	54	-
PC5	23.2	-	51	-
PC6	17.1	-	56	-
CPC1	13.6	13.4	96	96
CPC5	22.2	22.3	90	90
CPC4	28.1	28.4	86	86
CPC6	22.6	22.7	95	95
CPC7	26.4	26.5	92	92

We have to keep in mind that two different sets of optimal parameters were used for the simulation of the two process strategies, PC and CPC. When we simulate the six conventional PC experiments with the parameters found optimal for CPC, nucleation of the counter enantiomer is underestimated. On the other hand, when using the values found optimal for conventional PC to simulate the CPC experiments, the final predicted purities do not follow an intuitive trend in relation to the final crystallization temperature. In fact, purities increase with decreasing temperature, which is shown in Table 5.4. This suggests that even though supersaturation is higher at the lower temperatures, the nucleation kinetics become slower. Such a temperature dependency, commonly described by an Arrhenius approach, is in itself reasonable. However, in case of the isothermal experiment CPC1, the very low purity is not supported by the experimental results discussed in chapter 5.2. To clarify, whether the slowing of the kinetics outweighs the higher degree of supersaturation, systematic experiments need to be performed that are specifically designed to investigate nucleation during preferential crystallization.

Table 5.4: Final product masses and purities of three polythermal CPC experiments predicted by the simulation with the kinetic parameters found optimal for conventional PC.

Experiment	*product mass, m_{IS} [g]*		*product purity, Pu_I [%]*		*final temperature, T_{cryst} [°C]*
	Tank 1	Tank 2	Tank 1	Tank 2	
CPC1	13.8	13.7	89	90	30
CPC5	24.5	24.5	93	93	20
CPC4	34.2	34.2	94	94	10

Generally, the estimation of such a high number of parameters is a difficult task. Together with the highly non-linear kinetics, many different combinations of parameter values exist that produce similar simulation results. They have to be analyzed in detail to check for plausibility. Even though the optimizer terminates with a lower objective function value, does not necessarily imply a more reasonable or accurate simulation of the real process.

We have to recognize that the two sets of parameter values found in this work are possibly not optimal. At the same time the underlying model is a simplification, considering only one characteristic dimension of the crystal shape and being based on empirical kinetic expressions. However, it is readily capable of simulating preferential crystallization under different process conditions. Together with the parameter estimates summarized in Table 5.2, it is a suitable working version to simulate all process strategies investigated in this work with good accuracy. In chapter 5.7, we will use it to further analyze the processes to obtain general trends when changing the process conditions.

5.1.2 Simulation of conventional PC

In order to complement the simulation results obtained with the estimated parameter values, we will examine the temporal evolution of the involved kinetic rates, as well as the solid phase. The benchmark experiment PC1 is used for illustrative purposes. Figure 5.5 shows the depletion of supersaturation (a) and the resulting growth (b), primary (c) and secondary nucleation rates (d). As expected, the growth rates of the seeded (E1) and unseeded (E2) enantiomers shown in Figure 5.5b closely follow the dynamics of the driving force depicted in Figure 5.5a. Of more interest are the trends of the primary, B_{Iprim}, (Figure 5.5c) and secondary nucleation rates, B_{Isec} (Figure 5.5d).

The seeded enantiomer shows an almost negligible primary nucleation rate, since its supersaturation is quickly depleted by growth and secondary nucleation. In addition, the heterogeneous contribution captured by eq. (3.23) has almost no effect because the surface area of the unseeded enantiomer E2 is zero at the beginning. Significant amounts of the impurity (E2) are generated after two hours when primary nucleation reaches its highest level.

This is accompanied by a minor increase in primary nucleation of the product species (E1) as a result of the generated heterogeneous surface area.

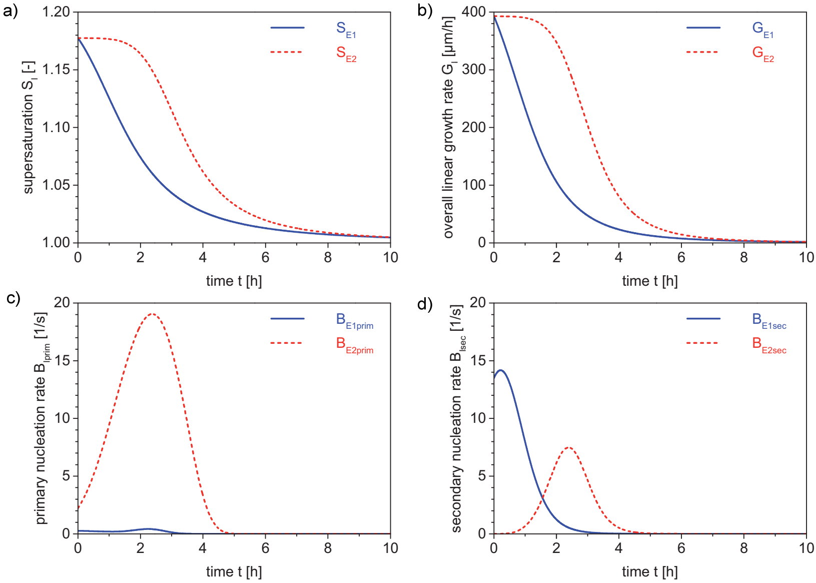

Figure 5.5: Further examination of the simulation of the benchmark experiment PC1. Depicted are the trends of: (a) supersaturation S_I, (b) growth rate G_I, (c) primary nucleation rate B_{Iprim} and (d) secondary nucleation rate B_{Isec} for each enantiomer. I = E1 (seeded), E2 (unseeded).

In order to further understand the course of the primary nucleation rate of enantiomer E2 in Figure 5.5c (red dashed line), consider the graphical representation in Figure 5.6. The surface plot in Figure 5.6a shows the dependence of the primary nucleation rate B_{prim} on supersaturation S and the second moment μ_2 as calculated by eq. (3.23). It can be seen that for lower levels of S (< 1.04), the rate becomes essentially zero.

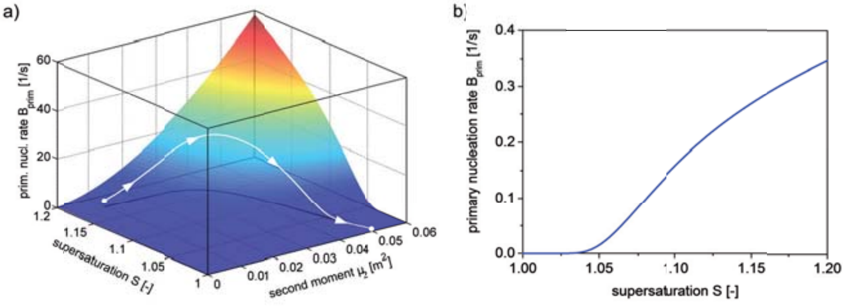

Figure 5.6: a) Calculated primary nucleation kinetics at 30 °C according to eq. (3.23) as a function of supersaturation and the second moment of the opposite enantiomer. The white curve is the trajectory of the unseeded enantiomer from the simulation of experiment PC1. The dark line is its projection into the x-y-plane. b) Calculated primary nucleation rate for $\mu_2 = 0$, which is the contribution of eq. (3.22) alone.

This is the result of eq. (3.22), which is plotted in Figure 5.6b over the same range of supersaturation but for $\mu_2 = 0$. The white line in Figure 5.6a is the trajectory that the primary nucleation rate of the unseeded enantiomer follows in the simulation of experiment PC1. The initial increase is connected to the growing surface area of the seeded enantiomer, which is captured by the heterogeneous contribution in eq. (3.23). The decrease in turn, is the result of eq. (3.22), which eventually becomes zero according to the plot in Figure 5.6b.

Although eqs. (3.22) and (3.23) do not model metastability or, in that sense, an induction time, they still lead to an adequate reproduction of the onset of nucleation of the counter enantiomer E2 (cf. Figure 5.3). Because of the mathematical dependence on supersaturation, the primary nucleation rate already starts at a certain level (Figure 5.5c). In a real metastable solution, however, particles are not immediately generated, thus one can argue that the initial primary nucleation rate predicted by the model should be zero. Up to now, nucleation from solution is, however, still not well understood; hence the physical significance of the chosen mathematical approach is difficult to assess.

A recently postulated single nucleus mechanism (Kadam, et al. (2011)) considers the stochastic appearance of one primary nuclei, which eventually causes a detectable nucleation event due to secondary nucleation. The mathematical description of this approach involves a stochastic model in addition to classical nucleation theory (Kadam, et al. (2012)) and is currently further investigated experimentally in Brandel, et al. (2015). The model presented in chapter 4 could in principle reproduce the proposed mechanism. Once an average induction time t_{ind} is assumed, the parameters of the primary nucleation kinetics (eq. (3.23)) could be adjusted in a way so that exactly one particle exists after this time (Maggioni, et al. (2015)), i.e.,

$$\int_0^{t_{ind}} B_{Iprim}^{(c)}(\tau)d\tau = 1\,. \tag{5.1}$$

The subsequent generation of more particles could then be simulated by adjusting secondary nucleation kinetics (eq. (3.20)) accordingly.

Finally, we will turn to Figure 5.5d and examine the behavior of secondary nucleation (eq. (3.20)) during the simulation of experiment PC1. From a qualitative point of view, the trends shown in Figure 5.5d appear reasonable compared to what is likely to happen in the real process: the secondary nucleation rate of enantiomer E1 is initially high, due to the presence of its seeds and slightly increases, as the third moment of the population grows, before it starts to diminish. At a supersaturation of approximately S = 1.04, it becomes virtually zero because of the non-linear dependence on the driving force. The counter enantiomer E2 is completely dissolved at the beginning of the process, therefore no secondary nucleation can initially occur. It gradually increases only after a significant amount of solid has been formed by primary nucleation. The remaining levels of supersaturation, regarding each enantiomer (E1 after 4 h, E2 after 5 h), are depleted almost solely by crystal growth. This is in line with the common understanding of crystallization, whereby, crystal growth, secondary and primary nucleation occur at increasing levels of supersaturation, respectively.

The discussed kinetics all result in the transfer of molecules from the liquid to the solid phase. For the parameter estimation, however, only the liquid phase was considered, since the observation of the solid phase during the processes is very difficult, especially at the small experimental scale used in this work (cf. section 4.2). Even with a sophisticated technique such as atline video microscopy (Borchert, et al. (2014), Eisenschmidt, et al. (2015)) the challenge in preferential crystallization to distinguish between the crystals of the two enantiomers remains. In the case of the six experiments (PC1-PC6) used for parameter estimation, the final solid phase was not analyzed in terms of its crystal size distribution (CSD), since a necessary separation to obtain homochiral fractions, e.g. by sieving would have at most allowed to characterize the population that originated from the seeds. Considering the duration of 10 h, it is, however, very likely that the nucleated counter enantiomer was also able to grow to similar mean sizes, thus causing a significant overlap of both CSDs.

At this point, the theoretical analysis of benchmark experiment PC1 shall be concluded with the predicted evolutions of the CSDs shown in Figure 5.7. The seeded enantiomer (a) shows a bimodal distribution consisting of the grown seed population and a large amount of smaller particles generated mostly by secondary nucleation (compare Figure 5.5d). The final mean crystal sizes of these two populations are approximately 460 µm and 1100 µm, yielding a total mass of m_{E1S} = 8.4 g after 10 h. No significant amount of the unseeded enantiomer is generated until 1 h (m_{E2S} < 0.03 g). Compared to the seeded enantiomer, the final CSD of the impurity (Figure 5.7b) is very wide and has a mean crystal size of approximately 440 µm, while the number of particles is more than twice as large. The total mass of the unseeded enantiomer, m_{E2S}, at the end of the process is 7.4 g – a difference of 1 g owing to the seeds. It is obvious that both final distributions overlap significantly leading to the aforementioned challenges concerning their experimental determination.

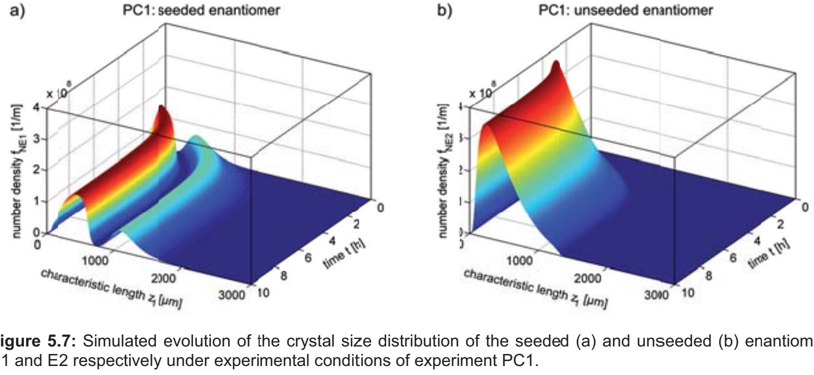

Figure 5.7: Simulated evolution of the crystal size distribution of the seeded (a) and unseeded (b) enantiomers E1 and E2 respectively under experimental conditions of experiment PC1.

In summary, the mathematical description presented in chapter 3.1 together with the two optimized sets of parameters listed in Table 5.2, can simulate conventional and coupled PC under different process conditions with quite good accuracy concerning the liquid phase. Naturally, it is possible that an even better set of parameter values exists. The optimization was therefore repeated using two different starting points at ± 5% of the optimal points as well as two randomly chosen points far from the respective optimum. In all three cases it was not possible to obtain a lower value of the objective function J. Of course this is no proof and a more detailed analysis including statistical methods as was done by Czapla, et al. (2009a) is required. Such analysis was omitted as it goes beyond the scope of this work. For a more detailed account on this matter the reader is referred to the dissertation of Czapla (2010).

The next chapters are primarily devoted to the discussion of experimental results. However, these will be frequently used to challenge some of the predictions made by the model with the parameters found in this chapter, especially with respect to the solid phase.

5.2 Conventional batch preferential crystallization

The following experiments were done in a single batch crystallizer under different process conditions and are intended to serve the following purposes:

- investigate preferential crystallization in its simplest implementation
- obtain a starting point for successive process improvements
- use observed process dynamics for model calibration

Some of the experiments were already considered in the previous chapter for parameter estimation. In the following, they will be discussed in more detail and compared to other process strategies.

5.2.1 Isothermal benchmark experiment

The following three experiments were done according to the general experimental procedure described in chapter 4.6 and Table 5.3 therein. They consist of the previously discussed benchmark experiment PC1 and two repetitions (PC1a, PC1b). L-threonine (E1) was the preferred enantiomer in all subsequent experiments. In order to determine the approximate induction time for nucleation of the unseeded enantiomer (E2) under these conditions, the first experiment was allowed to approach thermodynamic equilibrium. According to the concentration signal shown in Figure 5.8a, nucleation occurred after approximately 1.2 h. The repetition experiments PC1a,b were therefore stopped after this period of time to collect and filtrate the suspension for characterization of the obtained crystals as described in chapter 4.6.

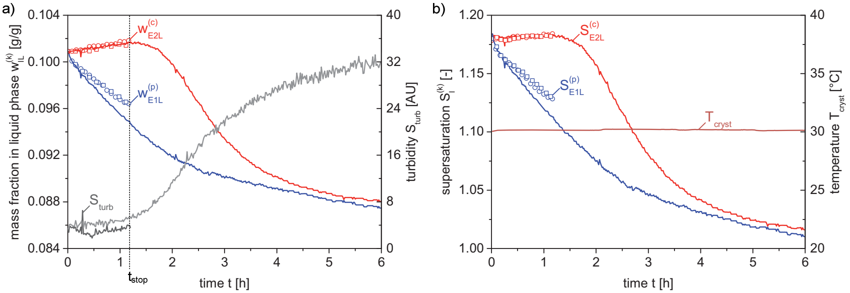

Figure 5.8: Twofold repetition of the benchmark experiment PC1 (solid lines) with an interruption for product capture after 1.2 h (circles: PC1a, squares: PC1b). a) Liquid phase mass fraction and turbidity signal. b) Supersaturation and temperature.

In addition to the concentration measurement, a turbidity probe was used for testing purposes to assess its potential in detecting the nucleation event. The signal, S_{turb}, did not appear to be more sensitive than the concentration measurement, since no significant increase in turbidity could be seen before nucleation was detected by the other analytical devices. For this reason it was not used in other experiments, which was also due to the limited amount of ports in the lids of the crystallizers.

The repetitions of experiment PC1, indicated by symbols in Figure 5.8, show good reproducibility. This is further confirmed by the analysis of the solid phase obtained after the process duration of 1.2 h. Figure 5.9a shows the number-based CSD of the L-threonine seeds and the products determined by manual measurement (see chapter 4.5). During each of the two experiments, the seeds have grown to almost the same mean size regarding the characteristic length z_1. A log-normal distribution was assumed to describe the histograms and used to approximate mean size μ and standard deviation σ. Based on this, an average increase of the mean length by 575 µm was determined, which can also be seen by comparing the micrographs of the seed and product crystals depicted in Figure 5.9b and c, respectively.

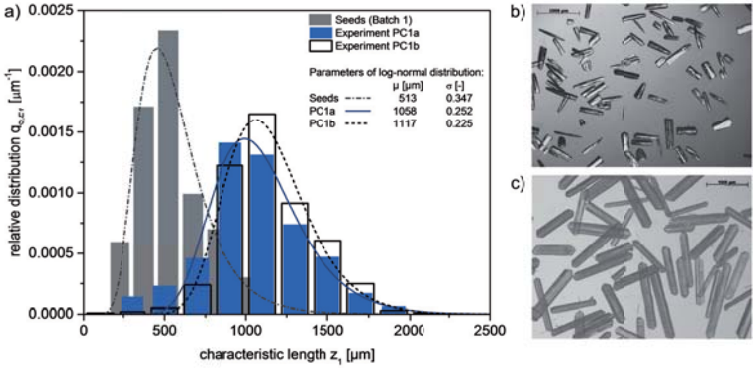

Figure 5.9: a) Seed and product crystal size distributions of experiments PC1a and PC1b after 1.2 h process duration. Lines represent fitted log-normal distributions. b) Micrograph of the L-threonine seeds and (c) the product obtained from PC1b, respectively. The bars have a span of 1000 µm.

The resulting product masses, m_{E1S}, purities, Pu_{E1} and mean crystal sizes, $\bar{z}_{E1}$, with respect to the seeded enantiomer L-Thr (E1), are summarized in Table 5.5 along with predicted values from the simulation. The values of experiment PC1 were obtained after 17.5 h, when the suspension had presumably reached equilibrium. Based on the solubility correlation given by eq. (4.1), a maximum of 15.6 g of racemate (in addition to the seeds) can crystallize under the process conditions of PC1. The difference of 2.2 g can be attributed mainly to losses during reactor emptying, filtration and washing of the crystals. Additionally, it is possible that equilibrium was not entirely reached. According to the simulation this takes approximately 28 h. When considering the product loss, the simulation is quite accurate regarding the predicted mass and purity of the solid phase. This is also the case for the subsequent experiments PC1a and b, which show the actual potential of the conventional PC process under these conditions. In both cases the product, obtained after 1.2 h, has a very high purity (> 99%), however, the absolute yield is rather low. According to the solubility (eq. 5.1), a maximum amount of approximately 7.8 g of L-Thr can be crystallized at the given temperature of 30 °C in addition to the seed mass. The relative yield (eq. 4.11) thus is 31% with respect to the thermodynamic limit. The mean crystal size is underestimated by an average of 220 µm by the simulation compared to experiments PC1a,b, which is caused by stronger secondary nucleation in the simulation than in the experiment.

In addition to the product masses that were determined gravimetrically, estimates based on the concentration measurement are indicated in brackets. They provide additional information about the amount, which is lost due to the processing of the suspension, next to the model predictions. In case of PC1a,b up to 15% of the expected absolute yield are lost.

Table 5.5: Comparison of product mass, purity and mean crystal size of experiments PC1, PC1a, PC1b and the corresponding model predictions. Values in brackets were determined based on the concentration measurement.

Exp. No.	*Product mass* $m_{E1S}^{(p)}$ *[g]*	*Purity* Pu_{E1} *[%]*	*mean crystal size* $\bar{z}_{E1}$ *[µm]*
PC1	14.38 (16.65)	53.3	-
model prediction	16.05	53.1	1100
PC1a	2.77 (3.15)	99.5	1058
PC1b	2.72 (3.31)	99.6	1117
model prediction	3.76	98.4	867

The experiments discussed in this section confirm the general applicability of preferential crystallization to resolve the racemic mixture of a conglomerate forming system. It was also shown that batch-to-batch reproducibility is given to a certain extent once the onset of nucleation is known. Still, the stochastic nature of this event strongly influences the robustness of the process since even minor fluctuations in the conditions can shift the induction time.

In terms of yield enhancements it is mandatory to either increase the period of time it takes for the unseeded enantiomer to nucleate, or to accelerate crystallization of the target enantiomer. The latter can, for example, be achieved by providing a larger surface area, e.g. by using milled or larger amounts of seeds. Polythermal operation is another option; however, one has to remember that both enantiomers are affected by the increase in driving force during further cooling. Conventional PC is therefore not well suited for such kind of strategy.

In the following sections we will investigate process strategies that address the challenges posed by nucleation of the impurity. They either aim at prolonging or completely suppressing its appearance in the solid phase. The first option uses fines dissolution to remove small particles.

5.2.2 Effect of fines dissolution on conventional PC

Dissolving smaller particles during a crystallization process is beneficial for the final CSD in particular when large crystals are desired. In preferential crystallization it has the additional effect that fines dissolution also removes nuclei of the unwanted enantiomer. It should therefore be possible to prolong the period during which only the seeded species can crystallize. That this is indeed the case is shown in this section. Experimental results of conventional PC with fines dissolution (FD) are compared with the previously discussed experiments PC1 and PC1a. As before, one experiment (PC-FD1) was carried out to assess the onset of nucleation and repeated afterwards to analyze the product (PC-FD1a) before this event. The process conditions differ slightly compared to the standard ones in Table 4.3; differences are given in the following table. The total mass of the initial solution was increased to 490 g to compensate for the dead volume of the fines dissolution unit (FDU), however, the concentration and initial saturation temperature were identical.

Table 5.6: Initial solution composition for conventional PC with fines dissolution (experiments PC-FD1 and PC-FD1a).

description	*process parameter*	*value*
mass of solvent	m_{H2O}	391.12 g
mass of L-Thr	m_{E1}	49.441 g
mass of D-Thr	m_{E2}	49.441 g
saturation temperature	T_{sat}	43.7 °C (eq. (5.1))
mass of seeds	$m_{E1seeds}$	1 g (Batch 3)

In the left graph of Figure 5.10, the mass fractions of conventional PC with and without fines removal are compared. Solid lines and symbols represent experiment PC-FD1 and its repetition PC-FD1a, respectively. The previous experiment PC1a represented by grey squares had to be stopped after 1.2 h (t_{stop}), while the use of fines dissolution increased the time until filtration by 48 min ($t_{stop}^{(FD)}$).

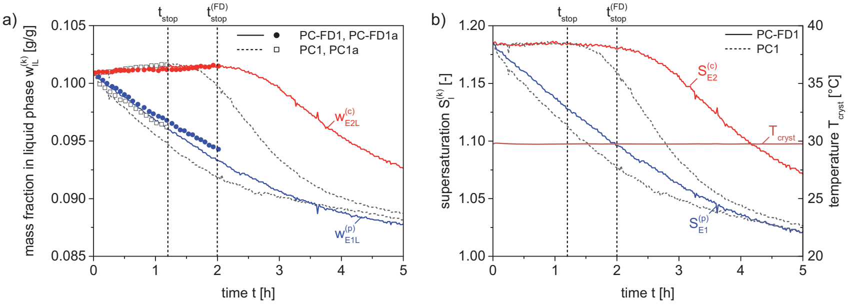

Figure 5.10: a) Mass fractions in the liquid phase during preferential crystallization with fines dissolution (red and blue circles and solid lines) and without fines dissolution (grey squares and dashed lines). b) Corresponding supersaturation profiles with fines dissolution (solid lines) and without (dashed lines) as well as temperature.

During this extended period of undisturbed crystallization of enantiomer E1 a further depletion of its supersaturation occurs, which is shown in Figure 5.10b. Consequently, a higher amount of mass can crystallize, which, at the same time, results in larger crystals as shown in Figure 5.11. Compared to the conventional process with no removal of small particles, an increase of the mean characteristic length of approximately 440 µm was measured.

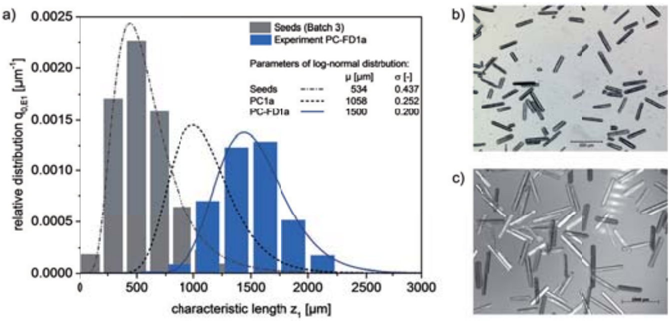

Figure 5.11: Comparison of the crystal size distributions (a) at t_{stop} without (b) and with fines dissolution (c).

At the same time, the absolute yield of experiment PC-FD1a was 0.8 g higher in comparison to PC1a,b, which is equivalent to a relative yield of 37% with respect to the solubility at 30 °C. Thermodynamics allow a maximum of 8.5 g of pure L-Thr to crystallize under these conditions in addition to the mass of seeds. The product masses of PC-FD1 given in Table 5.7, suggest a quite significant loss of solid material considering the values of the concentration measurement, the model prediction and the maximum thermodynamically possible yield of 18 g (including seeds) at the eutectic point.

Table 5.7: Comparison of product mass, purity and mean crystal size of experiments PC-FD1, PC-FD1a and the corresponding model predictions. Values in brackets were determined based on the concentration measurement.

Exp. No.	*Product mass* $m_{E1S}^{(p)}$ *[g]*	*Purity* Pu_{E1} *[%]*	*mean crystal size* $\overline{z}_{E1}$ *[μm]*
PC-FD1	13.97 (18.2)	59.5	-
model prediction	17.7	52.9	1580
PC-FD1a	3.54 (4.67)	98.9	1500
model prediction	4.9	99.9	1100

This is primarily caused by crystals adhering to the fines dissolution filter depicted in chapter 4.8. Over the entire length of the experiment of 14.5 h the built-up of solids on the filter can hardly be prevented. This is an issue that could be drastically improved by using a settling zone rather than a filter in order to withdraw a certain fraction of the crystal population. Owing to the confined space inside the crystallizer vessel such an approach was, however, not possible in this work. For shorter operating times that are relevant for the actual separation, i.e. during PC-FD1a, blocking of the filter was not significant since it mainly occurs during the nucleation event where large amounts of particles are generated at a high rate.

The previous two experiments were performed with the FDU described in chapter 4.8. It is referred to as design 1 in Table 5.8. In order to improve the dissolution efficiency, a second design was used that provided a higher residence time of the suspension inside the FDU by doubling the inner diameter. At the same time the total length was reduced to keep the dead volume low.

Table 5.8: Dimensions of the fines dissolution units (FDU) and the corresponding mean residence times at a flow rate of 50 ml/min. Design 1 was used for experiment PC-FD1, design 2 for experiment PC-FD2.

Design	L_{heat} *[m]*	L_{cool} *[m]*	*d [mm]*	$\tau_{heat}[s]$	$\tau_{cool}[s]$
1	2.16	3	3.2	26	36
2	1	2	6.4	42	85

The first experiment (PC-FD2) using the second design of the FDU is compared with experiment PC2. Both had the same operating conditions except for the total mass of the initial solution to account for the dead volume of the FDU. In contrast to experiments PC1 and PC-FD1, 0.5 g of seeds were used. Figure 5.12a shows the concentration profiles of three experiments. The previous experiment PC2 (circles) was repeated (PC2a, dashed lines) since a problem with the analytics was presumed during PC-FD2*. Based on the trends of experiments PC2 and PC2a in Figure 5.12a, the process should be stopped after approximately 2 h in order to obtain pure L-threonine crystals. The longer induction time compared to experiment PC1 (cf. Figure 5.8) could result from the lower (heterogeneous) surface area due to the reduced seed mass. A strong prolongation of the separation phase was achieved in experiment PC-FD2. Judging from the concentration signal in Figure 5.12a it can be maintained for at least 5 h without significant nucleation of the counter enantiomer.

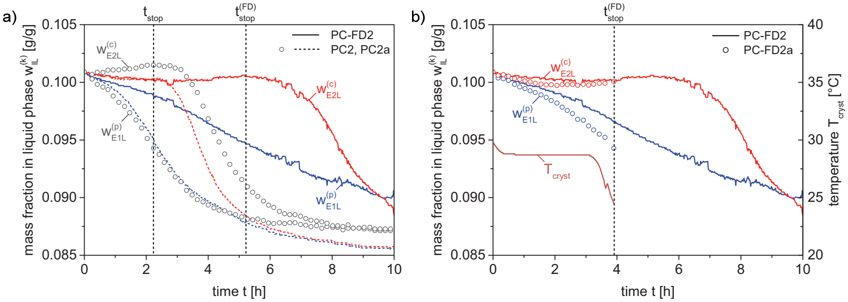

Figure 5.12: a) Mass fractions of enantiomers E1 and E2 when the second design of the FDU is used (solid lines) in comparison to two conventional PC processes under identical operating conditions without fines dissolution (symbols, dashed lines). b) Repetition of experiment PC-FD2 under slightly polythermal conditions and filtration after 3.9 h.

Within this period of time the concentration of the seeded enantiomer E1 drops to roughly the same value, $w_{E1L}^{(p)}(t_{stop}^{(FD)}) = 0.095$, as in the experiment without fines dissolution (PC2). As opposed to experiment PC-FD1 no yield improvement compared to the standard process without fines dissolution was achieved. This is a strong indication that the longer residence time of the suspension inside the FDU leads to a more effective dissolution, which is to be expected. As a result, the withdrawn seed fractions are dissolved to a higher extent as well, which explains the reduced yield.

---

* It can be seen in Figure 5.12a that the concentration of the counter enantiomer E2 does not follow the usual upward trend before it nucleates. This is likely due to a temperature drift in the polarimeter cell caused by an insufficient flow of the thermostat medium. The same behavior occurred during the repetition of experiment PC2. Since both experiments (PC2 and PC2a) were performed under identical conditions, it can be conjectured that the real trend of the concentrations is reflected by experiment PC2.

The subsequent repetition, PC-FD2a, in Figure 5.12b additionally made use of a polythermal temperature profile. Since design 2 of the FDU was found to delay nucleation more efficiently it was assumed that further careful cooling during the separation would be possible without promoting immediate crystallization of the counter enantiomer. The involved temperature trajectory was calculated using an optimization routine by Angelov, et al. (2008a). It was part of a preliminary optimization study presented in Eicke, et al. (2010).

Experiment PC-FD2a was stopped after 3.9 h, leaving a safety margin of approximately 1 h. Table 5.9 summarizes the solid phase analyses of all four experiments of this series, the first two (PC2, PC2a) being standard PC processes without fines dissolution. Compared to PC-FD1a, the product obtained from PC-FD2a has a higher purity and a significantly higher mean crystal size. This is due to the more efficient dissolution using the second design of the FDU, however, a reduction in productivity under the chosen process conditions has to be accepted since the process time was longer and slightly less product mass was obtained.

Table 5.9: Comparison of product mass, purity and mean crystal size obtained from experiments PC-FD2 and PC-FD2a using the second design of the FDU with conventional experiments PC2 and PC2a. Values in brackets were calculated based on the concentration measurement.

experiment	*Product mass* $m_{E1S}^{(p)}$ *[g]*	*Purity* Pu_{E1} *[%]*	*mean crystal size* $\overline{z}_{E1}$ *[μm]*
PC2	14.06 (15.71)	51.7	-
PC2a	14.30 (17.52)	to be measured	-
PC-FD2	11.65 (15.61)	59.5	-
PC-FD2a	3.43 (3.88)	99.2	2500

It has to be kept in mind that the experiments PC-FD1a and PC-FD2a cannot directly be compared because of the different masses of seeds and the polythermal operation applied during the latter process. Naturally, the yield obtained from the second experiment would have been even lower under isothermal conditions. The use of a higher mass of seeds could, however, counteract this reduction. The question that remains is if the further prolongation of the nucleation event during PC-FD2 in comparison to PC-FD1 is primarily due to the more efficient fines dissolution or because of the lower amount of seeds. When we again look at experiments PC1 and PC2 (1 g and 0.5 g of seeds, respectively) in Figure 5.3, we could conclude that the total surface area of the seeds has an influence on the induction time of the unseeded enantiomer. However, experiment PC3, in which 2 g of seeds were used, does not support this conclusion. In this experiment the onset of nucleation occurred at almost the same time as in PC2 with 0.5 g of seeds. Apparently, this contradicts the assumption of proportionality between seed surface area and heterogeneous nucleation of the counter enantiomer. Still, the observation does not entirely disprove the assumption but shows that a certain randomness concerning the detected onset of nucleation remains. More repetitions of these experiments would be necessary to confirm whether there is a significant relation or not. A study by Ito, et al. (2008) suggests that D-Thr can nucleate on certain faces of L-Thr crystals, which would again support the idea stated above. Their experiments, however, were performed in non-agitated solutions and the question can be raised, whether their observations apply to a stirred suspension.

Despite the experimental uncertainties, we saw that fines dissolution can effectively suppress nucleation. The investigations discussed in this chapter present a first implementation of this process strategy and were partly taken from the works published in Eicke, et al. (2009a) and Eicke, et al. (2009b). Although the experiments were not optimized in terms of productivity, the ability to prolong the period until nucleation occurs is a strong improvement of preferential crystallization. Given this extended process region of safe operation it is possible to implement means to increase productivity more easily. Especially further subcooling, which is the most obvious lever in crystallization processes, can be used, which was also demonstrated in experiment PC-FD2a. Under conventional conditions, that is without fines dissolution, a further increase of supersaturation by cooling has a high probability of inducing early unwanted nucleation. In that way, this first alternative strategy leads to a more robust separation process.

5.2.3 Summary of conventional PC experiments

In order to summarize the results of conventional preferential crystallization, a graphical comparison is given in Figure 5.13. The left figure shows productivity calculated with eq. (4.13) versus the *increase* of solid mass, $\Delta m_{E1S} = m_{E1S}(t_{stop}) - m_{E1seeds}$. As stated before, the use of fines dissolution leads to a reduction of the productivity since also parts of the seed material are constantly dissolved. At the same time the mean crystal size increases as shown in Figure 5.13b.

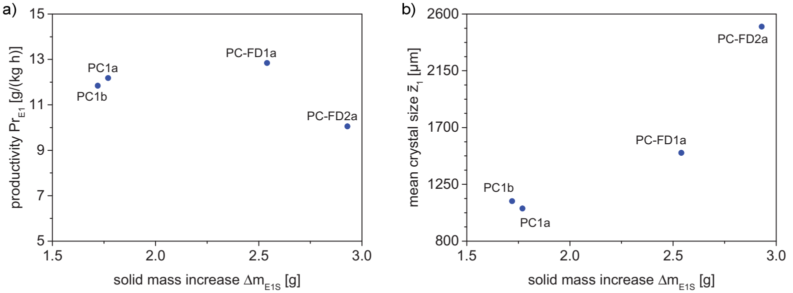

Figure 5.13: Summary of conventional PC experiments including the application of fines dissolution. All experiments were done at a crystallization temperature of 30 °C. Product purity was at least 99% in all cases. a) Productivity versus the increase in solid mass. b) Mean crystal size versus the increase in solid mass.

Here we can also again see the positive effect of the improved fines dissolution unit (PC-FD2a) on the mean crystal size, which could be further increased, compared to the first design with lower residence time (PC-FD1a). So far we have been able to delay nucleation. In the following chapter we will now turn to a process concept that has the aim of entirely resolving the problem of nucleation of the counter enantiomer.

5.3 Coupled batch preferential crystallization

The idea of crystallizing each enantiomer in a separate confinement is a logical step in case of a conglomerate forming system and was introduced in chapter 2.4 as well as in chapter 4.7. The following experiments are a continuation of the experimental studies initiated by Ziomek (2011) with a stronger focus on polythermal operation and the incorporation of the mathematical model to control and optimize this process variant of preferential crystallization. The first experiment presented in this chapter is essentially a repetition of Ziomek's initial investigation on isothermal coupled PC, however, under slightly different conditions.

5.3.1 Isothermal benchmark experiment

Analogous to the conventional PC process, we first examine an isothermal benchmark experiment, which can be compared to the isothermal experiments PC1, PC1a,b and PC2 because initial solution composition and crystallization temperature were the same. The process conditions for the first coupled PC experiment, denoted as CPC1, are summarized in Tables 4.3 and 4.4. Each crystallizer was seeded with 0.5 g of crystals taken from Batch 3 (cf. Table 4.2), i.e. Tank1 received seeds of L-Thr (E1) and Tank 2 seeds of D-Thr (E2).

The concentration measurement of each crystallizer is shown in Figure 5.14a,b for both enantiomers, respectively. In both tanks, the composition of the solution remains nearly racemic throughout the entire process and approaches the equilibrium concentration at 30 °C indicated by the dashed lines.

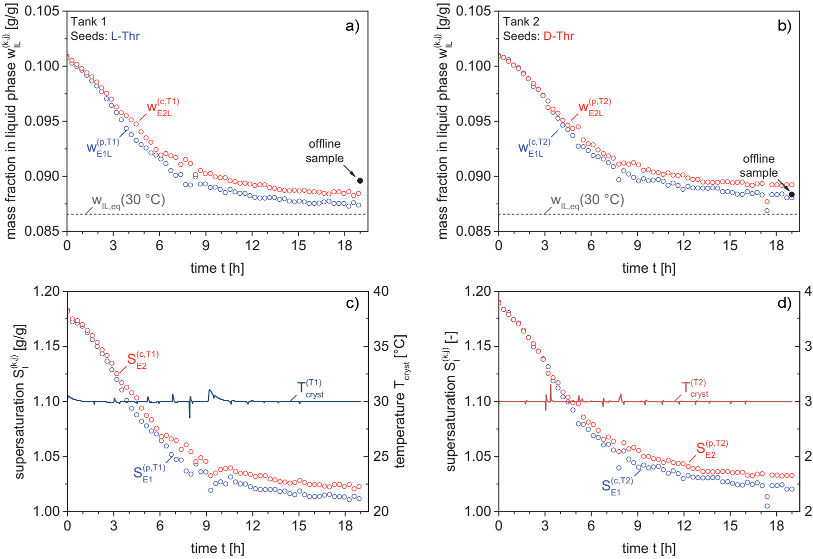

Figure 5.14: a,b) Liquid phase concentration of enantiomers E1 and E2 in each crystallizer (T1, T2) and the corresponding supersaturation trends (c,d) during the isothermal benchmark experiment CPC1. Tank 1 was seeded with 0.5 g of L-Thr, Tank 2 with 0.5 g of D-Thr.

This is an expected observation and indicates that the chosen exchange rate of 50 ml/min is sufficiently high to prevent mass transfer limitations from one crystallizer to the other. In contrast, if - over the course of individual experiments - the exchange rate were successively lowered, the concentration profiles in each crystallizer would diverge and approach that of the conventional PC process; with no exchange the process naturally resembles two conventional batch processes. The maximum benefit of the coupled setup would occur at an infinitely high exchange rate, which would result in an ideally mixed solution spread across two crystallizers with spatially separated solid phases. In addition, absolute process symmetry requires that the seeded enantiomers crystallize at identical rates. Only in that case will this process concept perfectly mimic a racemization in the liquid phase. A real *in situ* racemization is mediated by a racemizing agent, e.g. an enzyme (Wurges, et al. (2009)). Other options are reviewed, e.g. in Ebbers, et al. (1997) and Yoshioka (2007). As we will see in section 5.4, complete symmetry is, however, not necessary for a successful separation using coupled preferential crystallization.

The two graphs at the bottom of Figure 5.14 show the corresponding supersaturation trajectories next to the temperatures in each crystallizer. According to these information solid-liquid equilibrium was not entirely reached after 19 h, which was also confirmed by gravimetric offline analysis of the final solutions (solid circles in Figure 5.14a,b). The small peaks in the temperature signals resulted from the frequent replacement of the exchange filters. An undetected filter blockage in Tank 1 caused the sharp temperature increase after 9 h. Since an online observation of the solid phase composition was not available, the quality of the separation could only be assessed an analysis of the final products. The liquid phase analysis during the process is ambiguous since the concentration decrease of, e.g. enantiomer E2 in Tank 1 could in principle also result from its nucleation in that vessel.

The histograms in Figure 5.15 show the CSDs of the products obtained at the end of the process. In both cases the distribution is very wide indicating a significant amount of nucleation. Based on the rather high product purities given in Table 5.10 the populations below the size of 1500 µm most likely stem from secondary nucleation of the seeded enantiomers. Strong nucleation of the respective counter enantiomers in each crystallizer would have resulted in an abundance of small particles as well, however, product purity would have been lower. Assuming the population below size 1500 µm in Tank 1 (Figure 5.15a) hypothetically consisted of at least 50% D-Thr, product purity would be approximately 96%, which is significantly lower than the measured value in Table 5.10.

The seed population in Tank 1 (L-Thr) represented by the second peak of the roughly bimodal product distribution, has grown to a mean size of approximately 2800 µm. Compared to the conventional batch experiments PC1a,b this is an almost threefold increase. A similar value can be assigned to the product of Tank 2 (D-Thr). It is not surprising that secondary nucleation is very pronounced given the length of the process. Over the period of 19 h the crystals were subjected to mechanical stress, which in case of PC1a,b only lasted for the duration of 1.2 h. The product masses show a significant increase in relative yield (eq.(4.11)) compared to the conventional process. Based on solubility (eq.(4.1)) a maximum of 15.6 g of pure enantiomer can crystallize in each vessel at 30 °C under the chosen conditions.

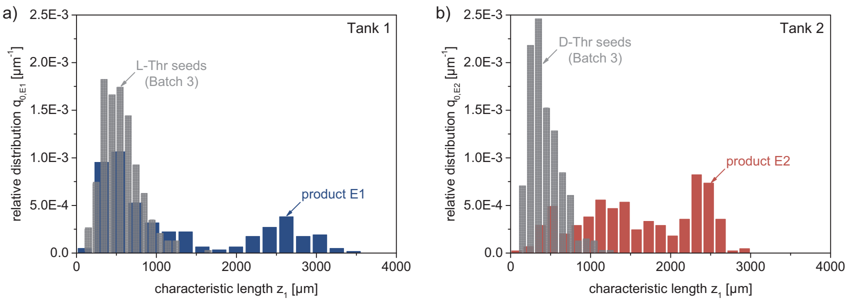

Figure 5.15: Crystal size distributions of the L- and D-Thr seeds (Batch 3) and the final products obtained from Tank 1 (a) and Tank 2 (b) at the end of experiment CPC1.

Comparing the mass of L-Thr obtained from Tank 1 with experiments PC1a,b the relative yield was increased from 31% to 71% of the thermodynamic limit. The product masses in brackets (Table 5.10) are again estimates based on the concentration signals and indicate that not all product was recovered. During coupled experiments solid material is additionally lost due to the replacement of the exchange filters.

Table 5.10: Results of the product analysis from experiment CPC1. T_{cryst} = 30 °C, m_{seeds} = 0.5 g, t_{stop} = 19 h. Values in brackets are estimates based on the concentration signals (eq. (4.10)).

Crystallizer	*Product mass* $m_{IS}^{(p)}$ *[g]*	*Purity* Pu_I *[%]*	*Productivity* Pr_I *[g/(kg h)]*	*Mean crystal size* $\overline{z}_{E1}$ *[µm]*
Tank 1 (L-Thr)	11.4 (15.0)	98.3	11.4	≈ 2800 (seed peak)
Tank 2 (D-Thr)	10.7 (13.4)	98.2	10.7	≈ 2500 (seed peak)

This first coupled experiment already shows that under the same conditions regarding temperature and initial supersaturation, the conventional process is significantly outperformed in terms of product mass and relative yield. Because of the long duration of 19 h productivity is low. According to the liquid phase analysis in Figure 5.14, the major part crystallizes within the first 10 h under these isothermal conditions. A repetition of CPC1, stopped after 11 h, yielded 11.15 g of L-Thr and 10.57 g of D-Thr, both with a purity of 97.7%. This is an insignificantly smaller amount of product and resulted in an average productivity of 17.6 g/(kg h). Subsequent runs were therefore stopped after ten or eleven hours.

It can further be seen that the product purities obtained from CPC1 and its repetition are slightly lower compared to the conventional batch summarized in Table 5.5. The solutions were initially supercooled by approximately 14 K ($T_{sat} \approx 44$ °C), which is already close to the border of metastability for cooling rates of -14 K/h (see also Polenske (2003)). Naturally, this does not work in favor of the separation by preferential crystallization. In this work a purity of 98% was chosen as the minimum requirement for a successful separation. Even though the conditions were at the border of metastability, the coupled process was able to produce product with this specification. For higher purities it can safely be assumed that a slight reduction of the initial supersaturation is sufficient. In order to be able to compare subsequent experiments with the benchmark experiments the initial conditions were not changed.

5.3.2 Comparison of coupled and conventional benchmark experiments

To conclude the coupled benchmark experiment CPC1 we will compare it with the conventional experiment PC2 in terms of productivity. Figure 5.16 shows the temporal evolution of the mass of preferred enantiomer E1 (a) and the corresponding productivity (b). Only the results from tank 1 are shown for the coupled case, which was seeded with L-Thr. The trends were calculated, based on the atline concentration measurements using eqs. (4.9), (4.10) and (4.13). The indicated time t_{stop} (2.3 h) marks the point up to which the conventional process (dashed line) produces pure enantiomer. The coupled process (symbols), on the other hand, is not limited to such time. It can reach thermodynamic equilibrium without significant nucleation of the counter enantiomer. Because of this, it is possible to exceed the productivity of the conventional batch.

If space-time yield is the crucial performance criterion, the coupled process should be stopped after 5 h were it reaches maximum productivity. Under the chosen conditions, it is obvious from Figure 5.16b that the conventional batch will always operate below its maximum capacity.

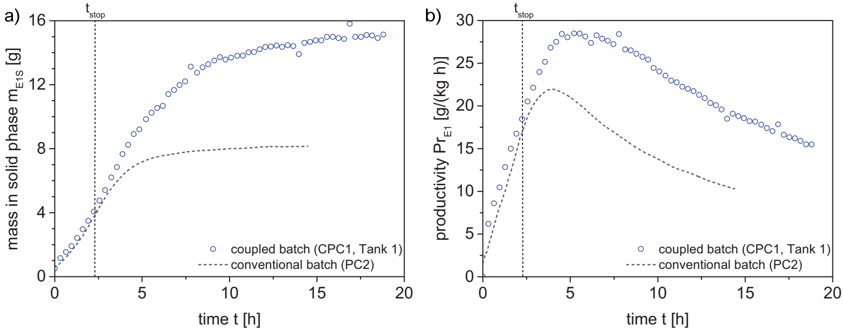

Figure 5.16: Comparison of coupled and conventional PC experiments CPC1 (Tank 1) and PC2 regarding solid mass of preferred enantiomer E1 (a) and productivity (b) calculated with eqs. (4.9), (4.10) and (4.13), respectively. After t_{stop} conventional preferential crystallization does not produce pure enantiomer anymore.

Regarding purity we could see that, under the chosen operating conditions, the coupled process does not entirely prevent nucleation of the respective impurity. However, unlike conventional PC, the process was not stopped after the induction time. The product purity achieved with conventional PC strongly depends on the duration of the process, which is not the case for coupled PC. Therefore, it is only a matter of choosing favorable initial conditions if purities > 98% have to be achieved. In the following section the use of fines dissolution in connection with coupled PC is investigated.

5.3.3 Effect of fines dissolution on coupled PC

In the previous chapter we reconfirmed the general conclusion that by coupling two crystallizers via the liquid phase, the separation task becomes more robust compared to the conventional case. This section proceeds in analogy to chapter 5.2.2 and demonstrates the impact of fines dissolution on coupled PC. For the following experiment CPC-FD1 the first design of the FDU was used whose dimensions are given in Table 5.8. It was operated according to the conditions summarized in Table 4.5.

The results of the concentration measurement from CPC-FD1 are shown in Figure 5.17a,b. Additionally the trajectories of the preferred enantiomers from experiment CPC1 are included for a direct comparison (dashed curves). It can be seen that crystallization proceeds at a slightly slower rate when fines dissolution is used, which was already observed during conventional PC. Towards the end of the process the concentration remains at a slightly higher level compared to CPC1 as a result of the continuing dissolution of small particles.

The corresponding trajectories of the supersaturation are depicted in Figure 5.17c,d. Compared to experiment CPC1, the driving force does not decrease as fast because of the dissolution of smaller particles.

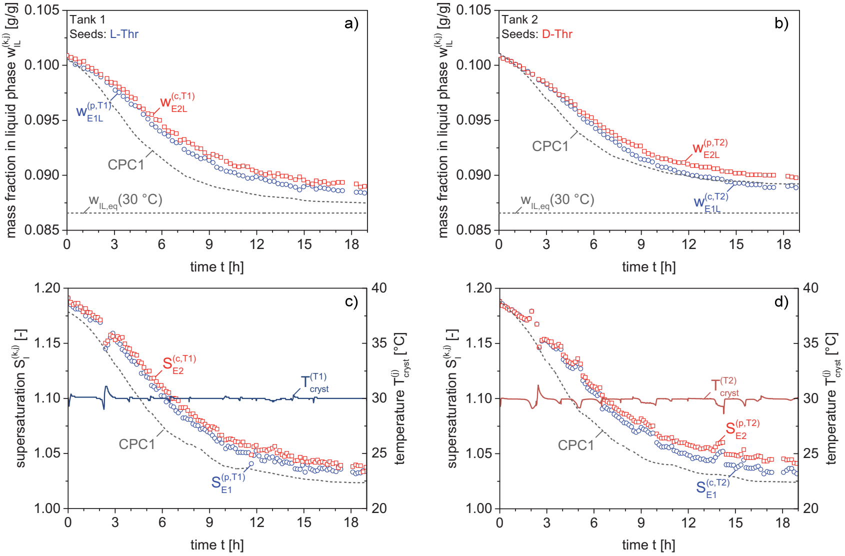

Figure 5.17: a,b) Liquid phase concentration of enantiomers E1 and E2 in each crystallizer (T1, T2) and the corresponding supersaturation trends (c,d) during the isothermal experiment CPC-FD1. Tank 1 was seeded with 0.5 g of L-Thr, Tank 2 with 0.5 g of D-Thr. The dashed lines show the trends from the previous experiment CPC1.

Therefore more material is available for the growing seeds, which is reflected by the final CSDs in Figure 5.18. Both peaks that can be associated with the seeds are approximately 500 μm larger in terms of the characteristic length z_1 compared to the product from CPC1. At the same time, fewer particles are found below the size of 1000 μm, which is an additional indication that the removal and dissolution of fines was effective. The different positions of the product peaks that emerged from the respective seed crystals are likely due to the properties of the initial populations, which were not identical in terms of mean size and width of the distributions. The slightly larger L-Thr seeds eventually grew to larger sizes than the D-Thr seeds as the masses were identical.

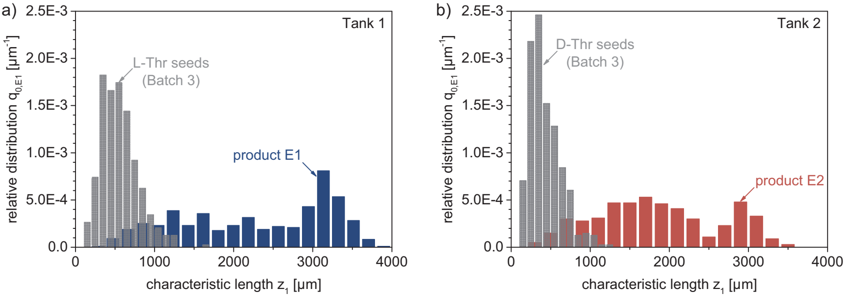

Figure 5.18: Crystal size distributions of the L- and D-Thr seeds (Batch 3) and the final products obtained from Tank 1 and Tank 2 at the end of experiment CPC-FD1.

The obtained product masses summarized in Table 5.11 are similar to the previous experiment CPC1 although the total mass in each crystallizer (490 g) was higher in CPC-FD1 to compensate for the dead volume of the fines dissolution unit. Hence, productivities are slightly lower (cf. Table 5.10). Additionally, purities suffered and there are significant differences between both crystallizers. Partly this can be attributed to the higher level of supersaturation compared to CPC1 as seen in Figure 5.17c,d. Another reason can be found in the technical realization of fines dissolution: the submerged FD-filter (see Figure 4.5) presents an additional surface promoting unspecific nucleation.

Table 5.11: Results of the product analysis from experiment CPC-FD1. T_{cryst} = 30 °C, m_{seeds} = 0.5 g, t_{stop} = 19 h. Values in brackets are estimates based on the concentration signals (eq. (4.10)).

Crystallizer	*Product mass* $m_{IS}^{(p)}$ *[g]*	*Purity* Pu_I *[%]*	*Productivity* Pr_I *[g/(kg h)]*	*Mean crystal size* $\overline{z}_{E1}$ *[µm]*
Tank 1 (L-Thr)	11.4 (15.4)	94.9	10.5	≈ 3200 (seed peak)
Tank 2 (D-Thr)	9.4 (13.9)	98.8	8.6	≈ 3000 (seed peak)

5.3.4 Conclusions from the experiments with fines dissolution

While the dissolution of fines is very beneficial for conventional PC in the sense that it delays nucleation of the impurity and at the same time leads to larger crystals, such improvements were not as pronounced during the presented coupled experiment CPC-FD1. Compared to coupled PC without fines dissolution it can in fact be counterproductive because of the elevated level of supersaturation with respect to *both* enantiomers. This contradicts the idea of CPC whose main purpose is to deplete the supersaturation of the respective counter enantiomer by letting it crystallize in the other vessel. Because of fines dissolution this depletion is slower. As for the coupled benchmark experiment CPC1, we can expect strong improvements regarding purity once the initial level of supersaturation is lowered. However, when employing fines dissolution care has to be taken that the rate of removal and dissolution is faster than the creation of nuclei.

These preliminary experiments on the effect of fines destruction show the principle applicability but did not involve an optimized technical implementation. By visual observation it was noticed that the dissolution of particles entering the fines dissolution unit (FDU) was not entirely quantitative. It is therefore suggested that a heated metal pipe coil be used for increased heat transfer to the suspension. Furthermore, replacing the filters by riser pipes with settling zones might circumvent some of the encountered problems. Especially blockage, which is partly responsible for the lower purity in case of the coupled process, could then be avoided.

A theoretical analysis with a more detailed mathematical description of the FDU such as the one given in eq. (3.47) together with energy balances should be very beneficial to find optimal geometries and necessary heat input along the tubing. Once a robust and quantitative dissolution is implemented, this technique presents an additional option to influence the crystal size distribution during preferential crystallization, which can be important for additional downstream processes.

In the next section we will examine means to further improve the yield of the coupled process. Whereas the yield of conventional PC could be increased by using fines dissolution, lowering the temperature might be a method of choice for the coupled case. We start by subjecting coupled preferential crystallization to various simple linear cooling profiles to assess the implications on process performance and handling.

5.3.5 Polythermal operation of coupled preferential crystallization

Because coupled PC is less likely to suffer from nucleation of the counter enantiomers it was expected that it can tolerate further cooling to improve yield and productivity. Preliminary experiments on polythermal operation of CPC done by Ziomek (2011) showed that purity did not decrease under mild cooling conditions. In this section we look at the effect of stronger cooling to much lower temperatures.

The first experiment involved a decrease of the crystallization temperature in steps of 2 K from initially 30 °C to 20 °C. All other conditions are identical to the isothermal benchmark experiment CPC1 as summarized in Tables 4.3 and 4.4. The resulting concentration decrease of each seeded enantiomer is shown in Figure 5.19a along with the supersaturation trajectories of the counter enantiomers and temperature profiles (Figure 5.19b). The final concentration did not reach the equilibrium value at 20 °C, which is partly caused by strong temperature fluctuations at the end of the process.

At first sight it seems implausible that the temperature decrements do not result in steps in the concentration signals. However, when we again consider the isothermal experiment CPC1 we see that even after 19 h equilibrium was still not entirely reached. Crystallization is not fast enough to produce a notable drop in concentration between the temperature steps imposed in this experiment over a period of 11 h. In that sense the concentration follows temperature in a strongly delayed manner.

Compared to the isothermal case, temperature control becomes increasingly difficult after 6 h due to stronger nucleation and – as a consequence – more frequent blockage of the exchange filters. The values in Table 5.12 show strong differences in terms of mass and purity between both crystallizers. This is a result of the unpredictability of nucleation, which becomes more pronounced under these polythermal conditions.

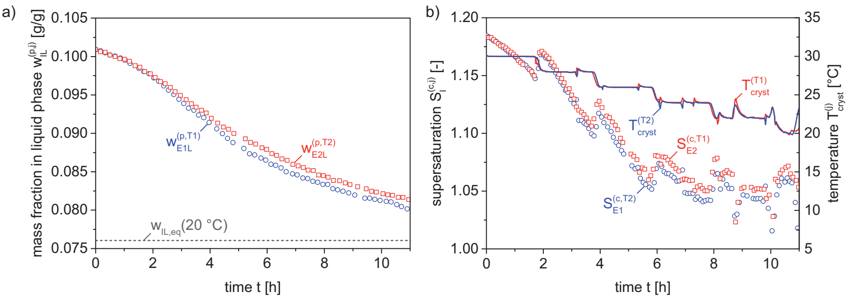

Figure 5.19: a) Concentration profiles of the preferred enantiomers in each crystallizer during experiment CPC3. b) Supersaturation profiles of the counter enantiomers and temperature profiles.

As expected, an overall increase in product mass compared to the isothermal case was achieved. Values reconstructed from the concentration measurement are omitted as they only provide reliable values when no nucleation of the counter enantiomers occurs. During the previous coupled experiments it was assumed that nucleation can be neglected, which is no longer justifiable for the polythermal experiments. Regarding purity we can see that Tank 1 was significantly affected by nucleation of D-Thr. In contrast, product from the second crystallizer shows a similar purity as that obtained from the isothermal experiment CPC1. Again this exemplifies the stochastic nature of nucleation and it is possible that a repetition of this experiment results in different purities.

Table 5.12: Results of the product analysis from the polythermal experiment CPC3. T_{cryst} = 30 °C to 20 °C (stepwise reduction), m_{seeds} = 0.5 g, t_{stop} = 11 h.

Crystallizer	*Product mass* $m_{IS}^{(p)}$ *[g]*	*Purity* Pu_I *[%]*	*Productivity* Pr_I *[g/(kg h)]*
Tank 1 (L-Thr)	17.9	94.9	29.5
Tank 2 (D-Thr)	14.8	98.7	24.2

In order to further investigate the influence of polythermal operation on coupled PC, a set of four experiments was done with different linear cooling ramps:

Case 1:	Immediate cooling from 30 °C to 10 °C at -14 K/h (CPC4)
Case 2:	Immediate cooling from 30 °C to 20 °C at -14 K/h (CPC5)
Case 3:	Delayed cooling from 30 °C to 20 °C at -14 K/h (CPC6)
Case 4:	Immediate cooling from 30 °C to 10 °C at -2 K/h (CPC7)

All other conditions were identical according to Tables 5.3 and 5.4.

The liquid concentrations of each seeded enantiomer are shown in Figure 5.20 for all four processes. Additionally the concentration profile of the seeded enantiomer E1 in tank 1 from the isothermal benchmark experiment CPC1 is indicated by the dashed lines. In all polythermal cases the trajectories suggest almost perfect symmetry between the two crystallizers, which means that the solutions remained nearly racemic.

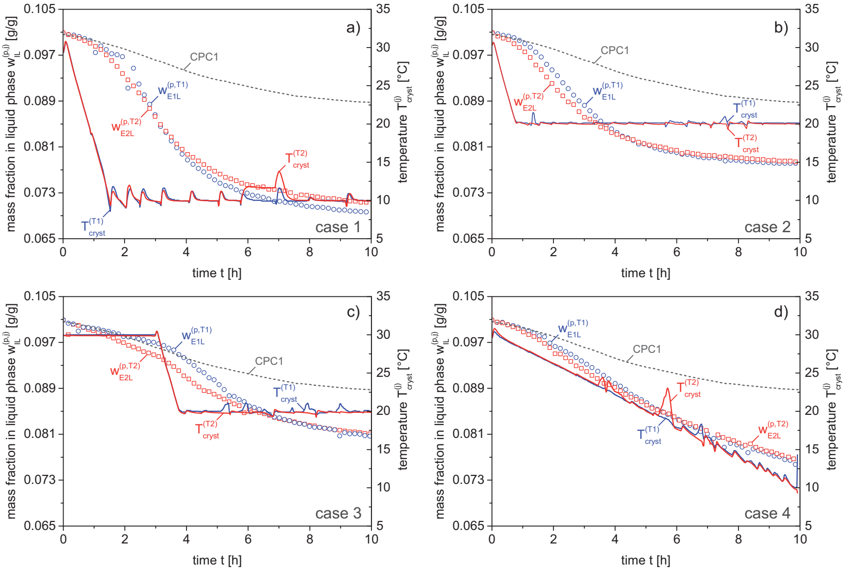

Figure 5.20: Polythermal operation of coupled preferential crystallization using four different linear cooling profiles. Shown are the mass fractions of the seeded enantiomers (E1 in Tank 1, E2 in Tank 2) for experiments CPC4 (a), CPC5 (b), CPC6 (c) and CPC7 (d). The concentration trend of E1 from experiment CPC1 is indicated by the grey dashed lines.

During the first case the process was subjected to the strongest cooling. Figure 5.20a shows that after seeding the rate of crystallization remained at the same level as during the isothermal case for approximately one hour. This can also be observed in the other two cases (2 and 4) were further cooling was started immediately after seeding as well. In case 1 the strong temperature fluctuations indicate that excessive nucleation occurred, which led to temporary reductions of the exchange flow rates due to filter blockage. The milder conditions of case 2 (Figure 5.20b) resulted in less disturbances of the process. The final concentration of the seeded enantiomers in the liquid phase remains at a higher level accordingly. During case 3 (Figure 5.20c), further cooling to 20 °C was started after 3 h, which is notable in the increased concentration decrease after approximately 3.5 h. In the second half of this experiment more frequent filter blockage occurred. The last experiment in this series (Figure 5.20d) was done because it was assumed that slower cooling will allow the seeds to deplete supersaturation more effectively and therefore reduce the chance of unwanted nucleation. Similar to cases 2 and 3, disturbances started to accumulate in the second half of the process.

It has to be mentioned that also ambient conditions had an impact on these four processes. All of them were performed in a warm environment, which resulted in double jacket temperatures down to -10 °C to maintain the slurry temperature. Heat insulation of the crystallizers had only minor effects. The heated solution from the liquid exchange posed an additional disturbance for the temperature control. As a result, high temperature gradients at the inner double jacket wall probably led to local high degrees of supersaturation. In later experiments with the optimized temperature trajectories (section 5.4.3) the exchange lines were extended by a recooling section to minimize these effects.

Based on the solubility as well as the measured temperature and concentration, the level of supersaturation was calculated for each unseeded enantiomer. The results are shown in Figure 5.21. As expected, the increase in supersaturation upon cooling becomes less and less over the series of these experiments. In case 4 it oscillates around its initial value of 1.16. Interestingly we can observe a slight increase after 7 h, which is an indication that the rate of crystallization slows down due to temperature effects on the kinetics.

Judging from the concentration and supersaturation trends (Figure 5.20 and Figure 5.21) we would expect the highest content of counter enantiomer in the product obtained from case 1 and the lowest in the product from case 4. Regarding product mass an increase should be observed in the following order: case 3, case 2, case 4, case 1.

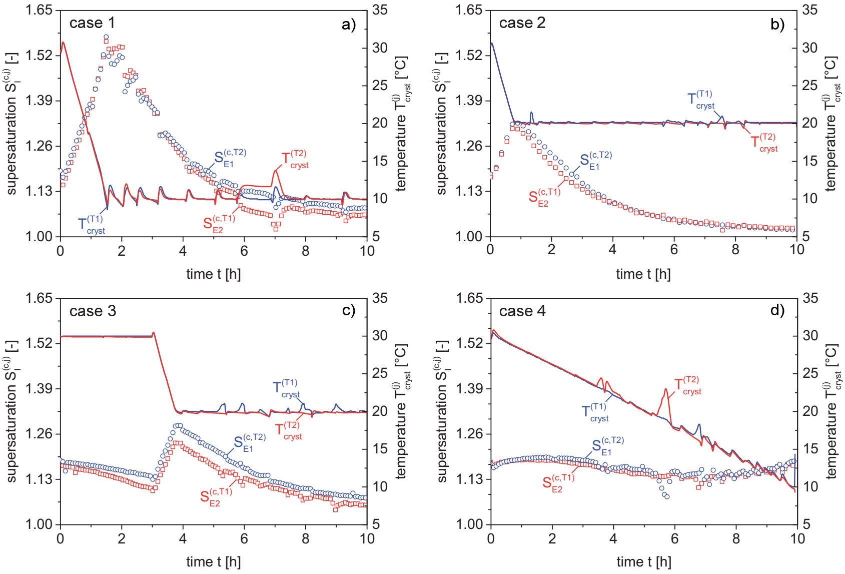

Figure 5.21: Corresponding supersaturation trends of the unseeded enantiomers (E2 in Tank 1, E1 in Tank 2) during polythermal operation of coupled preferential crystallization.

The results of the product analysis summarized in Table 5.13 only partly agree with the expected observation. Although there are differences in the product masses, they do not clearly show the anticipated trend. The same is true for the product compositions. Whereas experiments CPC6 and CPC7 show the highest purities, as expected, the drop in purity from CPC4 to CPC5 does not seem reasonable. Furthermore, the differences in product mass between CPC4 and CPC5 with final temperatures of 10 °C and 20 °C, respectively, should be far more significant. Theoretically an absolute yield of approximately 36 g should be obtained at 10 °C and 26 g at 20 °C in each crystallizer. The extremely strong deviation from these theoretical values is clearly caused by the loss of solid during filter replacement, which was quantified for these experiments.

Table 5.13: Results of the product analysis of the four polythermal coupled experiments CPC4, 5, 6 and 7.

experiment	*Tank 1 (L-Thr)*			*Tank 2 (D-Thr)*		
	product mass [g]	*purity (L-Thr) [%]*	*productivity [g/(kg h)]*	*product mass [g]*	*purity (D-Thr) [%]*	*productivity [g/(kg h)]*
case 1 (CPC4)	17.6	98.6	31.4	16.9	97.0	30.1
case 2 (CPC5)	17.3	97.5	30.8	15.7	94.3	27.9
case 3 (CPC6)	12.5	98.8	22.0	15.9	98.2	28.3
case 4 (CPC7)	15.6	98.4	27.7	16.8	98.1	29.9

Table 5.14 shows the total mass of crystals adhering to the replaced filters as well as the composition[†]. The numbers confirm that considerable amounts are lost and they also show that a significant amount of counter enantiomer (D-Thr in Tank 1, L-Thr in Tank 2) is removed, which has a positive effect on the purity of the final products (Table 5.13). However, this is a random, artificial effect, which distorts the process outcome and makes it difficult to draw definite conclusions on the effect of the four different temperature trajectories on coupled PC. It might therefore be the major reason for the discrepancies between the expected result and the observations. In chapter 5.7 we will use the process model to simulate these four experiments in order to shed more light on the possible effects of polythermal operation.

Table 5.14: Mass and composition[†] of solid adhering to the replaced exchange filter.

experiment	*Tank 1*		*Tank 2*	
	mass [g]	*L-Thr [%]*	*mass [g]*	*D-Thr [%]*
case 1	9.9	49.7	14.2	85.3
case 2	5.11	75.7	8.52	80.5
case 3	6.63	88.4	4.49	78.2
case 4	6.33	86.6	5.18	82.1

[†] The compositions are not entirely accurate because they include mother liquor trapped inside the tightly packed filter cakes, which could not be removed properly without dissolving major parts of the minute crystals. Actual compositions are likely to be slightly higher.

5.4 Control and optimization of coupled batch preferential crystallization

In this section, more advanced operating strategies of coupled preferential crystallization are investigated. All of them involve polythermal temperature trajectories, however, with different goals. In the first set of experiments (section 5.4.1), temperature in one vessel is used as a correcting variable to match the rate of crystallization of the seeded enantiomers in order to regain symmetry upon an initial disturbance. In section 5.4.2 we investigate the applicability of constant supersaturation control to maintain a higher rate of crystallization throughout the process and thereby increase the productivity. Finally, the mathematical model was used to calculate optimal temperature profiles for maximum product mass subject to different purity constraints, which were tested experimentally in section 5.4.3.

5.4.1 Compensation of initial disturbances through control

Coupled preferential crystallization is thought to run best when crystallization in both vessels proceeds symmetrically. It is however very difficult to maintain identical conditions over the course of the entire process especially when secondary or, in the worst case, primary nucleation occurs. The initial conditions can be another source of disturbances. Whereas it is easy to provide identical racemic solutions in both vessels, it is nearly impossible to create two identical populations of seed material. Even when taking only a certain sieve fraction, the CSDs of the L- and D-Thr seeds will always be different as we can see from the distribution parameters of the seed batches listed in table Table 4.2. Additionally, even if identical populations could be obtained there is still no guarantee that the crystals will grow at identical rates because of growth anomalies.

In this section we investigate the experimental application of a symmetry controller, introduced in chapter 3.2.2. The objective was to synchronize the rates at which the seeded enantiomers crystallize by letting the controller adjust the temperature in one tank accordingly. The controlled variable was the difference in concentration of the two seeded enantiomers whereupon the concentration in the master tank served as the setpoint trajectory for the slave crystallizer.

For illustrative purposes an artificial disturbance was induced by seeding Tank 1 with 2 g of L-Thr and Tank 2 with 0.5 g of D-Thr. The effect of this imbalance on the process, when no control measures are taken, is shown in Figure 5.22. Clearly the concentration profiles (a) of the seeded enantiomers E1 and E2 diverge in the first half of the process. Since Tank 1 was seeded with four times the mass as the second vessel, the concentration of L-Thr (E1) decreases faster. This, on the other hand, has the beneficial effect that it is also removed from Tank 2 at a faster rate where it is the unwanted enantiomer. In Figure 5.22b we see that the supersaturation of E1 (unseeded in T2) remains below that of E2 (unseeded in T1). The resulting product analysis for experiment CPC8 (Table 5.15) shows that purity is not affected in a negative sense. It is in fact higher compared to experiment CPC1, which however does not necessarily imply a causal relationship with the different seed masses. It can well be the result of randomness and shall thus be investigated further in chapter 5.7 with the help of the process model.

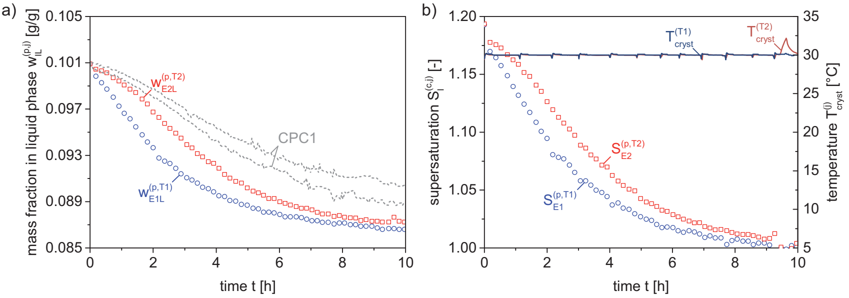

Figure 5.22: Coupled, isothermal experiment CPC8 with unequal initial conditions. Shown are the concentration trends of the two seeded enantiomers of each crystallizer (a) as well as the supersaturation of the unseeded species (b). Grey dashed lines represent the benchmark experiment CPC1. Tank 1 was seeded with 2 g of L-Thr, Tank 2 with 0.5 g of D-Thr.

Regarding the crystal size distributions of the product populations shown in Figure 5.23 we can observe a noticeable difference between Tank 1 and 2. Compared to CPC1, where the distribution of L-Thr was clearly bimodal (Figure 5.15a), the use of four times the mass of seeds apparently reduced the creation of smaller crystals. No significant changes can be seen in the CSD of D-Thr whose seed mass was unchanged. It retained its roughly bimodal character with accumulations around the sizes of 1000 µm and 2500 µm. At the same time, the major part of L-Thr crystals (Figure 5.23a) obtained from CPC8 are at a size around 2000 µm compared to 2800 µm in case of the coupled benchmark experiment. This is a reasonable result because the same amount of dissolved excess is built into approximately four times the number of initially provided crystals.

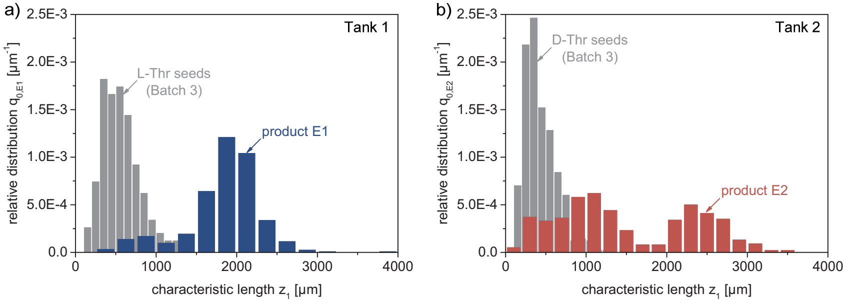

Figure 5.23: Product crystal size distributions of L-Thr (a) and D-Thr (b) obtained from the uncontrolled experiment CPC8 with unequal initial conditions.

The differences in the initial conditions are also reflected by the final product masses given in Table 5.15. After deduction of the seed masses, a difference of 2.4 g between both tanks remains. The following two experiments illustrate the use of the controller to compensate the deviation in concentration encountered during the uncontrolled process. In the first controlled experiment the temperature in Tank 1 was adjusted to decrease the rate of crystallization of L-Thr, whereas in the second one the temperature in Tank 2 was manipulated to accelerate crystallization of D-Thr. In the end, the concentrations should align with the trajectories of the isothermal benchmark experiment CPC1 in the first case and in the second case with the trajectory of L-Thr of the previous uncontrolled process.

In the first controlled experiment, CPC9, the concentration of the seeded enantiomer in Tank 2 (0.5 g of D-Thr) served as the setpoint trajectory for the concentration of L-Thr (2.0 g) in Tank 1. Judging from the measured mass fractions (indicated by ~) of both preferred species shown in Figure 5.24a it was indeed possible to compensate the disturbance and thus synchronize both crystallizers. A slight control deviation remained during the first four hours due to the upper temperature bound, which was set to 34 °C to avoid dissolution of crystals. We can see in Figure 5.24b that the controller increased the temperature in Tank 1 up to this bound in order to slow down crystallization of L-Thr. A higher value would have probably resulted in a complete synchronization but a safety margin was left to account for inaccuracies in the solubility.

During the first 3 hours of the process we observe an oscillating control with decreasing amplitude, which eventually merges into an asymptotic decrease of the temperature in Tank 1 as it approaches 30 °C. The sharp peaks were caused by filter blockage and are thus not the direct result of the controller action. Next to temperature, supersaturation of both preferred enantiomers is shown. Immediately after the start of the process the level in Tank 1 is decreased and remains at a significantly lower value compared to the second crystallizer. Only towards the end they align since the process approaches equilibrium.

Between 1.4 h and 2.7 h, air bubbles in the analytics caused gaps in the measurement signal. Such situation was anticipated during the development of the model based controller and it was therefore a welcome additional disturbance during the initial test. During this period the controller solely relied on the results of the state estimation based on the internal model. The current estimated state (indicated by ^) is represented by the solid lines in Figure 5.24a. These are the values that were actually "seen" by the PI-controller illustrated in Figure 3.6 of chapter 3.2.2. Although the underlying model only considered growth of the *seeded* crystals the estimated trajectory closely matches the actual measurement, which shows that the estimation procedure worked correctly.

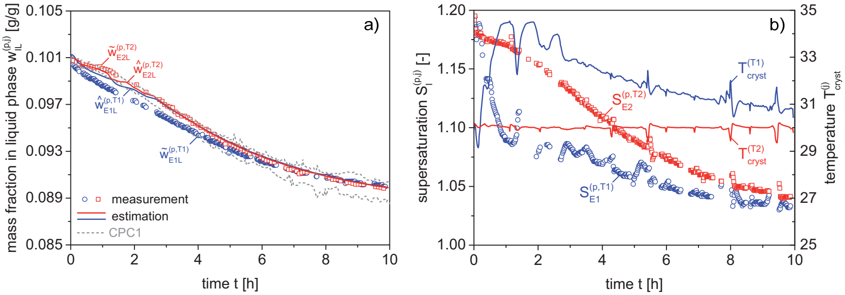

Figure 5.24: Experiment CPC9: application of the symmetry controller when Tank 2 is the master (cf. Figure 3.6). Tank 1 was seeded with 2 g of L-Thr, Tank 2 with 0.5 g of D-Thr. The temperature in Tank 1 was adjusted by the controller so that the concentration of seeded E1 follows the concentration of seeded E2 in the second Tank. a) Measured concentration profiles of the seeded enantiomers (symbols) and the estimation (solid lines) which served as the input for the PI-controller. Grey dashed lines represent the benchmark experiment CPC1. b) Temperature (lines) as well as supersaturation of the seeded enantiomers (symbols).

Regarding the crystal size distributions of the products of experiment CPC9 shown in Figure 5.25, we can see differences compared to the previous uncontrolled process CPC8. The majority of crystals from Tank 1 are located slightly below the size of 2000 μm, which makes sense given the higher overall temperature.

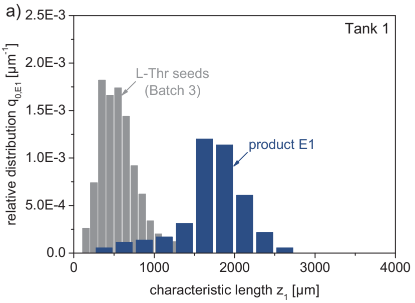

Figure 5.25: Crystal size distributions of the products obtained from experiment CPC9 involving the symmetry controller.

More pronounced differences compared to CPC8 are observed for the second crystallizer in Figure 5.25b, which suggest an increase in the number of smaller particles (≈ 1000 μm) and a decrease in the amount of larger ones (≈ 2500 μm).

The second experiment (CPC10) investigating the application of the model based symmetry controller was started with the same unequal initial conditions as the previous two. As opposed to CPC9, the concentration trajectory of the seeded enantiomer in *Tank 1* (2.0 g of L-Thr) was the setpoint for D-Thr seeded in Tank 2. Since Tank 1 was seeded with four times the mass of D-Thr seeds in Tank 2, the rate of crystallization in the second vessel had to be increased. To do so, the model based controller temporarily decreased the temperature in Tank 2 as depicted in Figure 5.26b. Due to technical reasons the lower bound for the temperature was set to 10 °C but was not exhausted.

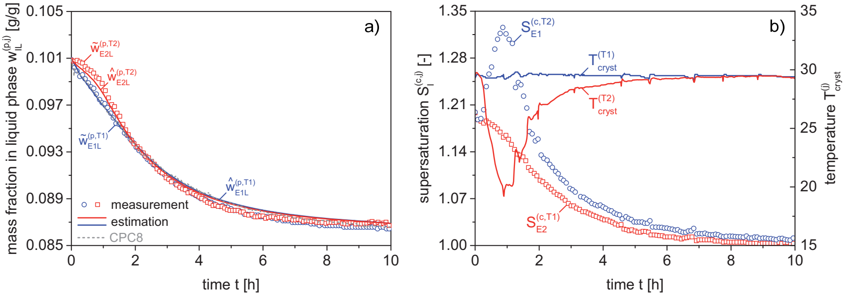

Figure 5.26: Experiment CPC10: application of the symmetry controller when Tank 1 is the master (cf. Figure 3.6). Tank 1 was seeded with 2 g of L-Thr, Tank 2 with 0.5 g of D-Thr. The temperature in Tank 2 was adjusted by the controller so that the concentration of seeded E2 follows the concentration of seeded E1 in the first Tank. a) Measured concentration profiles of the seeded enantiomers (symbols) and the estimation (dashed lines) which served as the input for the PI-controller. b) Temperature (lines) and supersaturation of the respective counter enantiomers (symbols).

As seen in Figure 5.26a the concentrations of the seeded enantiomers are almost identical throughout the entire process and follow the trajectory of L-Thr found in the uncontrolled experiment CPC8, which is depicted by the grey dashed line. Although a further decrease in temperature can promote unspecific nucleation of the counter enantiomer, as was the case in the polythermal experiment CPC5 (case 2), temporary cooling to 20 °C during CPC10 resulted only in a minor contamination of the product from Tank 2 with L-Thr (see Table 5.15). This is also due to the faster crystallization of L-Thr in Tank 1.

As a consequence of the increased supersaturation in Tank 2 the product size distribution of D-Thr shown in Figure 5.27b suggests an increased formation of particles below the size of 1000 µm compared to experiments CPC1 and CPC8. This is a reasonable result considering the transient reduction in temperature, which also led to slightly lower product purity (Table 5.15).

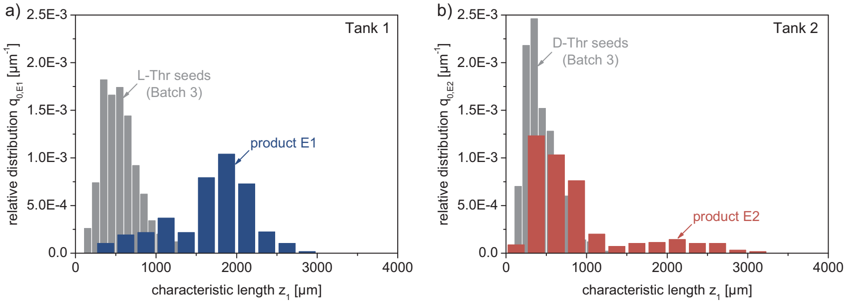

Figure 5.27: Product crystal size distributions of experiment CPC10 obtained from Tank 1 (a) and Tank 2 (b).

When we look at product yield and purity of the three processes discussed above (Table 5.15) it appears that the initial disturbance induced by the different seed masses had no negative effect. In fact, the uncontrolled experiment CPC8 had the best performance and the highest purity. Compared to CPC9, we notice that the product masses are generally higher. In case of Tank 1, this is not surprising since crystallization was slowed down by the increase in temperature during CPC9. The significantly lower yield in Tank 2 on the other hand was probably caused by the irreproducible removal of crystals adhering to the exchange filters.

Table 5.15: Results of the product analysis of the uncontrolled experiment CPC8 with unequal seed masses and the two experiments using the symmetry controller, CPC9 and CPC10. In all cases Tank 1 was seeded with 2 g of L-Thr and 0.5 g of D-Thr taken from batch 3 (see Table 4.2). Process duration was 10 h.

experiment	*Tank 1*			*Tank 2*		
	product mass [g]	*purity (L-Thr) [%]*	*productivity [g/(kg h)]*	*product mass [g]*	*purity (D-Thr) [%]*	*productivity [g/(kg h)]*
CPC8 (uncontrolled)	15.4	99.2	24.6	11.5	99.5	20.2
CPC9 (control in T1)	12.6	99.3	19.5	9.4	98.8	16.3
CPC10 (control in T2)	15.0	99.2	23.9	12.0	98.0	21.1

The last experiment of this series, CPC10, again yielded higher product masses, similar to the uncontrolled process CPC8 because of the reduction in temperature in the second crystallizer and thereby faster crystallization. Regarding differences in final product mass over the course of the three processes, results from Tank 1 show a qualitatively reasonable trend that can be directly attributed to the process conditions: a reduction in case of CPC9 and similar yields during the experiments where temperature was not manipulated in the first crystallizer. In light of the uncertainties caused by the aforementioned removal of crystals via the replaced filters (see also section 5.3.5), the results of the product analysis in Table 5.15 should be considered with care.

From a control engineering perspective, this first experimental application of the model based controller was successful. The demonstration showed that a very simple underlying process model (only seed growth) is already sufficient and a stable control can be achieved. In the presented processes, the control objective was the synchronization of crystallization of the seeded enantiomers since preliminary considerations concluded that symmetry between the two crystallizers is advantageous for coupled PC. The uncontrolled experiment CPC8, however, showed that this is apparently not absolutely necessary since the artificially induced asymmetry had no negative effects on purity. Nevertheless, we have to keep in mind that due to the rather small experimental scale any technical disturbance, such as filter blockage or fluctuations in temperature of the periphery, can randomly influence the process and make it difficult to observe the actual effects of the chosen process conditions.

The control toolbox developed during the dissertation of Steffen Hofmann from the group of Prof. Jörg Raisch at TU Berlin can be easily adapted to realize other control objectives. Apart from symmetric liquid phase concentration trends it can also be of interest to obtain equal crystal size distributions. As we saw in the previous three experiments, the final CSDs obtained from each crystallizer were quite different. This is, however, a very challenging control objective, since it requires an observation of the solid phase. Unless the underlying model perfectly describes the process, an online measurement is needed. A theoretical treatment of an optimal control problem to achieve a desired CSD is presented in Hofmann, et al. (2014). Its experimental application could be an interesting subject for future studies in the context of preferential crystallization.

In the next chapter, we will investigate the control of the driving force using the provided toolbox. The objective was to achieve a constant level of supersaturation starting from symmetric initial conditions.

5.4.2 Constant supersaturation control

With the exception of the polythermal experiment CPC7 presented in chapter 5.3.5, all of the previous coupled experiments eventually exhibited a reduction of the driving force. Their productivities therefore gradually decreased towards the end of the chosen process duration. In order to maintain a certain level of supersaturation to prolong the period of higher productivity, continuous further cooling can be applied as was shown in chapter 5.3.5. From the preliminary polythermal experiments in that chapter we know that arbitrary temperature profiles can lead to unwanted nucleation when supersaturation is increased prematurely. This became apparent during experiments CPC4 and 5 (cases 1 and 2) were immediate further cooling was applied. The delayed cooling in case 3 prevented the initial strong build-up of the driving force, which led to better product purities. Case 4 already showed a quite constant level of supersaturation around S = 1.16 and resulted in crystals with a purity above 98%.

The following experiment, CPC11, uses the constant supersaturation controller introduced in chapter 3.2.3. Based on the results obtained from CPC7 (case 4) a setpoint of S = 1.15 was chosen. It was decided to control the supersaturation of the respective *counter* enantiomers to avoid a possible increase in their driving force, which could provoke nucleation. Such scenario could occur when the seeded enantiomer nucleates in the opposite vessel or the exchange of solution between the crystallizers becomes insufficient while the supersaturations of the seeded enantiomers are controlled.

Figure 5.28 shows the evolution of the liquid phase concentrations in each crystallizer (a, b) and the corresponding supersaturation trends (c, d). The estimated concentrations are displayed as solid lines in the top two figures. We can see that the estimation of the current liquid phase composition, based on the seed-growth-only model, reflects the measured data very well. This is important because supersaturations of the counter enantiomers – the controlled variables – were calculated based on these estimates. In Tank 1 (Figure 5.28c) it was possible to almost perfectly keep the driving force of D-Thr at the setpoint of S = 1.15, which is confirmed by the measurement (E2, red squares).

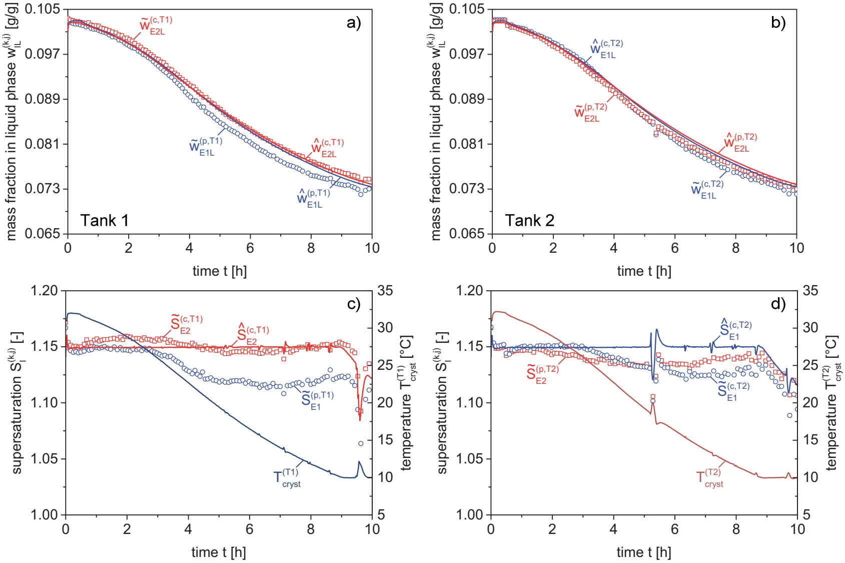

Figure 5.28: Application of the constant supersaturation controller in experiment CPC11. a, b) Measured (symbols, ~) and estimated concentration (lines, ^). The latter was used to calculate the current supersaturation estimate. c, d) Supersaturation calculated from concentration measurements (symbols) together with estimated values of S (lines) and temperature T_{cryst}.

After nine hours it decreased since the lower temperature bound (10 °C) was reached. The sharp peak in the temperature signal was again caused by strong filter blockage. From the perspective of the controller, no control deviation occurred for the first nine hours of the process. Except for small peaks, the estimated supersaturation of D-Thr (red line) remained exactly at the setpoint value. The trend of the supersaturation of the seeded enantiomer in Tank 1, L-Thr, dropped below $S = 1.15$ after about 3 h, which was likely due to nucleation in the second crystallizer. Control of the supersaturation of the seeded enantiomer would have caused a stronger reduction of the temperature by the controller in Tank 1 provided that the estimation of the E1-concentration had been more accurate: we can see in Figure 5.28a that the concentration of E1 was slightly overestimated (blue line), thus the calculated supersaturation was higher than the measured one.

In Tank 2, the estimated supersaturation of the counter enantiomer E1 is kept equally constant by the controller, except for a strong disturbance due to filter blockage after 5 h (Figure 5.28d). The supersaturation calculated from the measurement signals (blue circles), however, diverges from the estimate after 3 h, which indicates nucleation of L-Thr (E1) in Tank 2. From this point forward the simplification in the underlying model that only seed growth can occur is not sufficient to reflect the measurements. The results of the product analysis, summarized in Table 5.16, support the assumption of a nucleation event of the counter enantiomer in the second crystallizer.

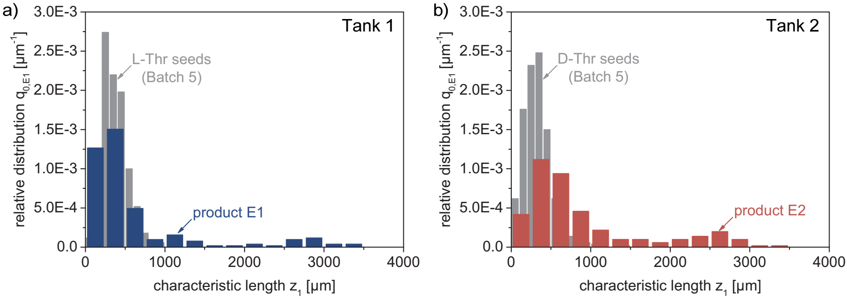

Figure 5.29: Product crystal size distributions obtained from experiment CPC11 using constant supersaturation control.

In comparison with the isothermal benchmark experiment CPC1, the product CSDs shown in Figure 5.29 indicate a minor increase of the mean size of the seed populations, which are located near the length of 3000 μm. However, we have to bear in mind that the seeds used in this experiment CPC11 were taken from Batch 5 and were generally smaller (see Table 4.2). In the size range below 1000 μm, a higher amount of smaller particles is encountered, which is due to the higher overall driving force. Compared to the experiments involving the symmetry controller discussed in section 5.4.1 the CSDs obtained from each crystallizer are more similar as a result of the symmetrical conditions. In terms of productivity, operation at constant supersaturation provided an almost fourfold increase compared to the isothermal case with acceptable purity. So far, the results summarized in Table 5.16 show that the investigated process has the best performance of all coupled processes discussed in this work. However, the purity obtained from Tank 2 suggests that the setpoint of S = 1.15 was still too high.

Table 5.16: Results of the product analysis from experiment CPC11 using constant supersaturation control. $m_{seeds} = 0.5$ g, $t_{stop} = 10$ h.

Crystallizer	*Product mass* $m_{IS}^{(p)}$ *[g]*	*Purity* Pu_I *[%]*	*Productivity* Pr_I *[g/(kg h)]*
Tank 1 (L-Thr)	22.6	98.6	40.6
Tank 2 (D-Thr)	23.7	96.0	42.6

Up to now we have looked at different means to improve the performance of coupled preferential crystallization. Starting from an isothermal mode of operation, fines dissolution was applied as well as polythermal cooling policies. In the last two chapters, two different control strategies were tested that made use of a simplified process model. While the first strategy had the aim of restoring symmetry between both crystallizers, the last one aimed at actually increasing the productivity. In the next chapter we will make use of the full process model described in chapter 3.1 to perform an optimization of coupled preferential crystallization. The investigated process will thus be evaluated in terms of its limits by exhausting the metastable zone. Additionally, this presents an opportunity to validate the model and assess the quality of calculated predictions.

5.4.3 Optimized polythermal operation of CPC

The previous chapters already investigated some aspects of polythermal operation of CPC and showed that even though this process strategy reduces the chance of nucleation of the unseeded enantiomer, further cooling is still not straightforward. This became particularly evident during the application of arbitrarily chosen linear temperature profiles that were discussed in chapter 5.3.5. In this chapter we will use the knowledge about the process contained in the full model described in chapter 3.1 to find optimal temperature profiles. The goal is to maximize the product yield after the fixed duration of 10 h given different final purity constraints. The procedure as well as the formulation of the optimization problem is explained in chapter 3.2.4. At the time this optimization was done, a different set of values of the kinetic parameters listed in Table 5.2 was used. They were the result of a preliminary parameter estimation employing the conventional and coupled preferential crystallization processes used in the final parameter estimation of this work. The preliminary values are summarized in Appendix 7.5.

Figure 5.30a shows the optimal temperature trajectories for five different purity constraints as well as the result of an unconstraint optimization run (dashed curve). In all cases the lowest allowed temperature was 10 °C. The corresponding simulated trends of the supersaturation of the seeded enantiomer in Tank 1 are shown in Figure 5.30b. All temperature profiles begin with a moderate cooling rate, which increases more rapidly at some point. This point is shifted to later times as the purity constraint is increased. The shape of the cooling profiles is similar to the one calculated by Angelov, et al. (2008a) for conventional PC and makes sense. In the beginning, a strong increase of the supersaturation is avoided to prevent nucleation of the counter enantiomers in each of the two crystallizers. During this period, the total surface areas of the seeded enantiomers increase. By the time the maximum cooling rate is reached, enough crystal surface area of the preferred species is available to rapidly deplete the supersaturation. Compared to the polythermal experiments CPC4 and CPC5 (chapter 5.3.5), which were immediately cooled to 10 °C and 20 °C, respectively, the maximum supersaturation predicted by the model using the optimized temperature profiles is S = 1.33.

At this point the legitimate question arises why the calculated profiles were tested experimentally even though their predicted supersaturation levels exceed values that led to nucleation of the unseeded enantiomers during some of the previously discussed coupled experiments. As mentioned earlier, the parameter values of the model used for this optimization were obtained from a previous estimation that also involved five additional coupled experiments. It was assumed that the total of 11 different experiments would result in better estimates. Only at a later stage of this work it became apparent that this additional information was misleading due to the unpredictable removal of crystals via the replaced exchange filters, which is not considered in the model. As a consequence, this previous set of parameter values underestimates nucleation of the counter enantiomers and therefore leads to steeper cooling trajectories.

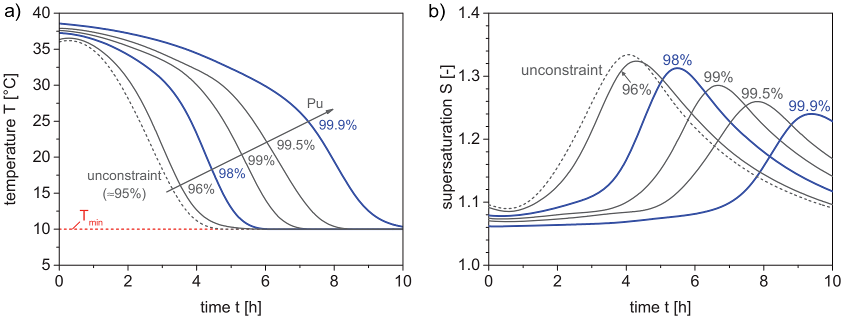

Figure 5.30: Calculated optimal temperature trajectories for coupled PC with different purity constraints Pu (a) and the resulting simulated supersaturation trends of the seeded enantiomer in Tank 1 (b). The bold blue trajectories (98% and 99.9%) were investigated experimentally. The dashed lines are the result of an unconstraint optimization. The lowest purity that still leads to a maximization of the product mass is approximately 95%.

Even with this "optimistic" set of parameter values, we can see from Figure 5.30a that the initial temperatures, resulting from the optimization, are much higher (> 30 °C) than those used in the previous experiments. The initial supersaturation must apparently be lower in order to comply with the purity constraints. Based on the unconstraint optimization it is evident that the maximization of the final product mass is only possible down to a purity of approximately 95%. Below this threshold, the allowed contamination leads to a decrease of the product yield as it nucleates in the respective opposite crystallizer.

In chapter 3.2.4, the optimization algorithm was formulated in a way so that each of the two coupled crystallizers eventually has a unique temperature trajectory. Due to the complexity of the problem and the resulting long computation times, complete symmetry between both tanks was assumed. Thus, only one temperature profile was optimized, which was applied to both crystallizers. However, the initial seed populations of L- and D-Thr were parameterized according to the actual seed batch 5 (see Table 4.2), which was later used in the experiments. For that reason, the purity constraint could only be satisfied in one tank. Table 5.17 shows the values of the objective function – the final product masses, m_{IS} – and the purities obtained for each of the chosen constraints. The purity of the product from Tank 2 was used in the evaluation of the constraint function because of the slightly smaller D-Thr seeds. Since the seed masses were the same in both crystallizers, the total surface area of the D-Thr seeds was larger than that of the L-Thr seeds. The contribution of eq. 3.23 therefore resulted in a slightly higher nucleation rate of the counter enantiomer in Tank 2.

Apart from the optimized temperature trajectories shown in Figure 5.30, it is also interesting to look at the values of the objective function as well as the actual purities after each optimization run. These values are summarized in Table 5.17 and show that the optimizer always exhausted the constraint in Tank 2. Purities in Tank 1 are slightly higher due to the reasons mentioned above. As expected, the value of the objective function rises with decreasing purity constraint. A challenge that arises from such an optimization is to judge whether the solution is a local or a global optimum. In case of the parameter estimation discussed in chapter 5.1 this can hardly be evaluated, partly because of the cross-correlations between certain model parameters. No hard proof can be provided for the optimized temperature profiles either. However, we can qualitatively take a look at how certain characteristic points depend on the chosen purity constraints. Reasonable candidates are, for example, the value of the objective function itself, the initial temperature, the maximum supersaturation and the time at which it is reached. In Appendix 7.6 a graphical representation of these dependencies are given. The curves depicted therein are mostly monotonic and generally seem to follow a common trend with only some deviations. This is at least an indication that each optimization terminated at a reasonable solution, which is possibly close to a global optimum.

Table 5.17: Simulated results of optimized CPC showing the predicted final product masses, m_{IS} (objective function), and purities, Pu_I, for different purity constraints, Pu_{min}.

Pu_{min}	*Tank 1*		*Tank 2*	
	m_{E1S} [g]	Pu_{E1} [%]	m_{E2S} [g]	Pu_{E2} [%]
99.9%	23.04	99.91	23.22	99.90
99.5%	27.08	99.54	27.28	99.50
99%	28.58	99.07	28.77	99.00
98%	29.69	98.13	29.88	98.00
96%	30.26	96.21	30.45	96.00
unconstraint	30.31	95.38	30.50	95.15

The two calculated trajectories optimized for 98% and 99.9% purity (bold blue lines in Figure 5.30a) were validated with four experiments. For the first three experiments – CPC12 its repetition CPC12a and CPC13 – seeds from Batch 5 were used. The distribution parameters of this seed batch were also used in the optimizations. For the fourth experiment, CPC14, milled seeds were used to increase the rate of crystallization; however no optimization was done for such small seeds. In all cases, 0.5 g of seed crystals were used for each crystallizer. The experimental conditions of CPC12 were identical to those summarized in Table 4.3 and Table 4.4. For the remaining three processes – CPC12a, CPC13 and CPC14 – the initial solutions were prepared according to Table 5.18. The higher total mass of the solutions in each crystallizer was chosen to account for the dead volume of an additional cooling section in the exchange paths, which was installed after CPC12.

Table 5.18: Initial solution composition in each crystallizer for the optimized coupled processes CPC12a, CPC13 and CPC14.

description	*process parameter*	*value*
mass of solvent	m_{H2O}	380 g
mass of L-Thr	m_{E1}	48.035 g
mass of D-Thr	m_{E2}	48.035 g
saturation temperature	T_{sat}	43.7 °C (eq. (4.1))

Figure 5.31 shows the concentrations, w_{IL} of L- and D-Thr (I = E1, E2) as well as the measured temperature, T_{cryst}, in each crystallizer during the validation of the two optimized temperature profiles. Apart from the experimental conditions already mentioned, the processes were operated as follows:

CPC 12:	Optimized for 98% final purity, Batch 5 seeds	(Figure 5.31a, b)
CPC 12a:	Repetition of CPC12	(Figure 5.31a, b)
CPC 13:	Optimized for 99.9% final purity, Batch 5 seeds	(Figure 5.31c, d)
CPC 14:	Optimized for 99.9% final purity, milled seeds	(Figure 5.31e, f)

During all four experiments, the realization of the optimized temperature profiles was successful. Every minute, a new setpoint from the pre-calculated trajectories, was sent to each thermostat. The evolutions of the liquid phase concentrations show that crystallization in both vessels proceeded nearly symmetrical in all cases. Furthermore, experiment CPC12 and its repetition, indicated by the open symbols, show a very high degree of reproducibility.

Compared to the isothermal benchmark experiment CPC1 shown by the dashed curve in each plot for Tank 1, the decrease in concentration during CPC12 and 13 was slower in the beginning because of the higher initial temperature. The operating temperature of the isothermal process (30 °C) was reached after approximately three and six hours, respectively. Only the use of milled seeds in CPC14 compensated the lower driving force for crystallization during the first half of the process.

The two validated temperature trajectories have a clear impact on the measured concentration trends, which is obvious when comparing experiments CPC12 and 13 (Figure 5.31a-d). However, for the first 60 minutes the concentrations of the two processes appear to be almost identical despite the differences in temperature and supersaturation. Although it cannot be excluded that the initial change in concentration is below the detection limit of the analytics, such behavior was already observed during the polythermal experiment CPC4 in comparison with the isothermal case CPC1 (cf. Figure 5.20a in section 5.3.5). A possible reason is that the amount of seeds and thus the initial surface area is not large enough to produce a notable drop in concentration. It could also be the result of an initial dynamic phase during which the crystals do not yet crystallize at the maximum possible rate. This can certainly also depend on the specific batch of seed material. In case of CPC14 (Figure 5.31e,f), for which milled seeds were used, an instant decrease in concentration was measured as opposed to CPC13. Clearly the rate of crystallization was higher, which resulted in a significantly lower final concentration.

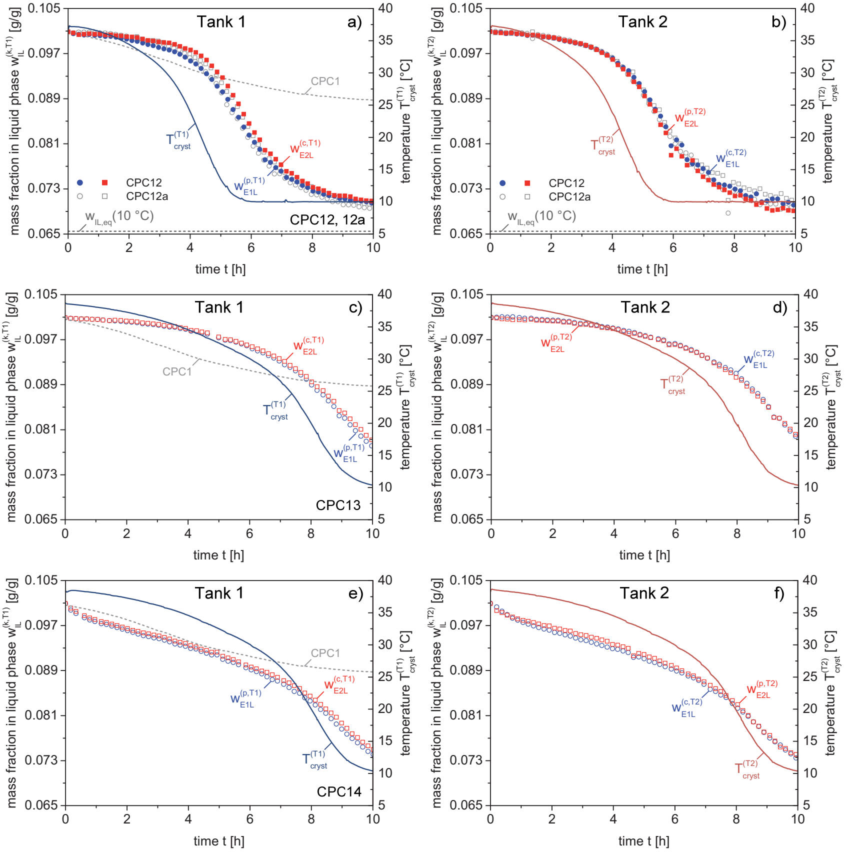

Figure 5.31: Concentrations w_{E1L} and w_{E2L} of L-Thr (blue circles, seeded in T1) and D-Thr (red squares, seeded in T2) and temperature trajectories in each crystallizer obtained from the optimized experiments CPC12 and CPC12a (a,b), CPC13 (c,d) and CPC14 (e,f). In experiments CPC12/CPC12a a temperature trajectory optimized for 98% purity was used. The second trajectory used for CPC12 and CPC14 was optimized for 99.9% purity. Unlike the first two experiments, milled seeds were used in CPC14.

Regarding the evolution of the supersaturation, shown in Figure 5.32, we see the strongest build-up during experiment CPC12. From the previous polythermal experiments it is clear that the metastable zone was exceeded, which is also reflected by the product purities given in Table 5.17. The maximum of the supersaturation curve is shifted to a later point in case of experiment CPC13 as predicted by the simulation in Figure 5.30b. However, the simulated trend of the supersaturation for 99.9% final purity (Figure 5.30b) shows an almost constant level during the first six hours, which is not the case in the experimental validation (CPC13). This indicates that the seeds crystallized at a slower rate than predicted by the model. As a consequence, the supersaturation of the counter enantiomers is depleted more slowly, which increases the chance of nucleation. The measured product purities of CPC13 in Table 5.19 confirm that the respective unseeded enantiomers nucleated in each crystallizer.

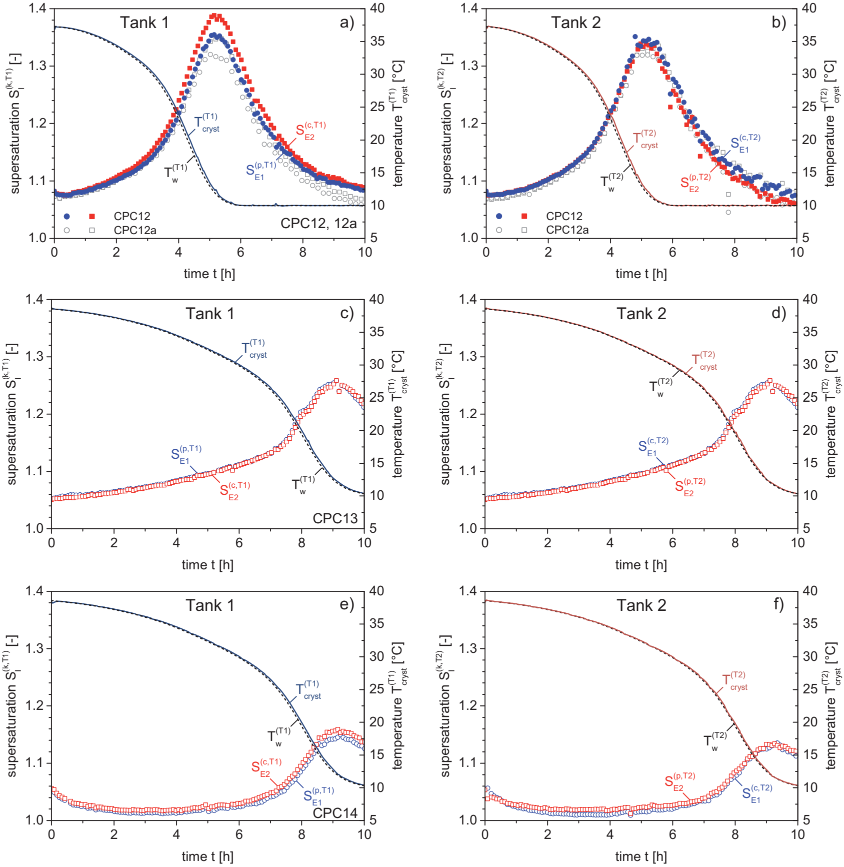

Figure 5.32: Supersaturation S_{E1} andS_{E2} of L-Thr (blue circles, seeded in T1) and D-Thr (red squares, seeded in T2), respectively, during the validation of two optimized temperature profiles. Next to the measured temperature T_{cryst}, the setpoint trajectories, T_w, are shown.

In the last experiment of this series, CPC14, the increase of the measured supersaturation towards the end of the process was not as pronounced. As shown in Figure 5.32e,f, the liquid phase remained close to saturation during the first six hours. Due to the high surface area of the milled seeds the supersaturation generated by the cooling profile is depleted almost instantaneously. In that sense crystallization is limited by the driving force, which is almost quasi-stationary for the first half of the process. During this period it is very unlikely that nucleation of the unseeded enantiomers occurred. We have to consider that the temperature trajectory for 99.9% purity was optimized for the seeds from Batch 5, which were much larger than the milled seeds. Still an increase in supersaturation occurred after seven hours, which, however, did not affect the purity of the final product as shown in Table 5.19.

When we examine the final product masses in Table 5.19, it is obvious that the first three processes suffered from strong nucleation in at least one of the two crystallizers. As already expected, due to the high level of supersaturation during CPC12, the cooling rate of the temperature profile optimized for 98% purity was too fast. The strong nucleation, which occurred in Tank 2 is also the reason for the low absolute yield in Tank 1. A slight improvement was achieved by the installation of the cooling sections, which were first used during the repetition CPC12a. With this addition, the maximum temperature difference between the slurry and the cooling agent could be reduced from 15 K to less than 5 K, which resulted in a higher overall purity in experiment CPC12a and a smaller difference regarding the product masses from each tank. The effects on the temperature control of the cooling section are shown in Appendix 7.7.

The more moderate cooling profile applied in experiment CPC13 already resulted in acceptable purities and an even smaller difference between the product masses. However, also in this case, the calculated temperature trajectory led to more nucleation than predicted by the model. For this reason, milled seeds were used in the last experiment CPC14, while using the same temperature profile. Clearly, the high surface area of the seeds resulted in a very fast removal of the enantiomers from the solution and thus prevented primary nucleation, which is reflected by the high purities. The combined product mass is significantly higher compared to experiment CPC12, although the final concentration remained at a higher value (Figure 5.31e,f). This is due to the strong nucleation and thus bigger losses due to crystals adhering to the exchange filters in case of CPC12. Figure 5.33 shows how these losses could be reduced over the course of the four optimized polythermal experiments.

Since the discussion of these experiments already involved a lot of information, the results of the product sieve analyses shall not be addressed in detail at this point. They are presented in Appendix 7.8.

Table 5.19: Results of the product analysis of the optimized polythermal experiments.

experiment (purity constraint)	*Tank 1*			*Tank 2*		
	product mass [g]	*purity (L-Thr) [%]*	*productivity [g/(kg h)]*	*product mass [g]*	*purity (D-Thr) [%]*	*productivity [g/(kg h)]*
CPC12 (98%)	17.03	98.3	28.7	28.37	83.7	48.4
CPC12a (98%)	28.20	92.0	48.1	24.08	97.1	40.9
CPC13 (99.9%)	20.35	98.9	34,4	21.54	96.8	36.5
CPC14 (99.9%)	28.95	99.6	49.4	28.40	99.4	48.4

The goal of these experiments was to find a suitable trajectory that would guide the process through the metastable region to obtain the maximum possible amount of product while avoiding nucleation of the counter enantiomers. The maximum possible yield was limited by the process duration (10 h) and the lowest allowed temperature (10 °C). It was already attempted to achieve this goal during the polythermal experiments discussed in chapter 5.3.5. Of the four preliminary cases summarized in Table 5.13 of that chapter, experiments CPC4 and CPC7 have to be considered as they had the same global process boundaries (10 h, 10 °C) as the optimized experiments. At the chosen lowest temperature, the maximum theoretical yield of pure solid product is approximately 36 g in each crystallizer given the scale and initial process conditions used in this work ($T_{sat,0}$ = 43.7 °C).

Although the two experiments using the linear cooling profiles showed slightly better overall purities, the obtained product masses were lower. Even the moderate optimized cooling profile (CPC13) resulted in more product with similar purity than the harshest linear cooling used in this work (CPC4). In order to further evaluate a possible advantage of the optimized over the linear temperature trajectories, we must also consider the loss of solid caused by the technical issues at this experimental scale. In Figure 5.33 we see that CPC4 suffered from the highest losses in both crystallizers. The slow linear cooling during CPC7 already reduced this amount. Within the series of the optimized experiments we can see a steady decrease from CPC12 to CPC13. The last experiment (CPC14) should be excluded from this discussion because its conditions were generally more favorable because of the use of milled seeds. Since the masses that are lost via the filter frits, correlate with the magnitude of nucleation that takes place in each vessel, we can conclude that the trajectory optimized for 99.9% purity (CPC13) provided the most favorable conditions. Compared to experiments CPC4 and CPC7 a significantly higher amount of product at almost identical purities was obtained. At the same time the smaller amount of loss indicates that less nucleation took place.

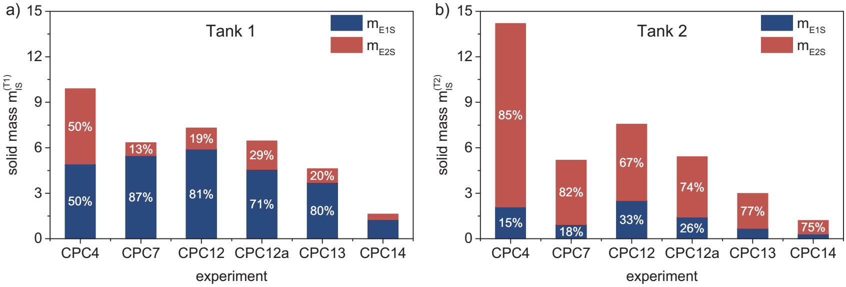

Figure 5.33: Total masses lost via the replacement of the exchange filter frits during the optimized coupled experiments (CPC12 – CPC14) compared with the two previous polythermal experiments CPC4 and CPC7. Also indicated are the compositions of the solid adhering to the filters.

The conclusions that can be drawn from these optimized experiments are not straight forward, due to the technical aspects that have to be considered as well. Certainly, we can say that the model underestimated nucleation, which is why the calculated temperature trajectories did not result in the predicted purities, with the exception of the last experiment.

However, when considering product yield, purity and the loss of crystals, we can conclude that the optimized trajectories generally lead to a better process performance than arbitrarily chosen linear cooling. From a modeling point of view, the validation of these optimized trajectories made it very clear that a good understanding of the process is required. In the context of crystallization an optimization usually means that the process is operated close to the border of the metastable zone width. Especially in preferential crystallization, where the impurity shares identical properties with the product, an insufficient model can easily jeopardize the process. Nevertheless, despite the inaccuracies of the model predictions regarding nucleation, its use in the planning of the discussed polythermal PC processes resulted in significant improvements.

With this last set of coupled preferential crystallization experiments (CPC), we conclude the investigation of this process concept. In comparison to conventional PC, the benefits of coupling two crystallizers became evident. Due to the simultaneous crystallization of both enantiomers in separate vessels the process becomes more flexible regarding means to increase the productivity. Apart from the possibility to apply different control concepts, CPC is generally more apt for polythermal operation. Conventional PC is strongly limited by the induction time of nucleation of the unseeded enantiomer. This challenge can be almost entirely eliminated with CPC given the right process conditions, which were not the most favorable in the discussed experiments. They included the use of rather large seed crystals and in most cases an initial degree of supersaturation, which was already close to the border of the metastable zone. This combination resulted in a slow rate of crystallization and an increased chance of nucleation. However, most of the experiments resulted in product purities above 98%, which shows that CPC was able to tolerate these conditions. We can therefore safely assume that more moderate degrees of supersaturation in conjunction with smaller seeds will result in a very robust process.

In the following chapter, we will again use the coupled concept but purposely operate it under completely asymmetric but isothermal conditions.

5.5 Coupling preferential crystallization and selective dissolution

A particularly interesting way of using two coupled vessels, to separate enantiomers of the conglomerate forming type, is to operate them at two different temperatures, which was outlined in chapter 2.5. One crystallizer is operated in the supersaturated region while the second remains at the initial saturation temperature. Initially, both tanks contain identical racemic solutions; however, solid racemate is added to the second one creating a saturated racemic suspension. In the first tank, enantiopure seeds are added to start preferential crystallization. Through the continuous exchange of solution between both vessels, we essentially combine conventional PC with selective dissolution. This has already been described in the patent of Krieger et al. (1965) and a detailed experimental and theoretical investigation of this process concept was published by the author of this work in Levilain et al. (2012) and Eicke et al. (2013). We will use the term coupled preferential crystallization and dissolution (CPC-D) for this process concept. In the following, three experiments will be discussed whose process conditions are summarized in Table 5.20. The first covers the entire dynamics until thermodynamic equilibrium and will be used as an illustrative example to understand the process concept. The second and third were stopped earlier to analyze the products and assess the performance.

Table 5.20: Initial solution composition and operating conditions for three coupled PC and selective dissolution (CPC-D) experiments. The mass of racemic DL-Thr is denoted as m_{rac}.

process parameter		*CPC-D1*		*CPC-D2*		*CPC-D3*	
		Tank 1	*Tank 2*	*Tank 1*	*Tank 2*	*Tank 1*	*Tank 2*
liquid phase	m_{H2O}	369.83 g		359.19 g		359.19 g	
	m_{E1L}	-		-		45.405 g	
	m_{E2L}	-		-		45.405 g	
	m_{racL}	93.84 g	93.89 g	94.81 g	94.81 g	-	
solid phase	$m_{E1seeds}$	2 g $^{*)}$	-	2 g $^{**)}$	-	2 g $^{**)}$	-
	m_{racS}	-	20 g	-	20 g	-	20 g
	T_{cryst}	36 °C	45 °C	34 °C	44 °C	34 °C	45 °C
	F_{ex}	20 mL/min		11 mL/min		11 mL/min	

$^{*)}$ milled seeds $^{**)}$ Batch 5

For the first experiment, milled seeds were used in order to guarantee fast crystallization during the initial testing of the process. In Figure 5.34, mass fractions and supersaturation levels are shown for each crystallizer. Tank 1 was operated below the saturation temperature and was seeded with L-Thr (E1) at t = 0 h. Tank 2 initially contained a saturated racemic suspension. Although Tank 1 shows a similar concentration profile as conventional PC, we immediately notice three inflection points, which are marked by the vertical dashed lines. The mass distributions of L- and D-Thr across the liquid and solid phases at these specific points are qualitatively illustrated in Figure 5.35.

In Figure 5.34, we see an initial sharp drop of the concentration of L-Thr (E1) in Tank 1 between t_0 (t = 0 h) and t_1 as a result of the fast crystallization of the milled seeds. A temporary plateau is reached because of the simultaneous selective dissolution of E1 from the racemic solid in Tank 2. As L-Thr crystallizes a transient undersaturation is created in the second crystallizer due to the exchange of solution. Up to t_1 the concentration of L-Thr does not change noticeably in Tank 2 since its selective dissolution immediately counter balances the drop caused by the preferential crystallization in Tank 1. This is also reflected by the level of supersaturation in Tank 2, which remains close to $S_{E1} = 1$. The same should apply to the crystallization Tank 1 during this period as suggested by the illustration in Figure 5.35 at t_1, however, the exchange rate of $F_{ex} = 20$ mL/min is not high enough, which causes a delayed equilibration of the two liquids and thus a drop in concentration. The supersaturation of D-Thr in Tank 2 is completely unaffected for the first 4.5 h of the process and remains at the initial value of $S_{E2} = 1$.

After t_1, the solid phase in Tank 2 only contains D-Thr. Crystallization of L-Thr is now maintained entirely by the excess that is still dissolved in the liquid phase in Tank 1. This results in the further decrease of the concentration in both vessels until it reaches equilibrium in Tank 1 after approximately 4 h. The inflection point of the concentration of D-Thr, w_{E2L}, at t_2 in Tank 1 indicates nucleation of the unseeded enantiomer D-Thr in this crystallizer.

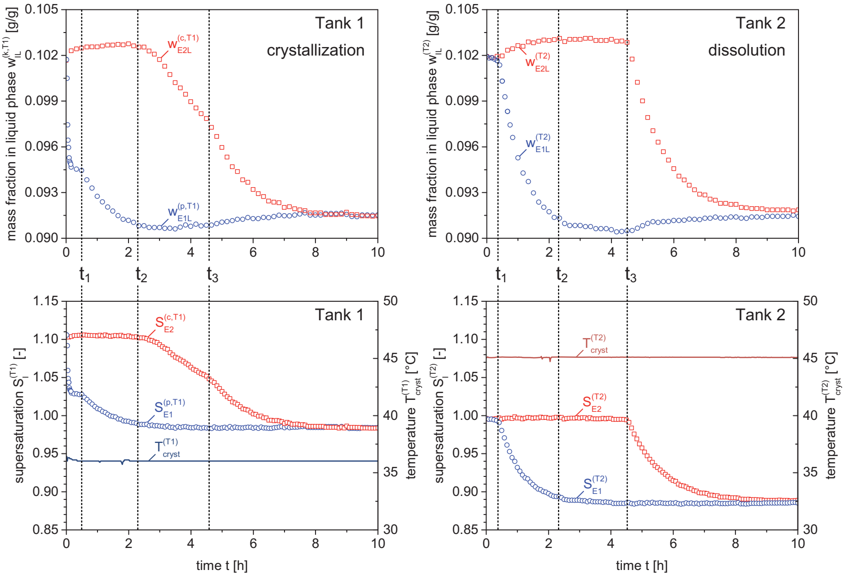

Figure 5.34: Mass fraction, w_{IL}, and supersaturation, S_I, in both crystallizers showing the full dynamics until equilibrium during the first coupled preferential crystallization-dissolution experiment CPC-D1. L-Thr (E1) is indicated by red circles, D-Thr (E2) by blue squares.

Between t_2 and t_3 it is dissolved from the remaining solid in Tank 2 in the same way L-Thr was dissolved from the racemate in the beginning of the process. Until t_3 the dissolution perfectly counter balances the crystallization of D-Thr, which we can see by the stable concentration in Tank 2. The decreasing concentration in Tank 1 is again the result of the rather slow exchange of solution between both crystallizers. Point t_3 marks the complete dissolution of D-Thr in Tank 2. It continues to crystallize in Tank 1 until the equilibrium concentration at the specific temperature of 36 °C is reached. After approximately 10 h the process is complete (t_∞ in Figure 5.35). The solid phase in Tank 2 has been entirely dissolved and transferred to the solid phase in Tank 1. The solution in Tank 2 is now undersaturated at the present temperature of 45 °C with respect to both enantiomers. In order to obtain pure product in Tank 1, the process must be stopped before nucleation of D-Thr, i.e. just before t_2. If pure product in Tank 2 is also a requirement, we have to ensure that L-Thr is completely dissolved from the racemic solid before D-Thr nucleates in Tank 1.

The subsequent two experiments in Figure 5.36 were stopped after 3 h and 2.5 h, respectively, to analyze the solid phase of each crystallizer. Since the conditions were different from CPC-D1 – in particular because of the larger seeds (Batch 5) – it was not known in advance at what time nucleation or complete selective dissolution would occur.

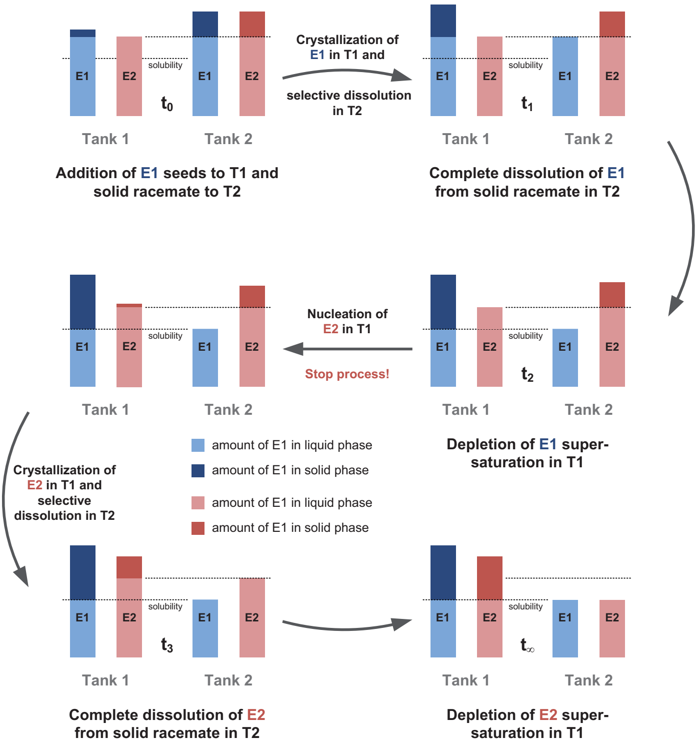
E1
E2
solubility
t0
E1
E2
Tank 1
Tank 2
Addition of E1 seeds to T1 and solid racemate to T2
Crystallization of E1 in T1 and
selective dissolution in T2
E1
E2
solubility
t1
E1
E2
Tank 1
Tank 2
Complete dissolution of E1 from solid racemate in T2
E1
E2
solubility
E1
E2
Tank 1
Tank 2
Nucleation of E2 in T1
Stop process!
E1
E2
solubility
t2
E1
E2
Tank 1
Tank 2
Depletion of E1 super-saturation in T1
Crystallization of E2 in T1 and selective dissolution in T2
🟦 amount of E1 in liquid phase
🟦 amount of E1 in solid phase
🟥 amount of E1 in liquid phase
🟥 amount of E1 in solid phase
E1
E2
solubility
t3
E1
E2
Tank 1
Tank 2
Complete dissolution of E2 from solid racemate in T2
E1
E2
solubility
t∞
E1
E2
Tank 1
Tank 2
Depletion of E2 super-saturation in T1

Figure 5.35: Schematic illustration of the liquid and solid phase repartitioning during the coupled preferential crystallization-dissolution experiment CPC-D1.

Therefore, the processes were stopped shortly after one of the inflection points (t_1 or t_2 in Figure 5.34) were identified in the concentration signals. Figure 5.36 shows the measured concentrations in each crystallizer for both experiments, CPC-D2 and CPC-D3. Because of the larger L-Thr seeds and the expected slower rate of crystallization in Tank 1, it was decided to lower the volumetric exchange rate to F_{ex} = 11 mL/min to more effectively avoid blockage of the filters, which was a frequent source of disturbances during the previous CPC experiments. Given the liquid volume of 450 mL in each crystallizer, the solutions were completely exchanged approximately every 40 min. During CPC-D2 (Figure 5.36a) the concentration of seeded L-Thr, w_{E1L}, in Tank 1, represented by solid blue circles, decreased slowly after an initial drop. For the first two hours of the process, the selective dissolution of L-Thr in Tank 2 (open blue circles) provided solution with a constant concentration to Tank 1. After 2.3 h, we can see a noticeable drop of the concentration of L-Thr in Tank 2, which indicates its quantitative dissolution from the initial solid racemate. This is also reflected by the increasing rate at which the concentration of L-Thr decreases in Tank 1 shortly afterwards. The process was operated for another 40 min; however, after 2.5 h the decrease of the concentration of D-Thr, w_{E2L} (solid red squares), suggests that nucleation occurred in Tank 1. This is also supported by the purity given in Table 5.21.

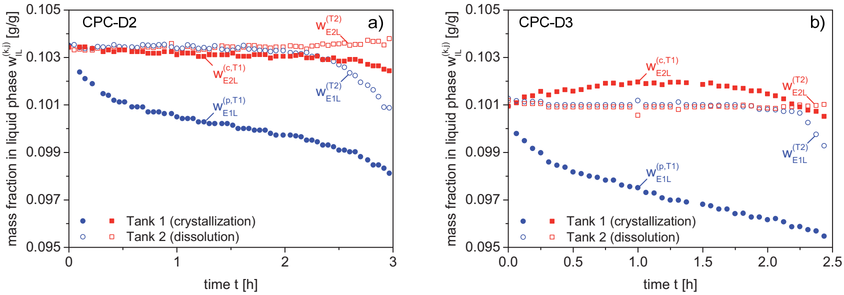

Figure 5.36: Mass fractions from two coupled preferential crystallization-dissolution experiments, CPC-D2 (a) and CPC-D3 (b). Solid symbols are measurements from the crystallization Tank 1, open symbols from the dissolution Tank 2.

In the last experiment, CPC-D3 (Figure 5.36b), the racemic solutions were prepared using purchased D- and L-Thr material. The concentration was identical to that of the isothermal benchmark experiments PC1 and CPC1. The point at which the selective dissolution of L-Thr from the racemic suspension in Tank 2 was completed can be clearly seen by the drop of the concentration w_{E1L}, represented by open circles in Figure 5.36b. However, the concentration of D-Thr in Tank 1 suggests that nucleation occurred earlier than during CPC-D2, i.e. after approximately 1.5 h. The purity of L-Thr, obtained from the crystallization vessel (Table 5.21) is slightly lower, which supports this observation.

Regarding the recovery of the solid material added to the crystallizers at the beginning of the processes (2 g of L-Thr seeds in Tank 1, 20 g of racemate in Tank 2), we notice that the sum of the product masses from both experiments is approximately 20 g. Ideally, we would expect 12 g of pure L-Thr in Tank 1 and 10 g of pure D-Thr in Tank 2. In addition, the L-Thr seeds also partly depleted the liquid phase as we can see by the decrease in concentration. As a result, the product mass in the crystallization vessel should be even higher. The discrepancy between the measured and the expected masses can be attributed to losses during the filtration and washing but also to inaccuracies of the solubility correlation (eq. (4.1)), which was used to calculate the initial solution concentrations.

Table 5.21: Results of the product analysis of experiments CPC-D2 and CPC-D3, stopped after 3 h and 2.5 h, respectively.

	Tank 1 (crystallization)			*Tank 2 (dissolution)*		
experiment	*product mass [g]*	*purity (L-Thr) [%]*	*productivity [g/(kg h)]*	*product mass [g]*	*purity (D-Thr) [%]*	*productivity [g/(kg h)]*
CPC-D2	9.6	96.6	32.4	9.7	98.0	41.3
CPC-D3	13.8	95.3	62.7	6.2	98.8	30.3

The main advantage of this process concept is that both enantiomers can be obtained as pure crystals using only one type of homochiral seeds as opposed to CPC. Obviously, however, the process must be stopped before nucleation of the unseeded enantiomer occurs in the crystallization tank. During experiment CPC-D1 this could be easily identified by the inflection point in the concentration measurement at t_2. At very high exchange flow rates, however, it could be difficult to detect the nucleation event in Tank 1. In case of ideal mixing of the two solutions, the selective dissolution in Tank 2 would also immediately counter balance the drop in concentration in Tank 1.

Another aspect is the chronological order of complete selective dissolution of L-Thr (t_1) and the onset of nucleation of D-Thr (t_2) (Figure 5.35). In the above experiment the very fast crystallization of the milled seeds was advantageous for the process since the racemic solid in Tank 2 was cleared of L-Thr before nucleation occurred in Tank 1. As a consequence, both enantiomers could have been obtained in pure form had the process been stopped at t_1. Under the specific conditions of CPC-D1, pure L-Thr could have been obtained even until t_2, which would have resulted in a further increase of the product mass in Tank 1 due to the additional depletion of the supersaturated liquid phase. It is however possible that the onset of nucleation in Tank 1 occurs earlier. In that case pure enantiomer can only be obtained in Tank 2. The order at which complete dissolution of L-Thr in Tank 2 and nucleation of D-Thr in Tank 1 occur depends on the combination of the following process parameters:

- degree of supersaturation in Tank 1
- seed size and loading
- rate of crystallization in Tank 1
- mass of solid racemate in Tank 2
- volumetric exchange flow rate
- temperature difference between both crystallizers

The implications of some of these parameters on the process will be analyzed in more detail in chapter 5.7.2 using the process model and the estimated kinetic parameter values presented in this work.

The coupling of preferential crystallization with selective dissolution presents an option to drastically increase the productivity of a conventional PC process by the addition of a second crystallizer, which provides a continuous stream of solution with constant concentration. It is therefore possible to maintain an almost constant driving force for crystallization of the preferred enantiomer and thus obtain much higher yields. At the same time, the concentration of the unseeded enantiomer is not increased, thus the induction time for its nucleation is not significantly reduced.

This process concept additionally presents another very robust option, namely the possibility to produce pure enantiomer by selective dissolution rather than by crystallization. Since the solution in one tank remains saturated, nucleation is impossible. Thus we can preferentially crystallize the unwanted enantiomer and selectively dissolve it from the racemic solid phase. Once this is complete, the purified solid phase will retain its purity. In the worst case it will start to dissolve due to nucleation in the crystallization tank but purity will not be affected.

5.6 Conclusions and comparison of conventional and improved process strategies

In this chapter we summarize all processes discussed so far and evaluate them in terms of their productivities. Figure 5.37 gives a more general overview of how the different process options and conditions influenced the performance of preferential crystallization. Therefore, the productivities Pr_I (eq. 4.13) of each experiment are plotted against the increase in product mass ($\Delta m_{IS} = m_{IS}(t_{stop}) - m_{Iseeds}$). The left figure shows results for L-Thr (E1), the right those for D-Thr (E2) obtained from Tanks 1 and 2, respectively. The majority of the data stems from the coupled processes (CPC), which are labeled according to the specific process option. Results from the conventional batch processes (PC) are shown only in Figure 5.37a, in the bottom left corner of the diagram. Coupled preferential crystallization-dissolution (CPC-D) is represented by two experiment. Red symbols are used in all cases where product purity was below 98%.

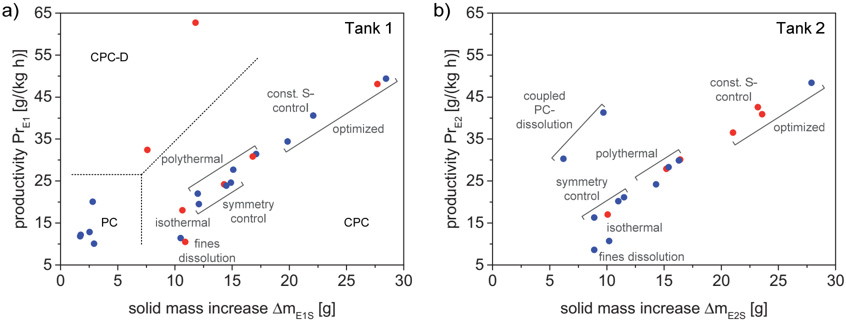

Figure 5.37: Comparison of the productivities Pr_I and the increase in product mass Δm_{IS} obtained from the conventional PC, coupled PC and coupled PC-dissolution experiments. In the lower left corner, results of the conventional process are shown (cf. Figure 5.13a). Red dots signify that the product purity was below 98%. Results in Tank 1 (a) are for L-Thr, in Tank 2 (b) for D-Thr.

Generally we can see that the coupled processes (CPC) have a great potential to be further improved by polythermal operation. Although they are not necessarily more productive than conventional PC when operated under isothermal conditions they always yield higher product masses. Among the polythermal CPC experiments, the optimized clearly stand out in terms of yield and productivity. It is interesting to see that constant supersaturation control results in a similar performance. The third process strategy, which combines PC with selective dissolution (CPC-D), was shown to be capable of very high productivities. The preliminary experiments even outperformed the optimized CPC process, although we have to consider that productivity was not the objective of the optimization.

The isolated group of conventional batch experiments (PC) in Figure 5.37a contains an additional experiment, with a productivity of Pr_{E1} = 20 g/(kg h) not mentioned so far, for which 2 g of milled seeds were used. It was operated at a temperature of 36 °C starting from the same initial solution as all other experiments in terms of concentration. The purpose was to show the impact of the seed crystal size. The productivity is comparable to some of the polythermal coupled experiments and it should be mentioned that by providing such a high initial crystal surface area of the preferred enantiomer, the conventional batch process can be very productive and possibly yield even higher amounts of pure product. However, it will always be outperformed by coupled preferential crystallization under identical conditions. The major advantage of CPC in comparison to conventional PC and CPC-D remains that – given the right operating conditions – it is only limited by thermodynamics not by kinetics. Because of this, CPC can be operated far more dynamically and is thus apt for optimization and control strategies that make extensive use of temperature variations to increase productivity and yield.

This completes the experimental investigation of three process strategies to obtain pure enantiomers from a conglomerate forming system by preferential crystallization. In the following chapter we will return to the process model to identify general trends and limits of the discussed processes.

5.7 Results of complementary simulation studies

The experimental work discussed in previous chapters was the basis for adjusting the model so that it would be capable of reproducing a wide range of operating conditions but also different process concepts. Over the course of this work it became apparent that the latter task is still difficult as each process strategy seems to exhibit specific phenomena. An accurate simulation of conventional and coupled preferential crystallization already required two different sets of kinetic parameter values. Coupled preferential crystallization with selective dissolution is therefore a good process to test the model.

The following simulation studies were done with the model described in chapter 3.1 using the kinetic parameters found optimal for coupled preferential crystallization (see Table 5.2, CPC) and further investigate the three process strategies on a theoretical basis. This allows us to screen a variety of different process conditions and generate a comprehensive understanding of where each process concept is optimal and where the limits are in terms of robustness (i.e. nucleation) and productivity.

5.7.1 Limits of conventional and coupled preferential crystallization

The amount of pure enantiomer that can be obtained by conventional PC is strongly limited by the induction time of nucleation. Under certain, unfavorable conditions, this also applies to coupled preferential crystallization. In the following, we will investigate these two process strategies under different operating conditions with the help of predictions made by the model. The most important process variable will be the initial temperature and thus the degree of supersaturation.

Figure 5.38 shows an illustrative simulation of the isothermal benchmark experiment PC1 using the parameters optimal for CPC (Table 5.2, chapter 5.1.1). Next to the concentration in the liquid phase (a), the predicted evolution of the solid phase (b) is shown. Although the simulation does not exactly follow the trend of the unseeded enantiomer E2, we will use this set of kinetic parameter values for all subsequent simulations. For a separation to be considered successful, the product purity must be at least 98%. The point in time at which this criterion is still fulfilled is labeled t_{98} in Figure 5.38. It will also be referred to as the induction time of nucleation. The process depicted in Figure 5.38 was simulated at a temperature of 30 °C with initial conditions summarized in Table 4.3. In the subsequent simulations, we will investigate how the location of t_{98} and the relative product yield at this point, $Y_{E1}(t_{98})$, are influenced by the degree of initial supercooling ΔT_0. The relative yield was calculated with eq. (4.11) using the mass obtained after the process duration t_{98} ($m_{E1S}(t_{98})$ in Figure 5.38b) and is a measure that shows how close the process has come to thermodynamic equilibrium.

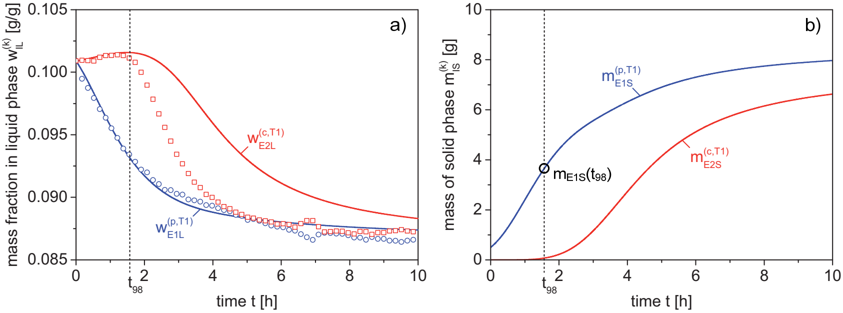

Figure 5.38: Simulation of the benchmark experiment PC1 using the parameters optimal for coupled PC (Table 5.2). a) mass fractions w_{IL} in the liquid phase, b) simulated masses m_{IS} of the solid phase. t_{98} indicates the point where the product (E1) has a purity of 98%, i.e. the induction time of nucleation.

We will first evaluate conventional preferential crystallization subjected to different degrees of initial supercooling $\Delta T_0 = T_{sat,0} - T_{cryst}$. Except for temperature all other conditions were constant (see Table 4.3).The initial solutions were saturated at $T_{sat,0} = 43.7$°C.

Figure 5.39a shows the change of the relative yield $Y_{E1}(t_{98})$ and shifting of the induction time t_{98} at varying crystallization temperatures T_{cryst} for conventional PC. With temperature T_{cryst} decreasing from 35 °C to 20 °C (Figure 5.39a), the model predicts a decrease of the induction time t_{98} (squares) during which pure enantiomer can be produced. This is due to the increasing driving force making nucleation more likely. With shorter available process times t_{98}, the relative yield $Y_{E1}(t_{98})$ (circles) decreases as well although the driving force for crystal growth is higher. In addition to shorter available process times all kinetics are affected by the temperature dependencies contained in the model resulting in a reduction of crystallization rates.

Below 20 °C the model predicts a slight increase of t_{98}, which seems counter intuitive. We would assume that the induction time for nucleation becomes shorter as the driving force is further increased. The current model predicts that below a certain temperature, the influence of supersaturation on the rate of primary nucleation is outweighed by the temperature dependency, which slows kinetics and in turn prolongs the induction time t_{98}. The effect is minor and would be very difficult to confirm experimentally. However, measurements reported by Polenske (2010) and Lorenz, et al. (2006), show a broadening of the metastable zone width of threonine with decreasing temperature suggesting a retardation of primary nucleation at lower temperatures.

Generally, the model predicts that it is possible to operate conventional PC over the entire simulated temperature range. We have to consider, though, that at T_{cryst} = 10 °C, the initial degree of supercooling amounts to ΔT = 33 K under the set conditions, which is far outside the reported the metastable zone width of threonine. It is thus unlikely to be experimentally feasible. Conventional PC of threonine was, however, not investigated at such low temperatures. Therefore, it cannot be entirely excluded that the predictions are correct. In the publication Eicke, et al. (2013) it was reported that a racemic threonine solution, saturated at 40 °C can be readily subcooled by ΔT = 20 K without an onset of nucleation for at least 1.5 h (see also Appendix 7.3). This suggests that the process could be performed even at such high levels of supersaturation. Below 20 °C the model predictions should however be treated with care.

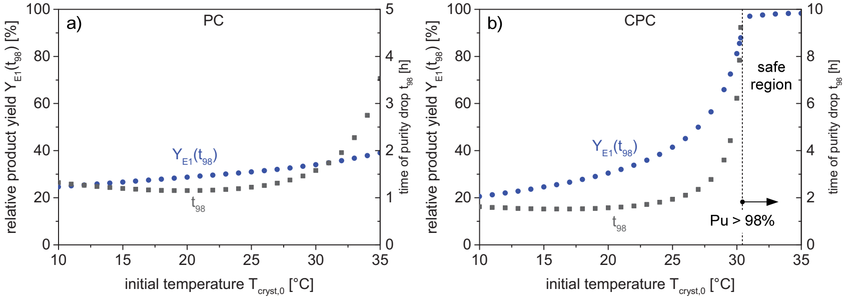

Figure 5.39: Comparison of conventional PC (a) and CPC (b). Predicted relative product yields Y_{E1} obtained after t_{98} are indicated by circles. The points in time t_{98} where the product still has a purity of 98% are represented by squares. In all cases the initial solution was saturated at T_{sat} = 43.7 °C.

The theoretical study was repeated under identical conditions (concentration, mass and size of seeds) for coupled preferential crystallization with an exchange flow rate of F_{ex} = 50 mL/min; the results are shown in Figure 5.39b for only one tank, since the simulated process was perfectly symmetric. Even though the two enantiomers crystallize in two separate vessels, nucleation can still occur, which was also shown for some of the experiments done in this work. The model predicts significant nucleation below $T_{cryst,0}$ = 30.5 °C. Above this temperature, the CPC process is only limited by thermodynamics and always yields product with purities above 98%. Therefore, the indication of t_{98} is obsolete for this region because the process can be operated until equilibrium is reached. Similar to the PC process, the induction time t_{98} decreases towards lower temperatures but remains at higher values. The relative yield $Y_{E1}(t_{98})$ increases significantly stronger, as the initial degree of supercooling is reduced, and approaches 100% above 30.5°C. This clearly shows the main advantage of the coupled process over conventional PC. In general, CPC exhibits a process regime (here for temperatures above 30.5°C), were nucleation can be completely avoided, which is not possible in the conventional case.

In the simulations, the point t_{98} was defined as the end of the process at which the product is obtained. Although the maximum possible process duration (t_{98}) and the *relative* yield decrease as we approach 10 °C, the *absolute* yield, i.e. the product mass $m_{E1S}(t_{98})$ still increases during conventional PC. As a consequence, the process becomes more productive. A plot comparing the productivities of PC and CPC at the investigated initial temperatures is shown in Figure 5.40. The conventional case (PC) exhibits a slight maximum around 12 °C, which is caused by the temperature dependencies of the kinetics. Below 20 °C, however, the model predictions have to be evaluated critically in light of the projected increase of the induction time t_{98}, which seems implausible.

As expected and confirmed by the experimental results in chapter 5.3.2 (Figure 5.16b), the CPC process shows much higher productivities, especially in the "unsafe" region below 30.5 °C. Above this temperature, the productivities of CPC (bold circles) are misleading as they suggest almost no benefit. This trend is merely coincidental. The points correspond to the productivity after the maximum simulation time of 10 h. Naturally, an isothermal process becomes less productive as it approaches equilibrium (see Figure 5.16b). As a consequence, such a coupled process would not be operated until equilibrium when productivity is the main performance criterion. For illustrative purposes, the open circles show the productivity, when the process is stopped after 5 h.

The model predictions showed that CPC can be operated under conditions where nucleation does not occur. Although the productivity is much lower in the safe operating window under isothermal conditions, it is readily possible to increase it by further cooling when the process is started within this region. Such options are – if at all – not easily applicable for the conventional case.

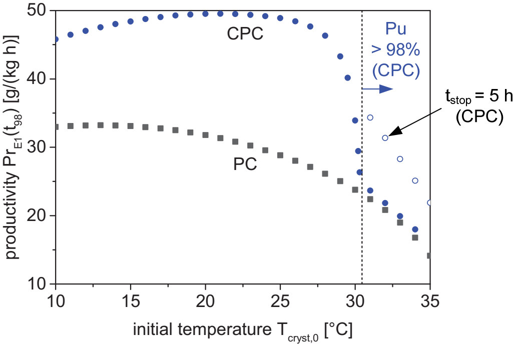

Figure 5.40: Comparison of the productivities of conventional and coupled PC. Under the specific process conditions (concentration, mass and size of seeds, exchange flow rate), CPC can be operated safely above 30.5 °C.

We have to remember that the theoretical investigation presented above was done under specific process conditions. Naturally, each process strategy (PC, CPC) can be further improved by changing, e.g. the mass or size of the seeds. With a larger surface area, and thus faster desupersaturation of the liquid phase, conventional preferential crystallization will become more productive and the relative yield will be higher. Coupled preferential crystallization would additionally benefit in terms of the safe regime as the location of its border also depends on the surface area of the seeds. With a faster decrease in concentration regarding both enantiomers, nucleation of the unseeded species in each crystallizer becomes less likely. As a consequence, the safe region will shift towards lower temperatures. In order to keep this investigation concise, the impact of the seed surface area is not further investigated.

An important aspect is the influence of the exchange flow rate F_{ex} on the performance of CPC. The previous simulations were therefore repeated for different flow rates. Figure 5.41 shows how the induction time t_{98} (a) and the relative product yield Y_{E1} (b) evolve under different temperatures and flow rates. Again, only results from one crystallizer are shown.

The safe regions are located in the rightmost quarter of each plot represented in red. For F_{ex} = 0 mL/min, the process is identical to conventional PC and we can see that no safe region exists for the investigated temperature range. With increasing flow rate, the operating window becomes wider and extents to approximately 30 °C.

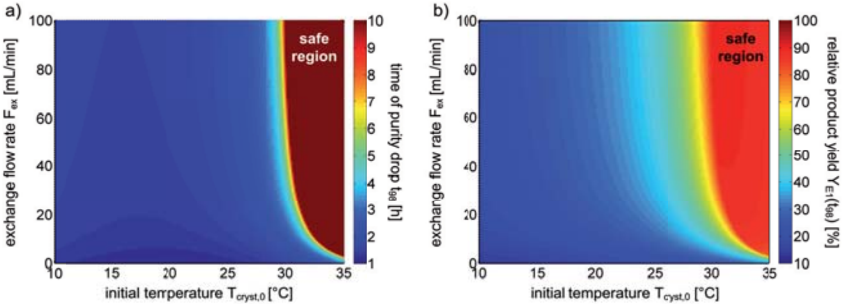

Figure 5.41: Influence of the exchange flow rate F_{ex} at different initial temperatures on the process time t_{98} (a) and the relative yield Y_{E1} (b) for CPC. The red areas on the right side of each plot indicate operating conditions under which CPC completely avoids nucleation of the unseeded enantiomers. Results are for Tank 1 only due to perfect symmetry.

Assuming that the model is accurate enough we can also see that the flow rate of F_{ex} = 50 mL/min chosen for the experiments was reasonably high. The benefit does not improve significantly above this value. In addition, this theoretical study showed that most of the coupled experiments were operated with initial conditions that are right at the border of the safe region. This was already suggested at the end of chapter 5.4.3 and is now supported by the model. Although the results obtained from this simulation study are specific for threonine, the author believes that other conglomerate forming systems will also exhibit a region, where a potential CPC process is only limited by thermodynamics.

5.7.2 Limits of coupled preferential crystallization with selective dissolution

The combination of preferential crystallization and selective dissolution is a suitable process to validate the model described in chapter 3.1. From the experiments in chapter 5.5 we know the dynamics of the liquid phase and were able to appoint different stages of the process to events taking place in the solid phase. We will now use the model to confirm the assumed relationships.

Figure 5.42 shows a simulation of experiment CPC-D1 using the model parameters found optimal for CPC (Table 5.2). The agreement between the simulated and measured concentrations in the liquid phase, w_{IL}, is acceptable considering that the model was adjusted using a different type of process. Chapter 5.1.1 already showed that two different kinetic parameter sets are needed to accurately simulate the process strategies PC and CPC, respectively. Since CPC-D is yet another kind of process a third set is apparently necessary. In the publication Eicke, et al. (2013) a slightly different model was used and calibrated specifically with experiment CPC-D1 resulting in a very good fit. However, nucleation kinetics therein assumed a fixed induction time and did not include a temperature dependency as opposed to the model used in this work.

Generally, the simulation in Figure 5.42a,b shows the same inflection points in the liquid concentrations, although slightly shifted in time. They clearly correspond with the complete dissolution of the crystallizing enantiomer E1 from the racemate in Tank 2 (t_{diss}, Figure 5.42d) and the onset of nucleation of the unseeded enantiomer E2 in Tank 1 (t_{nuc}, Figure 5.42c). The third inflection point in the concentration w_{E2L} obviously marks the complete dissolution of the nucleated enantiomer in Tank 2 after 4 h. The fact that these points do not coincide with the experimental observation suggests that the initial mass of solid racemate in Tank 2 was less than the actually added mass (Table 5.20, CPC-D1). A certain amount apparently dissolved during the preparation. This may be due to impurities of the purchased racemic threonine that affected the solubility.

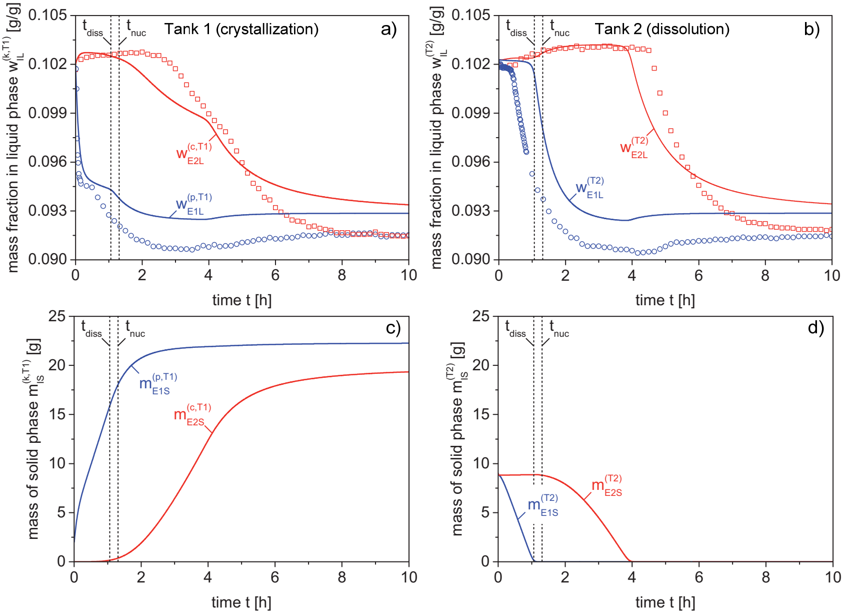

Figure 5.42: Simulation of CPC-D1 using model parameters optimal for coupled preferential crystallization (see Table 5.2). a,b) Experimental and simulated evolution of the liquid phases. c,d) Predicted trends of the solid phase. The point at which the seeded enantiomer E1 is dissolved from the solid racemate in Tank 2 is labeled t_{diss}. The onset of nucleation of E2 in Tank 1 is labeled t_{nuc}.

In chapter 5.5 we concluded that the dynamics of the CPC-D process, specifically the location of t_{diss} and t_{nuc}, depend on a number of process conditions, i.e. the degree of supersaturation in Tank 1, seed size and loading, temperature in Tank 2, mass of solid racemate and the volumetric exchange flow rate. The combination of these process parameters results in distinct operating regions where the process yields two pure enantiomers. Some were already studied in Eicke, et al. (2013), however without variations of temperature. In order to complement the published investigation, we will particularly look at the influence of the crystallization temperature T_{cryst} in Tank 1.

The initial solutions were all saturated at T_{sat} = 43.7 °C (eq. (3.1)) with dissolved masses of E1 and E2 identical to experiment CPC-D3 (Table 5.20). Additionally, two different exchange rates F_{ex} as well as two seed mean sizes were investigated. The performance of each crystallizer was evaluated using the product of productivity (eq. (4.13)) and enantiomeric excess in the solid phase (eq. (4.15)), $Pr_I \cdot ee_j$. Figure 5.43 shows the performance measure as a function of temperature and time (notice the different scaling).

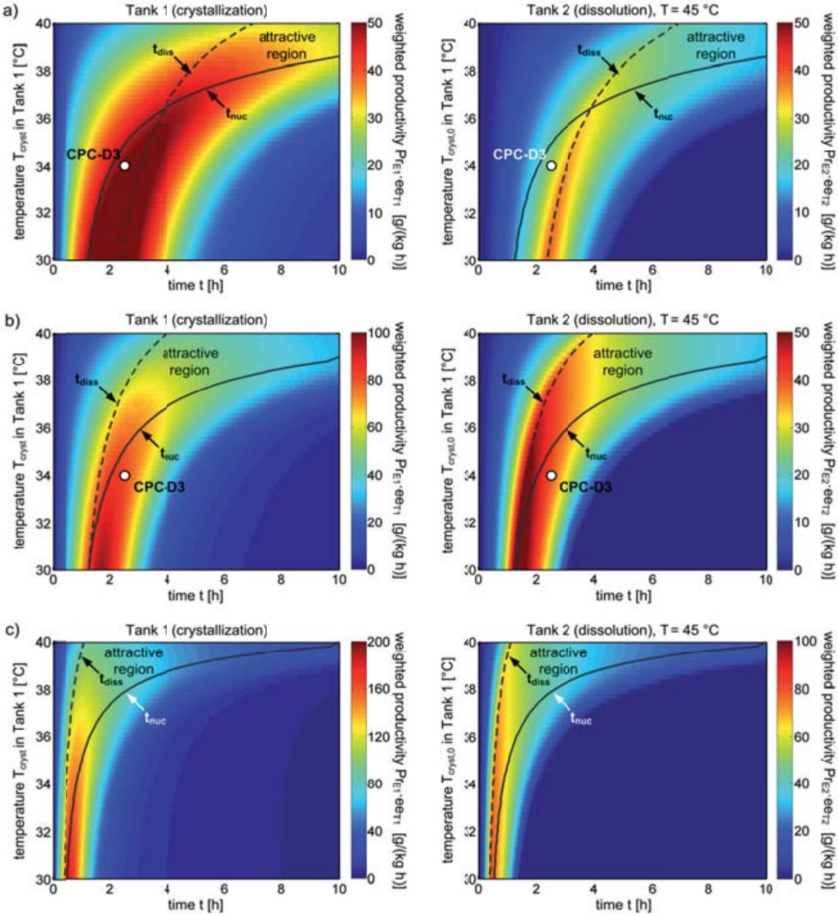

Figure 5.43: Parametric simulation study of CPC-D at various crystallization temperatures in Tank 1. Additionally, the exchange rate F_{ex} as well as the seed size were changed. The conditions were as follows. a) F_{ex} = 11 mL/min, $m_{E1seeds}$ = 2 g (Batch 5); b) F_{ex} = 50 mL/min, $m_{E1seeds}$ = 2 g (Batch 5); c) F_{ex} = 50 mL/min, $m_{E1seeds}$ = 2 g (milled, z_{mean} = 50 µm). The initial solutions were all saturated at $T_{sat,0}$ = 43.7 °C. The mass of solid racemate in Tank 2 was m_{racS} = 20 g. Tank 1 was seeded with 2 g of L-Thr (E1). Within the attractive region, pure enantiomer can be obtained from both tanks.

The dashed curves represent point t_{diss}, at which the seeded enantiomer E1 (L-Thr) has been dissolved from the racemate in Tank 2, i.e. the purity of E2 (D-Thr) has reached 98%. The solid lines indicate t_{nuc}, i.e. the point, at which the purity of E1 in Tank 1 has dropped to 98% due to the onset of nucleation.

The first set of simulations (Figure 5.43a) was done according to the conditions of experiment CPC-D3 at an exchange rate of F_{ex} = 11 mL/min. The circle marks the position of this experiment. According to the model predictions, the chosen process conditions were not favorable as it lies outside the attractive region were both pure enantiomers can be obtained. This is in accordance with the measured product purities given in Table 5.21 suggesting that nucleation in Tank 1 occurred before L-Thr was completely dissolved from the racemate in Tank 2. Generally, the attractive region is enclosed by t_{diss} and t_{nuc} in this specific order.

The simulation in Figure 5.43b illustrates the effect of a higher exchange rate, here F_{ex} = 50 mL/min. The position of t_{nuc} is not significantly changed; however, the point at which the racemate in Tank 2 is purified moves towards the beginning of the process. As a result, the attractive region becomes much wider and productivities increase. Even at lower crystallization temperatures the process is far more productive than the previous one with F_{ex} = 11 mL/min. At lower exchange rates, mass transfer between the crystallizers is limited and the drop in concentration caused by crystallization in Tank 1 cannot be immediately counterbalanced by selective dissolution in Tank 2.

In Figure 5.43c we see the influence of a higher seed surface area. The same mass of seeds was added to Tank 1, however, with mean size z_{mean} = 50 µm as opposed to 350 µm. All other conditions were kept constant, i.e. F_{ex} = 50 mL/min. As expected, productivity is significantly higher and the attractive region now extents to the lowest investigated temperature of 30 °C, which is equivalent to an initial supercooling of ΔT = 13.7 K. Furthermore, the model predicts a shorter induction time t_{nuc} resulting from the dependence of the nucleation kinetics on the second moment (eq. (3.23)). Experimental studies are, however, required to clarify if this effect is reasonable.

The theoretical study showed how varying temperature differences between the crystallization and dissolution tanks affect the process performance and revealed optimal operating regions. Generally, fast exchange rates and high seed surface areas are most beneficial and show the strongest influence. Due to the higher mass transfer to the solid phase in the crystallization tank, coupled preferential crystallization and selective dissolution can potentially be more productive than standard coupled preferential crystallization.

5.7.3 Conclusions from the simulation studies

The simulations discussed in the previous two chapters provide a broader understanding of the investigated process strategies and allow qualitative extrapolation of process performances when operating conditions are changed. Naturally, we have to accept that the simplified process description only approximates the complex phenomena taking place during crystallization and many technically related effects. Nucleation remains the biggest challenge therein but a full understanding is not the main goal of engineering research. Apart from temperature and supersaturation, it might be sufficient to systematically study the influence of additional process variables on induction time and nucleation rate, e.g. seed loading, suspension density, degree of agitation, and use simple empirical correlations. A successful example is the description of crystal growth kinetics, which was sufficiently accurate for threonine. Improvements can also be gained by considering the crystal shape in a simplified way. In this work, a fixed length-to-width ratio was assumed, which is not supported by the data presented in Appendix 7.9. Such easily accessible observations should be included in future works.

The current model is already sufficiently accurate and capable of predicting the dynamics of the studied process strategies. Together with the knowledge of favorable operating regions it is a valuable additional resource for future process design with new substance systems.

6 Conclusions

In this work, three different process concepts were investigated that can be applied to separate the enantiomers of the conglomerate forming system DL-threonine/H_2O by preferential crystallization. An overview of the studied processes is shown in Figure 6.1. The simplest implementation, termed conventional preferential crystallization (PC), was used as a starting point from where the separation process was successively improved. The major part of this work was devoted to coupled preferential crystallization (CPC), which exploits the benefits of connecting two crystallizers via the liquid phase. This concept was finally used to study the third option denoted coupled preferential crystallization with selective dissolution (CPC-D), where both crystallizers were operated at different temperatures.

Some of the results obtained from PC and CPC experiments were used to improve the predictive capabilities of a mathematical process model by performing a detailed parameter estimation. The model was based on one-dimensional population balance equations and was used to theoretically investigate the three process concepts under different operating conditions. The experiments but also the simulations showed that the coupled process strategies CPC and CPC-D are clearly superior in comparison to conventional PC.

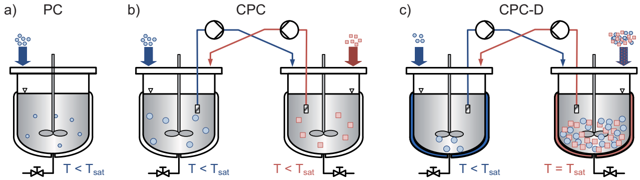

Figure 6.1: Process strategies for batch preferential crystallization investigated in this work.

Preferential crystallization has to be performed in a region where the initially racemic solution is metastable. Since the enantiomers have identical physico-chemical properties, their tendency to crystallize spontaneously from a supersaturated solution is equal. Within the metastable region, however, nucleation occurs only after an induction period, during which it is possible to selectively crystallize only one enantiomer by seeding. Thus conventional preferential crystallization has to be stopped at some point to avoid contamination of the solid product. The yield of enantiopure crystals and the overall performance is therefore strongly limited by kinetics. In this work, fines dissolution was shown to often be a feasible improvement of conventional PC, as it is capable of delaying the onset of nucleation by continuously dissolving the generated nuclei. This, however, was only possible to a certain extent under the chosen experimental conditions. Theoretically it could be possible to almost completely avoid nucleation with this technique; however, this would require significant energy inputs in the form of heating and liquid circulation. The application of fines dissolution was only briefly investigated in this work, although it has great potential for improvement, especially from a technical point of view. Some of the challenges encountered during the preliminary investigations could probably be easily resolved by a redesign of the fines dissolution unit.

Coupled preferential crystallization is perhaps the most robust option, in particular when both enantiomers have to be crystallized. Previous works had already shown the benefit of a solution exchange, which essentially mimics a racemization in the liquid phase. It had also been shown that polythermal operation is a feasible option to further enhance productivity. In this work an isothermal experiment was performed, which served as a benchmark for subsequent improvements. Parts of the studies on CPC were done in collaboration with Prof. Jörg Raisch at the Technical University, Berlin, whose group provided model based control strategies for preferential crystallization. The main focus of this collaboration was to investigate a control strategy that counteracts disturbances during a CPC process. It was generally agreed that it is beneficial for the coupled process when both vessels are synchronized in terms of the rate of crystallization of the seeded enantiomers. Only in that case, will the liquid phases remain racemic, which maximizes the driving forces for crystallization of the seeded enantiomers. The experiments could successfully demonstrate the application of such a symmetry control, which was tested under forced asymmetric initial conditions. Among the coupled experiments these controlled processes also showed some of the highest purities reached. At the same time it could also be shown that perfect symmetry is not entirely necessary for an effective separation. An uncontrolled asymmetric experiment showed no negative impact on the final product purities.

The second control strategy that was tested directly aimed at the productivity of CPC and involved the control of the level of supersaturation. Under isothermal conditions the driving force constantly decreases as supersaturation is depleted, which leads to a reduction in productivity. Polythermal operation using arbitrarily chosen linear cooling profiles was studied in this work as well. It was shown that the separation can easily fail when the degree of supersaturation is increased too rapidly. The application of the constant supersaturation controller resulted in significantly higher productivities, while product purities remained within an acceptable range. A slightly lower setpoint would have resulted in much higher purities. This control strategy was shown to be very effective in enhancing the productivity. Apart from this closed-loop control, the developed mathematical process model was used to calculate optimal temperature trajectories that maximized the product yield. It could be shown that the productivities obtained from the optimized processes were similar compared to those obtained with constant supersaturation control.

The third process strategy investigated in this work presents an option, with which it is possible to obtain both enantiomers, when only one is available in its pure form. By the time of this work it had not received much attention in the literature apart from having been mentioned in a patent description. Like the CPC process, it relies on the coupling of two crystallizers via the liquid phase. However, the conditions are deliberately asymmetric. One vessel is operated as a conventional PC process at lower temperature, while the other contains a saturated racemic suspension at higher temperature. The crystallization vessel is constantly fed with fresh racemic solution as the seeded enantiomer selectively dissolves from the racemate. Although this process can also suffer from nucleation of the unseeded molecule it is possible to operate it at a very moderate degree of supersaturation and still maintain a high productivity. As opposed to conventional PC, the liquid phase is not depleted with respect to the seeded enantiomer as long as the second tank contains solid material. Alternatively, it is possible to obtain the desired enantiomer directly from the racemic suspension by crystallizing the impurity. This is the most robust option since no nucleation can occur in the dissolution vessel. At the early stage of process development with limited access to pure enantiomer, CPC-D is thus an attractive option to generate a stock of seed material for subsequent production processes.

The experimental studies done in this work showed that the CPC-D process concept can exceed the productivity of CPC. However, in order to be truly productive the level of supersaturation has to be in a range where nucleation can eventually occur. In that sense, we can conclude that a robust and productive process is best achieved with CPC once both enantiomers are available. A theoretical analysis of CPC using the full process model and the kinetic parameters estimated in this work, showed that there is an operating region, where nucleation can be completely avoided. Once this region has been identified for a specific conglomerate forming system it is possible to design a very robust process, which yields high amounts of two pure enantiomers.

This work focused entirely on batch processes and showed that preferential crystallization of conglomerate forming systems can be strongly intensified. In binary crystallization processes polythermal operation is very common. Its application in a process to separate enantiomers is not straight forward because of the identical properties of the two molecules. A strong focus was put on polythermal CPC showing that it is then possible to significantly increase the performance.

The next step in the development of preferential crystallization based separation processes is the transition from batch to continuous operation. Towards the end of this work, studies were initiated that assessed the feasibility of a continuous operation of conventional PC and CPC. The results published in Galan, et al. (2015) already show that continuous CPC is an attractive option that seems to be capable of exceeding the productivity of an optimized batch. Nevertheless, for smaller amounts of specialty chemicals, batch preferential crystallization will remain the option mainly used. This work is a contribution that increased the understanding of this type of separation process and provided a basis, from which further improvements can be developed. The results obtained for threonine should be easy to transfer to other conglomerate forming chiral systems and also to other preferential crystallization processes.

7 Appendix

7.1 Experimental conditions of conventional and coupled PC experiments

Table 7.1: Process conditions of all conventional PC experiments.

Experiment	T_{cryst} *[°C]*	m_{seeds} *[g]*	*Seeds Batch No.*	N_{St} $[min^{-1}]$	m_{tot} *[g]*	$w_{IL0}(t=0)$ *[g/g]*	*Process duration [h]*	*Remarks*	*Name in lab journal*
PC1	30	1.0	1 (L-Thr)	300	450	0.1009	17.5	isothermal benchmark exp.	PC 10
PC1a	30	1.0	1 (L-Thr)	300	450	0.1009	1.2	repetition of PC1 with interruption	PC 11
PC1b	30	1.0	1 (L-Thr)	300	450	0.1009	1.2	repetition of PC1a	PC 12
PC-FD1	30	1.0	3 (L-Thr)	300	490	0.1009	14.5	isothermal with fines dissolution	PC 32
PC-FD1a	30	1.0	3 (L-Thr)	300	490	0.1009	2	repetition of PC-FD1 with interruption	PC 33
PC2	30	0.5	4 (L-Thr)	300	450	0.1009	25.5	repetition of PC1, different seeds	PC 31
PC2a	30	0.5	4 (L-Thr)	250	450	0.1009	24.4	repetition of PC2	PC 38
PC-FD2	30	0.5	4 (L-Thr)	250	490	0.1009	27.8	isothermal with fines dissolution	PC 39
PC-FD2a	[30, 22]	0.5	4 (L-Thr)	250	490	0.1009	3.9	repetition of PC-FD2	PC 42
PC3	30	2.0	3 (L-Thr)	250	450	0.1009	10	param. est.	PC 35
PC4	35	0.5	260*)	250	454.45	0.1009	10	param. est.	batch PC 02
PC5	[34, 29]	0.5	3 (L-Thr)	250	450	0.1009	10	param. est.	PC 27
PC6	[30, 22]	0.5	3 (L-Thr)	300	450	0.1009	11	param. est.	PC 34

Table 7.2: Process conditions of coupled preferential experiments.

Experiment	*T_{cryst} [°C]*	*m_{seeds} [g]*		*Seeds Batch No.*		*N_{St} [min^{-1}]*	*m_{tot} [g]*	*$w_{IL0}(t=0)$ [g/g]*	*Process duration [h]*	*Remarks*	*Name in lab journal*
		Tank 1	*Tank 2*	*Tank 1*	*Tank 2*						
CPC1	30	0.5	0.5	3 (L-Thr)	3 (D-Thr)	250	450	0.1009	19	isothermal benchmark exp., param. est.	CPC 03
CPC2	30	0.5	0.5	3 (L-Thr)	3 (D-Thr)	300	450	0.1009	11	repetition of CPC1	CPC 06
CPC-FD1	30	0.5	0.5	3 (L-Thr)	3 (D-Thr)	250	490	0.1009	19	isothermal with fines dissolution	CPC 04
CPC3	[30, 20]	0.5	0.5	3 (L-Thr)	3 (D-Thr)	300	450	0.1009	11	polythermal (stepwise linear)	CPC05
CPC4	[30, 10]	0.5	0.5	5 (L-Thr)	5 (D-Thr)	250	450	0.1009	10	polythermal (linear) param. est.	CPC 12
CPC5	[30, 20]	0.5	0.5	5 (L-Thr)	5 (D-Thr)	250	450	0.1009	10	polythermal (linear) param. est.	CPC 14
CPC6	[30, 20]	0.5	0.5	5 (L-Thr)	5 (D-Thr)	250	450	0.1009	10	polythermal (linear) param. est.	CPC 16
CPC7	[30, 10]	0.5	0.5	5 (L-Thr)	5 (D-Thr)	250	450	0.1009	10	polythermal (linear) param. est.	CPC 15
CPC8	30	2.0	0.5	3 (L-Thr)	3 (D-Thr)	250	450	0.1009	10	isothermal, uncontrolled	CPC 08
CPC9	controlled	2.0	0.5	3 (L-Thr)	3 (D-Thr)	250	450	0.1009	10	symmetry control	CPC 07
CPC10	controlled	2.0	0.5	3 (L-Thr)	3 (D-Thr)	250	450	0.1009	10	symmetry control	CPC 09
CPC11	controlled	0.5	0.5	5 (L-Thr)	5 (D-Thr)	250	450	0.1009	10	constant supersaturation control	CPC 17
CPC12	optimized	0.5	0.5	5 (L-Thr)	5 (D-Thr)	250	450	0.1009	10	optimized for 98% purity	CPC19
CPC12a	optimized	0.5	0.5	5 (L-Thr)	5 (D-Thr)	250	476.07	0.1009	10	repetition of CPC12	CPC20
CPC13	optimized	0.5	0.5	5 (L-Thr)	5 (D-Thr)	250	476.07	0.1009	10	optimized for 99.9% purity	CPC21
CPC14	optimized	0.5	0.5	milled (L-Thr)	milled (D-Thr)	250	476.07	0.1009	10	optimized for 99.9% purity	CPC22

7.2 Experimental conditions of coupled preferential crystallization with dissolution

Table 7.3: Experimental conditions of coupled preferential crystallization and selective dissolution (CPC-D).

Experiment	*T_{cryst} [°C]*		*m_{seeds} [g]*		*Seeds Batch No.*		*N_{St} [min^{-1}]*	*m_{tot} [g]*	*$w_{IL0}(t=0)$ [g/g]*	*Process duration [h]*	*Remarks*	*Name in lab journal*
	Tank 1	*Tank 2*	*Tank 1*	*Tank 2*	*Tank 1*	*Tank 2*						
CPC-D1	36	45	2	20	milled (L-Thr)	Racemate	250	450	0.1009	10	Full dynamics	CPCv 02
CPC-D2	34	44	2	20	5 (L-Thr)	Racemate	250	450	0.1009	3		CPC 06
CPC-D3	34	45	2	20	5 (L-Thr)	Racemate	250	490	0.1009	2.5		CPC 04

7.3 Metastable zone width measurements of threonine

The figure below shows results from metastable zone width measurements of L-Thr/H_2O (Figure 7.1a) and racemic DL-Thr/H_2O (Figure 7.1b) performed in the equipment used for the experiments discussed in this work. In Figure 7.1a, the influence of different cooling rates was investigated. Figure 7.1b shows the nucleation behavior for higher cooling rates, including the maximum possible.

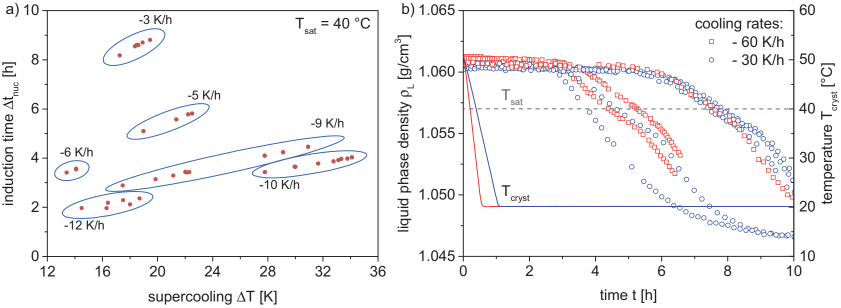

Figure 7.1: Nucleation behavior of threonine. a) Induction time of L-Thr/H_2O as a function of cooling rate and degree of supercooling. b) Nucleation of DL-/Thr/H_2O at two different cooling rates.

7.4 Seed crystal size distributions

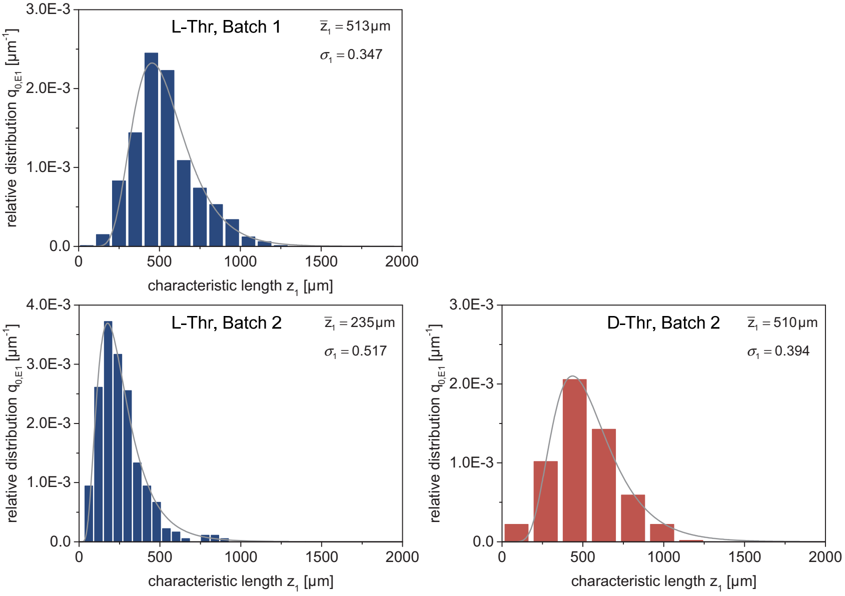

Figure 7.2: Seed crystal size distributions of batches 1 and 2.

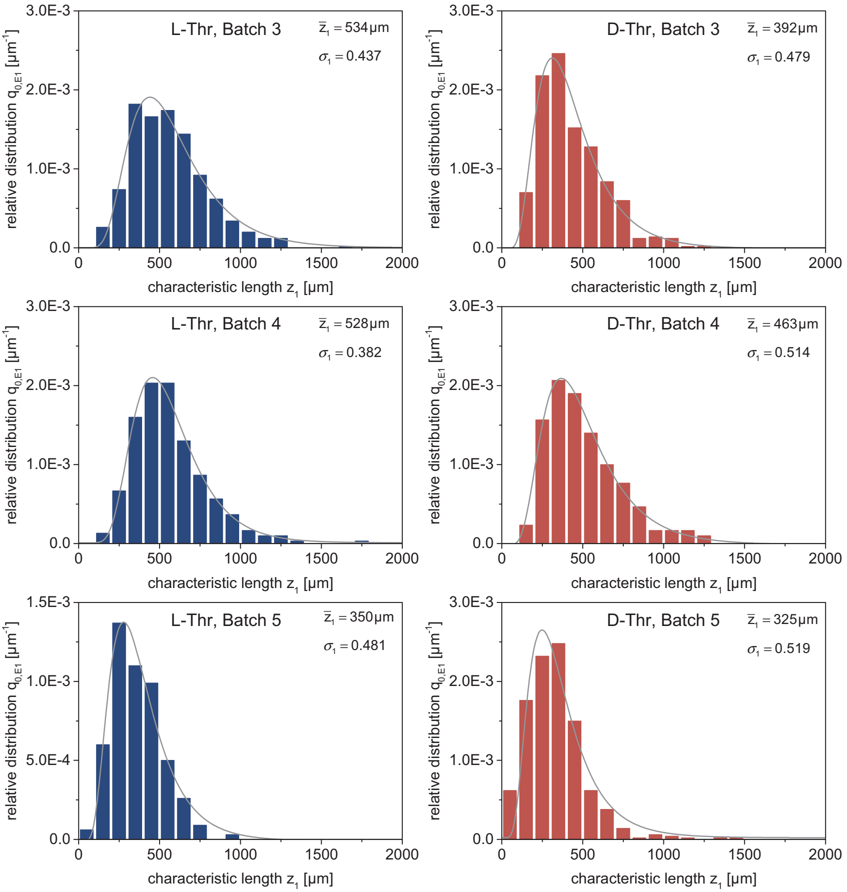

Figure 7.3: Seed crystal size distributions of batches 3-5.

7.5 Model parameters used for the optimization of CPC

The temperature trajectories obtained from the optimization of CPC presented in chapter 5.4.3 are based on the mathematical model described in chapter 3.1. The parameter values are given in Table 7.4 below. They differ from the final set obtained from the parameter estimation done for this work. However, these values were obtained from a preliminary parameter estimation using the same set of conventional and coupled PC experiments as done for the final parameter estimation in chapter 5.1.

Table 7.4: Model parameter values used for the optimization of coupled preferential crystallization (CPC).

No.	*kinetics*	*parameter*	*value*	*unit*
1	growth	$k_{g,0}$	9.4383e6	$m\,s^{-1}s^{n_g}$
2		E_{Ag}	75.8920	kJ/mol
3		g	1.7037	-
4	secondary nucleation	$k_{bsec,0}$	1.0331e27	$s^{-1}(m^3)^{-n_{\mu 3}}$
5		b_{sec}	2.8003	-
6		$n_{\mu 3}$	3.8596	-
7	primary nucleation	k_{bprim1}	2.5576e-6	$s^{-1}K^{-1}m^7kg^{-7/3}$
8		k_{bprim2}	2.0563e-3	-
9		A_{prim}	2.7536e1	$(m^2)^{-n_{\mu 2}}$
10		$n_{\mu 2}$	1.6176e-4	-

7.6 Further analysis of the optimization results

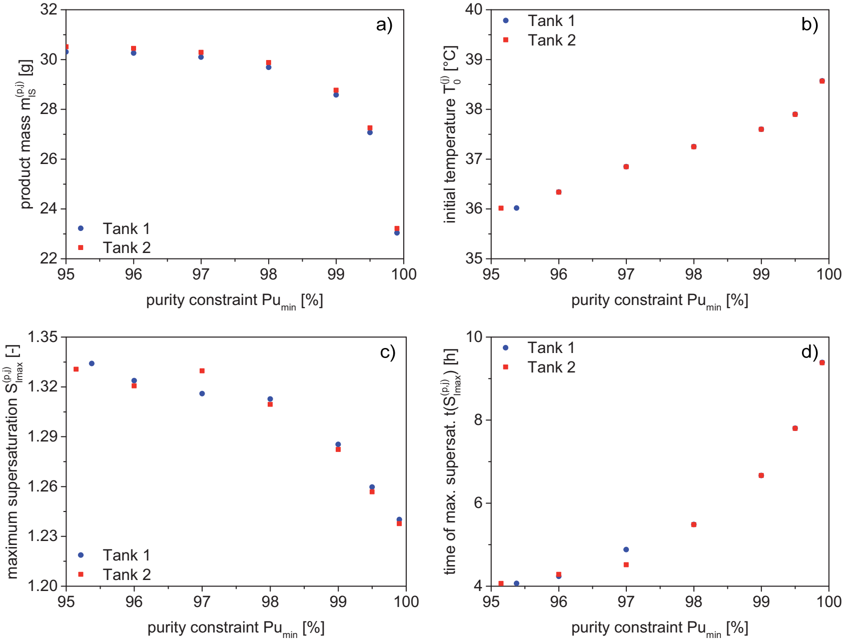

Figure 7.4: Relationship between characteristic points and the purity constraint obtained from the optimization of coupled preferential crystallization (CPC). a) Objective function, i.e. product mass. b) Initial temperature. c) Maximum supersaturation of the seeded enantiomers. d) Time at which the maximum supersaturation is reached.

7.7 Temperature control during optimized CPC

Figure 7.5 shows shows the effect on the double jacket temperature, T_{DJ}, in Tank 1 before (a) and after (b) the extension of the exchange lines. The temperature of the cooling section, $T_{ex,cool}$, was manually adjusted over the course of the experiment. With this addition, the maximum temperature difference between the slurry and the cooling agent could be reduced from 15 K to less than 5 K, which resulted in a higher overall purity in experiment CPC12a and a smaller difference regarding the product masses from each tank.

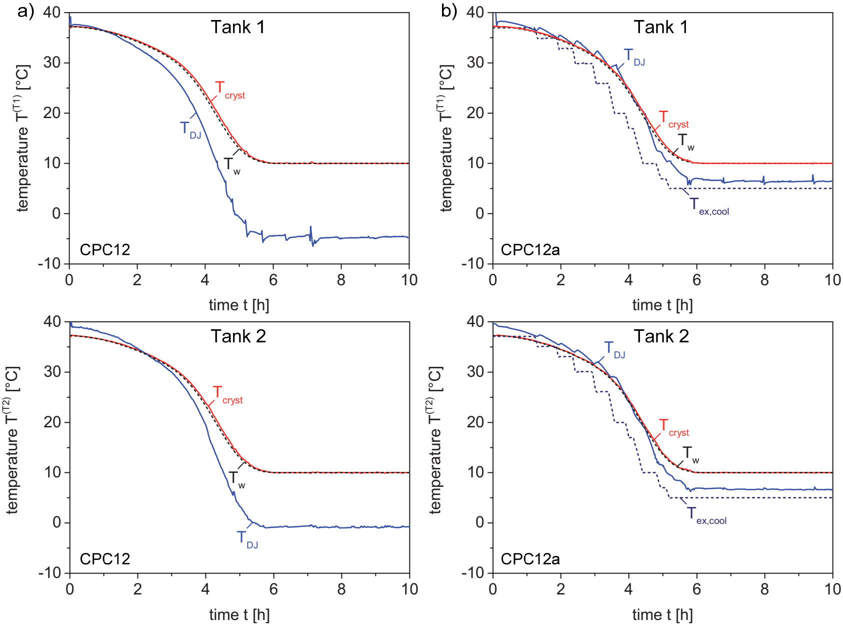

Figure 7.5: Comparison of the temperature trajectories in Tank 1 and Tank 2 during experiment CPC12 (a) and its repetition CPC12a (b). After the addition of a cooling section to the exchange lines, the minimum double jacket temperature T_{DJ} (blue line) could be raised to 5 °C in order to maintain a slurry temperature of T_{cryst} = 10 °C. $T_{ex,cool}$ is the temperature of the cooling section, which was manually adjusted during the process.

7.8 Product sieve analysis of optimized CPC experiments

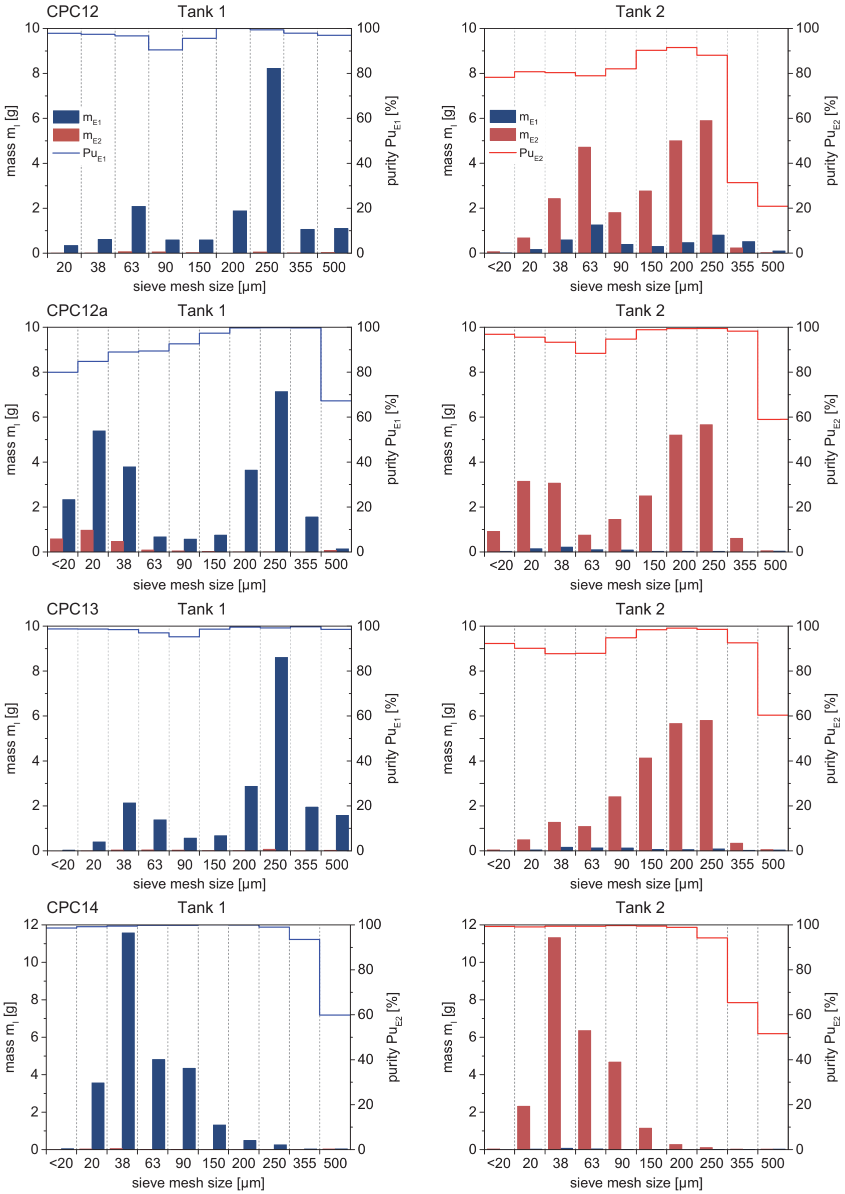

Figure 7.6: Sieve analysis of the products obtained from the optimized coupled PC experiments. Shown are mass m_l and purity Pu_l of each sieve fraction. The mesh size range 150 µm – 500 µm corresponds approximately to a characteristic crystal size z_1 between 1000 µm and 3700 µm.

7.9 Crystal shape evolution

In all versions of the model a constant volumetric shape factor k_V is assumed, which is based on a constant ratio of the two characteristic lengths z_1 and z_2 mentioned in chapter 4.1.1. For the case of threonine crystals, results from the CSD analyses of various experiments done in this work were evaluated in terms of their mean length-to-width ratio and its dependence on the mean characteristic length z_1. The results are plotted in Figure 7.7 for L- and D-Thr. In particular for the case of L-Thr shown in the left plot, a quite linear relationship can be identified. Three different data sets are shown: grey circles depict the five L-Thr seed batches, blue circles were obtained from conventional and coupled PC experiments; open circles represent data from experiments with the binary system L-Thr/H_2O.

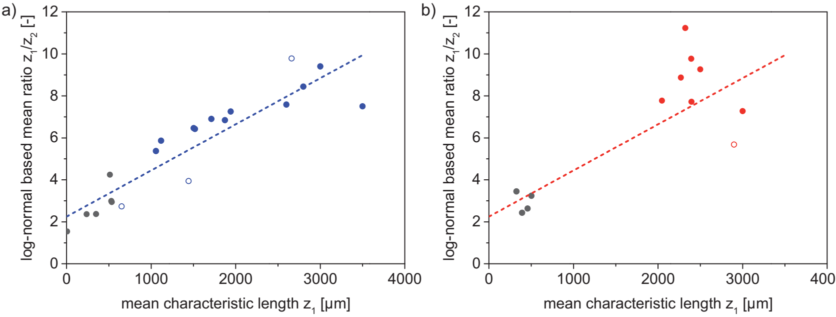

Figure 7.7: Correlation between the mean length to width ratio (z_1/z_2) and the mean characteristic length z_1 of (a) L-threonine and (b) D-threonine crystals.

The same applies to the graph in Figure 7.7b. For D-Thr, no conventional PC experiments like PC1a,b were done. For that reason, no data points are available in the medium size range (1000 – 2000 µm).

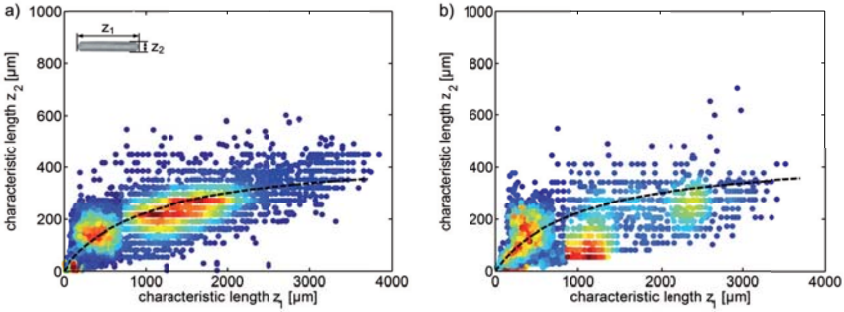

Figure 7.8: Full data set of (a) L-Thr and (b) D-Thr CSDs from which the mean aspect ratio z_1/z_2 was calculated. The dashed lines show the dependence $z_2 = f(z_1)$ using the linear regression from Figure 7.7a.

The parameters of the linear regression were obtained from L-Thr and is given as,

$$\frac{z_1}{z_2} = 2.2e^{-3} \mu m^{-1} \cdot z_1 + 2.2 \,. \qquad ((7.1)$$

The same line is plotted in Figure 7.7b for D-Thr. Based on this correlation, a simple extension of the model assuming a cuboid shape can be added to calculate the volumetric shape factor k_V as a function of the characteristic length z_1,

$$k_V = \left(2.2e^{-3}\mu m^{-1} \cdot z_1 + 2.2\right)^{-2}. \qquad ((7.2)$$

References

Abegg, C. F.; Stevens, J. D.; Larson, M. A., Crystal Size Distributions in Continuous Crystallizers when Growth Rate is Size Dependent. *AlChE J.* **1968,** 14, (1), 118-122.

Agranat, I.; Caner, H.; Caldwell, A., Putting chirality to work: The strategy of chiral switches. *Nat. Rev. Drug Discov.* **2002,** 1, (10), 753-768.

Angelov, I.; Raisch, J.; Elsner, M. P.; Eidel-Morgenstern, A. S., Optimal operation of enantioseparation by batch-wise preferential crystallization. *Chem. Eng. Sci.* **2008a,** 63, (5), 1282-1292.

Angelov, I.; Raisch, J.; Elsner, M. P.; Seidel-Morgenstern, A., Optimal operation of enantioseparation by batch-wise preferential crystallization. *Chem. Eng. Sci.* **2008b,** 63, (5), 1282-1292.

Bakhuis-Roozeboom, H. W., Löslichkeit und Schmelzpunkt als Kriteria für racemische Verbindungen, pseudoracemische Mischkrystalle und inactive Conglomerate. *Berichte der deutschen chemischen Gesellschaft* **1899,** 32, (1), 537-541.

Borchert, C.; Temmel, E.; Eisenschmidt, H.; Lorenz, H.; Seidel-Morgenstern, A.; Sundmacher, K., Image-Based in Situ Identification of Face Specific Crystal Growth Rates from Crystal Populations. *Cryst. Growth Des.* **2014,** 14, (3), 952-971.

Brandel, C.; ter Horst, J. H., Measuring induction times and crystal nucleation rates. *Faraday Discuss.* **2015,** 179, 199-214.

Burton, W. K.; Cabrera, N.; Frank, F. C., The Growth of Crystals and the Equilibrium Structure of their Surfaces. *Philosophical Transactions of the Royal Society of London Series a-Mathematical and Physical Sciences* **1951,** 243, (866), 299-358.

Collet, A., Separation and purification of enantiomers by crystallisation methods. *Enantiomer* **1999,** 4, (3-4), 157-172.

Coquerel, G., Preferential crystallization. *Top Curr Chem* **2007,** 269, 1-51.

Coquerel, G.; Petit, M.-N.; Bouaziz, R. Method of resolution of two enantiomers by crystallization. Patent 6,022,409, February 8, 2000.

Czapla, F. Modeling of polythermal preferential crystallization. Ph.D. thesis, Otto-von-Guericke-Universität Magdeburg, 2010.

Czapla, F.; Haida, H.; Elsner, M. P.; Lorenz, H.; Seidel-Morgenstern, A., Parameterization of population balance models for polythermal auto seeded preferential crystallization of enantiomers. *Chem. Eng. Sci.* **2009a,** 64, (4), 753-763.

Czapla, F.; Lorenz, H.; Seidel-Morgenstern, A., Modeling and comparison of Polytherm autoseeded process variants of preferences. *Chem. Ing. Tech.* **2009b,** 81, (6), 839-848.

Czapla, F.; Polenske, D.; Klukas, L.; Lorenz, H.; Seidel-Morgenstern, A., Cyclic auto-seeded polythermal preferential crystallization-Effect of impurity accumulation. *Chem. Eng. Process.* **2010,** 49, (1), 22-28.

de Boor, C., On calculating with B-splines. *Journal of Approximation Theory* **1972,** 6, (1), 50-62.

Ebbers, E. J.; Ariaans, G. J. A.; Houbiers, J. P. M.; Bruggink, A.; Zwanenburg, B., Controlled racemization of optically active organic compounds: Prospects for asymmetric transformation. *Tetrahedron* **1997,** 53, (28), 9417-9476.

Eicke, M.; Seidel-Morgenstern, A.; Elsner, M. P., Effect of fines dissolution on the performance of preferential crystallization for the production of pure enantiomers. *Chem Engineer Trans* **2009a,** 17, 651-656.

Eicke, M. J.; Angelov, I.; Seidel-Morgenstern, A.; Elsner, M. P. *Combining polythermal operation and fines destruction to increase the efficiency of simple batch preferential crystallization*, 4th International Conference on Population Balance Modelling, 15-17 September, 2010; Berlin, Germany.

Eicke, M. J.; Levilain, G.; Seidel-Morgenstern, A., Efficient Resolution of Enantiomers by Coupling Preferential Crystallization and Dissolution. Part 2: A Parametric Simulation Study to Identify Suitable Process Conditions. *Cryst. Growth Des.* **2013,** 13, (4), 1638-1648.

Eicke, M. J.; Seidel-Morgenstern, A.; Elsner, M. P. 2009b; *Preferential Crystallization including Fines Dissolution: How to kill two birds with one stone*, AIDIC Conference Series: pp 111-120,10.3303 / ACOS0909014.

Eisenschmidt, H.; Voigt, A.; Sundmacher, K., Face-Specific Growth and Dissolution Kinetics of Potassium Dihydrogen Phosphate Crystals from Batch Crystallization Experiments. *Cryst. Growth Des.* **2015,** 15, (1), 219-227.

Elsner, M. P.; Ziomek, G.; Seidel-Morgenstern, A., Simultaneous preferential crystallization in a coupled, batch operation mode - Part 1: Theoretical analysis and optimization. *Chem. Eng. Sci.* **2007,** 62, (17), 4760-4769.

Elsner, M. P.; Ziomek, G.; Seidel-Morgenstern, A., Efficient Separation of Enantiomers by Preferential Crystallization in Two Coupled Vessels. *AlChE J.* **2009,** 55, (3), 640-649.

Elsner, M. P.; Ziomek, G.; Seidel-Morgenstern, A., Simultaneous preferential crystallization in a coupled batch operation mode. Part II: Experimental study and model refinement. *Chem. Eng. Sci.* **2011,** 66, (6), 1269-1284.

Galan, K.; Eicke, M. J.; Elsner, M. P.; Lorenz, H.; Seidel-Morgenstern, A., Continuous Preferential Crystallization of Chiral Molecules in Single and Coupled Mixed-Suspension Mixed-Product-Removal Crystallizers. *Cryst. Growth Des.* **2015,** 15, (4), 1808-1818.

Hofmann, S.; Eicke, M.; Elsner, M. P.; Seidel-Morgen, A.; Raisch, J. *Innovative control strategies for coupled preferential crystallization*, WCPT6- World Congress on Particle Technology, 2010; Nuremberg.

Hofmann, S.; Raisch, J., Inversion-based Optimal Control of Batch Preferential Crystallization Processes. *At-Automatisierungstechnik* **2014,** 62, (2), 78-91.

Ito, A.; Matsuoka, M., Nucleation behavior of D-threonine on different faces of L-threonine crystals. *Cryst. Growth Des.* **2008,** 8, (8), 2716-2720.

Ito, T.; Ando, H.; Handa, H., Teratogenic effects of thalidomide: molecular mechanisms. *Cell. Mol. Life Sci.* **2011,** 68, (9), 1569-1579.

Jacques, J.; Collet, A.; Wilen, S. H., *Enantiomers, racemates, and resolutions*. Wiley: New York, 1981; p xv, 447 p.

Jones, C. M.; Larson, M. A., Characterizing growth-rate dispersion of NaNO3 secondary nuclei. *AlChE J.* **1999,** 45, (10), 2128-2135.

Kadam, S. S.; Kramer, H. J. M.; ter Horst, J. H., Combination of a Single Primary Nucleation Event and Secondary Nucleation in Crystallization Processes. *Cryst. Growth Des.* **2011,** 11, (4), 1271-1277.

Kadam, S. S.; Kulkarni, S. A.; Ribera, R. C.; Stankiewicz, A. I.; ter Horst, J. H.; Kramer, H. J. M., A new view on the metastable zone width during cooling crystallization. *Chem. Eng. Sci.* **2012,** 72, 10-19.

Kaemmerer, H.; Lorenz, H.; Seidel-Morgenstern, A., Alternative procedure to the racemate separation compound forming systems by means of crystallisation. *Chem. Ing. Tech.* **2009,** 81, (12), 1955-1965.

Kashchiev, D.; van Rosmalen, G. M., Review: Nucleation in solutions revisited. *Cryst. Res. Technol.* **2003,** 38, (7-8), 555-574.

Kreil, G., D-amino acids in animal peptides. In *Annu. Rev. Biochem*, Richardson, C. C., Ed. 1997; Vol. 66, pp 337-345.

Krieger, K. H.; Lago, J.; Wantuck, J. A. Verfahren zur Trennung von racemischen Gemischen optisch aktiver Enantiomorpher. Patent DE1543238, 1965.

Levilain, G.; Eicke, M. J.; Seidel-Morgenstern, A., Efficient resolution of enantiomers by coupling preferential crystallization and dissolution. Part 1: Experimental proof of principle. *Cryst. Growth Des.* **2012,** 12, (11), 5396-5401.

Levilain, G.; Rougeot, C.; Guillen, F.; Plaquevent, J. C.; Coquerel, G., Attrition-enhanced preferential crystallization combined with racemization leading to redissolution of the antipode nuclei. *Tetrahedron-Asymmetry* **2009,** 20, (24), 2769-2771.

Lorenz, H.; Le Minh, T.; Kaemmerer, H.; Buchholz, H.; Seidel-Morgenstern, A., Exploitation of shifts of eutectic compositions in crystallization-based enantioseparation. *Chem. Eng. Res. Des.* **2013,** 91, (10), 1890-1902.

Lorenz, H.; Perlberg, A.; Sapoundjiev, D.; Elsner, M. P.; Seidel-Morgenstern, A., Crystallization of enantiomers. *Chem. Eng. Process.* **2006,** 45, (10), 863-873.

Lorenz, H.; Seidel-Morgenstern, A., Processes To Separate Enantiomers. *Angew Chem Int Edit* **2014,** 53, (5), 1218-1250.

Maggioni, G. M.; Mazzotti, M., Modelling the stochastic behaviour of primary nucleation. *Faraday Discuss.* **2015,** 179, 359-382.

Meierhenrich, U., Amino Acids and the Asymmetry of Life Caught in the Act of Formation Preface. In *Advances in Astrobiology and Biogeophysics*, Meierhenrich, U., Ed. 2008; pp XI-XIII,207-228.

Mersmann, A., *Crystallization technology handbook*. Marcel Dekker: New York, 2001; p xiv, 832 p.

Mullin, J. W., *Crystallization*. Butterworth-Heinemann: Oxford ; Boston, 2001; p xv, 594 p.

Ndzie, E.; Cardinael, P.; Schoofs, A. R.; Coquerel, G., An efficient access to the enantiomers of alpha-methyl-4-carboxyphenylglycine via a hydantoin route using a practical variant of preferential crystallization AS3PC (auto seeded programmed polythermic preferential crystallization). *Tetrahedron-Asymmetry* **1997,** 8, (17), 2913-2920.

Nývlt, J., *The Kinetics of industrial crystallization*. Elsevier Science Pub. Co., Inc. distributor: Amsterdam ; New York, 1985; p 350 p.

Pasteur, L., Mémoire sur la relation qui peut exister entre la forme cristalline et la composition chimique, et sur la cause de la polarisation rotatoire. *Comptes rendus hebdomadaires des séances de l' Académie des Sciences* **1848,** 26, 535-538.

Podlech, J., Origin of organic molecules and biomolecular homochirality. *Cell. Mol. Life Sci.* **2001,** 58, (1), 44-60.

Polenske, D. Untersuchungen zur Racemattrennung von Threonin mit Hilfe der Preferential Crystallisation. Diploma thesis, Hochschule Magdeburg-Stendal, 2003.

Polenske, D. Bewertung des Potentials der Bevorzugten Kristallisation zur Enantiomerentrennung. Ph.D. thesis, Otto-von-Guericke-Universität Magdeburg, 2010.

Polenske, D.; Elsner, M. P.; Lorenz, H.; Seidel-Morgenstern, A., Alternative possibilities for assigning "favoured crystallisation" to enantiomer separation. *Chem. Ing. Tech.* **2006,** 78, (8), 1101-1110.

Profir, V. M.; Matsuoka, M., Processes and phenomena of purity decrease during the optical resolution of DL-threonine by preferential crystallization. *Colloids Surf., A* **2000,** 164, (2-3), 315-324.

Qamar, S.; Warnecke, G.; Elsner, M. P.; Seidel-Morgenstern, A., A Laplace transformation based technique for reconstructing crystal size distributions regarding size independent growth. *Chem. Eng. Sci.* **2008,** 63, (8), 2233-2240.

Ramkrishna, D., *Population balances: theory and applications to particulate systems in engineering*. Academic Press: San Diego, CA, 2000; p xvi, 355 p.

Randolph, A. D.; Larson, M. A., *Theory of particulate processes : analysis and techniques of continuous crystallization*. Academic Press: San Diego, 1988; p xv, 369 p.

Sakai, K.; Hirayama, N.; Tamura, R., Novel Optical Resolution Technologies. In *Top Curr Chem*, Sakai, K.; Hirayama, N.; Tamura, R., Eds. 2007; Vol. 269, pp 1-313.

Sapoundjiev, D.; Lorenz, H.; Seidel-Morgenstern, A., Solubility of chiral threonine species in water/ethanol mixtures. *J. Chem. Eng. Data* **2006,** 51, (5), 1562-1566.

Srisanga, S.; Flood, A. E.; Galbraith, S. C.; Rugmai, S.; Soontaranon, S.; Ulrich, J., Crystal Growth Rate Dispersion versus Size-Dependent Crystal Growth: Appropriate Modeling for Crystallization Processes. *Cryst. Growth Des.* **2015,** 15, (5), 2330-2336.

Tulashie, S. K.; Lorenz, H.; Hilfert, L.; Edelmann, F. T.; Seidel-Morgenstern, A., Potential of chiral solvents for enantioselective crystallization. 1. Evaluation of thermodynamic effects. *Cryst. Growth Des.* **2008,** 8, (9), 3408-3414.

Tulashie, S. K.; Lorenz, H.; Seidel-Morgenstern, A., Potential of Chiral Solvents for Enantioselective Crystallization. 2. Evaluation of Kinetic Effects. *Cryst. Growth Des.* **2009,** 9, (5), 2387-2392.

Ulrich, J., Growth-Rate Dispersion - A Review. *Cryst. Res. Technol.* **1989,** 24, (3), 249-257.

Versteeg, H. K.; Malalasekera, W., *An introduction to computational fluid dynamics - The finite volume method*. Longman Scientific & Technical: Essex, England, 1995.

Volmer, M.; Weber, A., Germ-formation in oversaturated figures. *Zeitschrift Fur Physikalische Chemie--Stochiometrie Und Verwandtschaftslehre* **1926,** 119, (3/4), 277-301.

Wurges, K.; Petrusevska-Seebach, K.; Elsner, M. P.; Lutz, S., Enzyme-Assisted Physicochemical Enantioseparation Processes-Part III: Overcoming Yield Limitations by Dynamic Kinetic Resolution of Asparagine Via Preferential Crystallization and Enzymatic Racemization. *Biotechnol. Bioeng.* **2009,** 104, (6), 1235-1239.

Yoshioka, R., Racemization, optical resolution and crystallization-induced asymmetric transformation of amino acids and pharmaceutical intermediates. *Top Curr Chem* **2007,** 269, 83-132.

Ziomek, G. Evaluation of different operation modes for chromatographic and crystallization processes. Ph.D. thesis, Otto-von-Guericke-Universität Magdeburg, 2011.

List of figures

Figure 1.1: Examples of chiral molecules and their different effects in biological organisms............................... 3

Figure 2.1: Binary melting point phase diagrams of the three known systems: a) conglomerate, b) racemic compound, c) solid solution (pseudoracemate) of Roozeboom Type I (ideal solid solution), Type II (maximum melting point at racemic composition) and Type III (minimum melting point at racemic composition). 9

Figure 2.2: Schematic representation of a solubility diagram for a binary system, consisting of solute and solvent. 11

Figure 2.3: Ternary phase diagram of a conglomerate (a) and a compound forming system (b). The dotted lines represent the eutectic compositions. The number of coexisting phases in each region is indicated by Roman numerals. 11

Figure 2.4: Crystallization consists of two major processes. Nucleation is responsible for the appearance of the new solid phase from a clear solution. Growth is the process by which the addition of solute molecules to the existing solid phase results in an increase in particle size. Dissolution can be considered as the opposite and eventually causes the disappearance of the solid phase. 13

Figure 2.5: Change of the overall free energy ΔG as a function of cluster size d for homogeneous nucleation... 14

Figure 2.6: Principle of preferential crystallization. From t0 to t1, pure E1 can be obtained. Nucleation of the counter enantiomer E2 occurs just after t1, which leads to a gradual contamination of the product until the new equilibrium is reached. 17

Figure 2.7: Typical time trend of the liquid mass fractions of the seeded (E1, blue) and unseeded (E2, red) enantiomers (a) and the corresponding trajectory in a small region of the ternary phase diagram (b). 18

Figure 2.8: Principle of coupled preferential crystallization. Both crystallizers are connected via the liquid phase by a continuous exchange of crystal free solution. E1 and E2 crystallize separately in each crystallizer. Under ideal conditions, no nucleation of the respective counter enantiomer occurs. . 19

Figure 2.9: Typical time trend of the liquid mass fractions of the respective seeded enantiomer in each crystallizer (grey bold line) (a) and the corresponding trajectory in a small region of the ternary phase diagram (b). 20

Figure 2.10: Principle of coupling preferential crystallization and selective dissolution. The solution in tank 1 is kept below saturation temperature, while tank 2 remains at the initial saturation temperature. .. 21

Figure 3.1: System of two coupled subsystems and a representative volume element. 25

Figure 3.2: Definition of characteristic lengths for the quantification of particle properties. 26

Figure 3.3: Central control volume element. 33

Figure 3.4: Boundary control volume elements. 35

Figure 3.5: Crystallizer with an attached fines dissolution unit and the resulting in- and output streams. 35

Figure 3.6: Controller structure for symmetry control of coupled preferential crystallization. 40

Figure 3.7: Controller structure for constant supersaturation control of coupled PC. 41

Figure 3.8: Clamped (a) and open (b) B-Spline curves B(t), and their underlying basis functions Ni,d(t). 43

Figure 3.9: Triangle diagram, visualizing the de Boor-algorithm (eqs. (3.58), (3.59)). The construction of the third degree basis function for i = 1, N1,3, is highlighted. Clearly, N1,3 is nonzero across the interval [u1, u5]. 44

Figure 4.1: The four stereoisomers of threonine result from the two stereogenic (chiral) centers. 48

Figure 4.2: a) Solubility of L-Thr and the racemate in water. Symbols are measured, lines calculated values using the fitted solubility correlation (eq. (3.17)). b) Ternary phase diagram of the DL-Thr/water system for a temperature range of 10 to 40 °C. Open symbols represent solubility data reported by

Sapoundjiev et al. (2006). Solid symbols in b) are own measurements. The lines are calculated values (eq. (3.17)). 49

Figure 4.3: PI flow diagram of the crystallization plant used for single and coupled batch operation. Fines removal loops are not shown (compare Figure 4.5). 50

Figure 4.4: Signal network for symmetry and constant supersaturation control. 53

Figure 4.5: Crystallizer with the additional heated loop for fines dissolution (a). Fines dissolution filter built from a wire mesh with a spacing of 500 µm and a Büchner funnel for support of the cap (b). 56

Figure 5.1: Simulation (solid and dashed lines) of the isothermal benchmark experiment (see section 5.2.1) using the model and parameter values reported by Czapla, et al. (2009b) (a) and Ziomek (2011) (b). Symbols denote experimental data from the benchmark experiment PC1 done in this work. E1 is the seeded enantiomer. 61

Figure 5.2: a) Resulting model fit when only experiment PC2 is used for parameter estimation. b) The obtained optimal parameter values applied to experiment PC4 do not produce the same quality of agreement, which is also reflected by the value of the objective function J (eq. 3.49). 62

Figure 5.3: Measured (symbols) and simulated (lines) concentration profiles of six PC experiments (Table 5.1) used for the parameter estimation. The value of the objective function J is given for each individual experiment. 65

Figure 5.4: Measured (symbols) and simulated (lines) concentration profiles of five coupled preferential crystallization experiments (CPC) used for the parameter estimation. The value of the objective function J resulting from the simulation with the optimal parameters for CPC in Table 5.2 is indicated for each individual experiment. 66

Figure 5.5: Further examination of the simulation of the benchmark experiment PC1. Depicted are the trends of: (a) supersaturation SI, (b) growth rate GI, (c) primary nucleation rate BIprim and (d) secondary nucleation rate BIsec for each enantiomer. I = E1 (seeded), E2 (unseeded). 69

Figure 5.6: a) Calculated primary nucleation kinetics at 30 °C according to eq. (3.23) as a function of supersaturation and the second moment of the opposite enantiomer. The white curve is the trajectory of the unseeded enantiomer from the simulation of experiment PC1. The dark line is its projection into the x-y-plane. b) Calculated primary nucleation rate for µ2 = 0, which is the contribution of eq. (3.22) alone. 69

Figure 5.7: Simulated evolution of the crystal size distribution of the seeded (a) and unseeded (b) enantiomers E1 and E2 respectively under experimental conditions of experiment PC1. 71

Figure 5.8: Twofold repetition of the benchmark experiment PC1 (solid lines) with an interruption for product capture after 1.2 h (circles: PC1a, squares: PC1b). a) Liquid phase mass fraction and turbidity signal. b) Supersaturation and temperature. 72

Figure 5.9: a) Seed and product crystal size distributions of experiments PC1a and PC1b after 1.2 h process duration. Lines represent fitted log-normal distributions. b) Micrograph of the L-threonine seeds and (c) the product obtained from PC1b, respectively. The bars have a span of 1000 µm. 73

Figure 5.10: a) Mass fractions in the liquid phase during preferential crystallization with fines dissolution (red and blue circles and solid lines) and without fines dissolution (grey squares and dashed lines). b) Corresponding supersaturation profiles with fines dissolution (solid lines) and without (dashed lines) as well as temperature. 75

Figure 5.11: Comparison of the crystal size distributions (a) at tstop without (b) and with fines dissolution (c). 76

Figure 5.12: a) Mass fractions of enantiomers E1 and E2 when the second design of the FDU is used (solid lines) in comparison to two conventional PC processes under identical operating conditions without fines dissolution (symbols, dashed lines). b) Repetition of experiment PC-FD2 under slightly polythermal conditions and filtration after 3.9 h. 77

Figure 5.13: Summary of conventional PC experiments including the application of fines dissolution. All experiments were done at a crystallization temperature of 30 °C. Product purity was at least 99%

in all cases. a) Productivity versus the increase in solid mass. b) Mean crystal size versus the increase in solid mass. 79

Figure 5.14: a,b) Liquid phase concentration of enantiomers E1 and E2 in each crystallizer (T1, T2) and the corresponding supersaturation trends (c,d) during the isothermal benchmark experiment CPC1. Tank 1 was seeded with 0.5 g of L-Thr, Tank 2 with 0.5 g of D-Thr. 80

Figure 5.15: Crystal size distributions of the L- and D-Thr seeds (Batch 3) and the final products obtained from Tank 1 (a) and Tank 2 (b) at the end of experiment CPC1. 82

Figure 5.16: Comparison of coupled and conventional PC experiments CPC1 (Tank 1) and PC2 regarding solid mass of preferred enantiomer E1 (a) and productivity (b) calculated with eqs. (4.9), (4.10) and (4.13), respectively. After tstop conventional preferential crystallization does not produce pure enantiomer anymore. 83

Figure 5.17: a,b) Liquid phase concentration of enantiomers E1 and E2 in each crystallizer (T1, T2) and the corresponding supersaturation trends (c,d) during the isothermal experiment CPC-FD1. Tank 1 was seeded with 0.5 g of L-Thr, Tank 2 with 0.5 g of D-Thr. The dashed lines show the trends from the previous experiment CPC1. 84

Figure 5.18: Crystal size distributions of the L- and D-Thr seeds (Batch 3) and the final products obtained from Tank 1 and Tank 2 at the end of experiment CPC-FD1. 85

Figure 5.19: a) Concentration profiles of the preferred enantiomers in each crystallizer during experiment CPC3. b) Supersaturation profiles of the counter enantiomers and temperature profiles. 87

Figure 5.20: Polythermal operation of coupled preferential crystallization using four different linear cooling profiles. Shown are the mass fractions of the seeded enantiomers (E1 in Tank 1, E2 in Tank 2) for experiments CPC4 (a), CPC5 (b), CPC6 (c) and CPC7 (d). The concentration trend of E1 from experiment CPC1 is indicated by the grey dashed lines. 88

Figure 5.21: Corresponding supersaturation trends of the unseeded enantiomers (E2 in Tank 1, E1 in Tank 2) during polythermal operation of coupled preferential crystallization. 89

Figure 5.22: Coupled, isothermal experiment CPC8 with unequal initial conditions. Shown are the concentration trends of the two seeded enantiomers of each crystallizer (a) as well as the supersaturation of the unseeded species (b). Grey dashed lines represent the benchmark experiment CPC1. Tank 1 was seeded with 2 g of L-Thr, Tank 2 with 0.5 g of D-Thr. 92

Figure 5.23: Product crystal size distributions of L-Thr (a) and D-Thr (b) obtained from the uncontrolled experiment CPC8 with unequal initial conditions. 92

Figure 5.24: Experiment CPC9: application of the symmetry controller when Tank 2 is the master (cf. Figure 3.6). Tank 1 was seeded with 2 g of L-Thr, Tank 2 with 0.5 g of D-Thr. The temperature in Tank 1 was adjusted by the controller so that the concentration of seeded E1 follows the concentration of seeded E2 in the second Tank. a) Measured concentration profiles of the seeded enantiomers (symbols) and the estimation (solid lines) which served as the input for the PI-controller. Grey dashed lines represent the benchmark experiment CPC1. b) Temperature (lines) as well as supersaturation of the seeded enantiomers (symbols). 93

Figure 5.25: Crystal size distributions of the products obtained from experiment CPC9 involving the symmetry controller. 94

Figure 5.26: Experiment CPC10: application of the symmetry controller when Tank 1 is the master (cf. Figure 3.6). Tank 1 was seeded with 2 g of L-Thr, Tank 2 with 0.5 g of D-Thr. The temperature in Tank 2 was adjusted by the controller so that the concentration of seeded E2 follows the concentration of seeded E1 in the first Tank. a) Measured concentration profiles of the seeded enantiomers (symbols) and the estimation (dashed lines) which served as the input for the PI-controller. b) Temperature (lines) and supersaturation of the respective counter enantiomers (symbols). 94

Figure 5.27: Product crystal size distributions of experiment CPC10 obtained from Tank 1 (a) and Tank 2 (b). 95

Figure 5.28: Application of the constant supersaturation controller in experiment CPC11. a, b) Measured (symbols, ~) and estimated concentration (lines, ^). The latter was used to calculate the current supersaturation estimate. c, d) Supersaturation calculated from concentration measurements (symbols) together with estimated values of S (lines) and temperature Tcryst. 97

Figure 5.29: Product crystal size distributions obtained from experiment CPC11 using constant supersaturation control.. 98

Figure 5.30: Calculated optimal temperature trajectories for coupled PC with different purity constraints Pu (a) and the resulting simulated supersaturation trends of the seeded enantiomer in Tank 1 (b). The bold blue trajectories (98% and 99.9%) were investigated experimentally. The dashed lines are the result of an unconstraint optimization. The lowest purity that still leads to a maximization of the product mass is approximately 95%. 100

Figure 5.31: Concentrations wE1L and wE2L of L-Thr (blue circles, seeded in T1) and D-Thr (red squares, seeded in T2) and temperature trajectories in each crystallizer obtained from the optimized experiments CPC12 and CPC12a (a,b), CPC13 (c,d) and CPC14 (e,f). In experiments CPC12/CPC12a a temperature trajectory optimized for 98% purity was used. The second trajectory used for CPC12 and CPC14 was optimized for 99.9% purity. Unlike the first two experiments, milled seeds were used in CPC14. 103

Figure 5.32: Supersaturation SE1 andSE2 of L-Thr (blue circles, seeded in T1) and D-Thr (red squares, seeded in T2), respectively, during the validation of two optimized temperature profiles. Next to the measured temperature Tcryst, the setpoint trajectories, Tw, are shown. 104

Figure 5.33: Total masses lost via the replacement of the exchange filter frits during the optimized coupled experiments (CPC12 – CPC14) compared with the two previous polythermal experiments CPC4 and CPC7. Also indicated are the compositions of the solid adhering to the filters. 106

Figure 5.34: Mass fraction, wIL, and supersaturation, SI, in both crystallizers showing the full dynamics until equilibrium during the first coupled preferential crystallization-dissolution experiment CPC-D1. L-Thr (E1) is indicated by red circles, D-Thr (E2) by blue squares. 109

Figure 5.35: Schematic illustration of the liquid and solid phase repartitioning during the coupled preferential crystallization-dissolution experiment CPC-D1. 110

Figure 5.36: Mass fractions from two coupled preferential crystallization-dissolution experiments, CPC-D2 (a) and CPC-D3 (b). Solid symbols are measurements from the crystallization Tank 1, open symbols from the dissolution Tank 2. 111

Figure 5.37: Comparison of the productivities PrI and the increase in product mass ∞mIS obtained from the conventional PC, coupled PC and coupled PC-dissolution experiments. In the lower left corner, results of the conventional process are shown (cf. Figure 5.13a). Red dots signify that the product purity was below 98%. Results in Tank 1 (a) are for L-Thr, in Tank 2 (b) for D-Thr. 113

Figure 5.38: Simulation of the benchmark experiment PC1 using the parameters optimal for coupled PC (Table 5.2). a) mass fractions wIL in the liquid phase, b) simulated masses mIS of the solid phase. t98 indicates the point where the product (E1) has a purity of 98%, i.e. the induction time of nucleation. 115

Figure 5.39: Comparison of conventional PC (a) and CPC (b). Predicted relative product yields YE1 obtained after t98 are indicated by circles. The points in time t98 where the product still has a purity of 98% are represented by squares. In all cases the initial solution was saturated at Tsat = 43.7 °C. 116

Figure 5.40: Comparison of the productivities of conventional and coupled PC. Under the specific process conditions (concentration, mass and size of seeds, exchange flow rate), CPC can be operated safely above 30.5 °C. 117

Figure 5.41: Influence of the exchange flow rate Fex at different initial temperatures on the process time t98 (a) and the relative yield YE1 (b) for CPC. The red areas on the right side of each plot indicate operating conditions under which CPC completely avoids nucleation of the unseeded enantiomers. Results are for Tank 1 only due to perfect symmetry. 118

Figure 5.42: Simulation of CPC-D1 using model parameters optimal for coupled preferential crystallization (see Table 5.2). a,b) Experimental and simulated evolution of the liquid phases. c,d) Predicted trends of the solid phase. The point at which the seeded enantiomer E1 is dissolved from the solid racemate in Tank 2 is labeled tdiss. The onset of nucleation of E2 in Tank 1 is labeled tnuc. 119

Figure 5.43: Parametric simulation study of CPC-D at various crystallization temperatures in Tank 1. Additionally, the exchange rate Fex as well as the seed size were changed. The conditions were as follows. a) Fex = 11 mL/min, mE1seeds = 2 g (Batch 5); b) Fex = 50 mL/min, mE1seeds = 2 g (Batch 5); c) Fex = 50 mL/min, mE1seeds = 2 g (milled, zmean = 50 µm). The initial solutions were all saturated at Tsat,0 = 43.7 °C. The mass of solid racemate in Tank 2 was mracS = 20 g. Tank 1 was seeded with 2 g of L-Thr (E1). Within the attractive region, pure enantiomer can be obtained from both tanks. 120

Figure 6.1: Process strategies for batch preferential crystallization investigated in this work. 126

Figure 7.1: Nucleation behavior of threonine. a) Induction time of L-Thr/H2O as a function of cooling rate and degree of supercooling. b) Nucleation of DL-/Thr/H2O at two different cooling rates. 135

Figure 7.2: Seed crystal size distributions of batches 1 and 2. 135

Figure 7.3: Seed crystal size distributions of batches 3-5. 136

Figure 7.4: Relationship between characteristic points and the purity constraint obtained from the optimization of coupled preferential crystallization (CPC). a) Objective function, i.e. product mass. b) Initial temperature. c) Maximum supersaturation of the seeded enantiomers. d) Time at which the maximum supersaturation is reached... 137

Figure 7.5: Comparison of the temperature trajectories in Tank 1 and Tank 2 during experiment CPC12 (a) and its repetition CPC12a (b). After the addition of a cooling section to the exchange lines, the minimum double jacket temperature TDJ (blue line) could be raised to 5 °C in order to maintain a slurry temperature of Tcryst = 10 °C. Tex,cool is the temperature of the cooling section, which was manually adjusted during the process.. 138

Figure 7.6: Sieve analysis of the products obtained from the optimized coupled PC experiments. Shown are mass mI and purity PuI of each sieve fraction. The mesh size range 150 µm – 500 µm corresponds approximately to a characteristic crystal size z1 between 1000 µm and 3700 µm. 139

Figure 7.7: Correlation between the mean length to width ratio (z1/z2) and the mean characteristic length z1 of (a) L-threonine and (b) D-threonine crystals. 140

Figure 7.8: Full data set of (a) L-Thr and (b) D-Thr CSDs from which the mean aspect ratio z1/z2 was calculated. The dashed lines show the dependence z2 = f(z1) using the linear regression from Figure 7.7a. 140

List of tables

Table 3.1: Model parameters for the simulation of preferential crystallization of threonine. 44

Table 4.1: List of the plant instrumentation. 50

Table 4.2: Seed crystal batches and their log-normal size distribution parameters zI and ∞an 54

Table 4.3: Standard (initial) operating conditions for conventional batch PC. L-Thr was the seeded enantiomer in most cases. 54

Table 4.4: Additional process parameters specific to coupled preferential crystallization. 55

Table 4.5: Operating conditions of the fines dissolution unit. 56

Table 4.6: Overview of the investigated process strategies for preferential crystallization. 57

Table 5.1: Overview of important experimental conditions of conventional (PC) and coupled preferential crystallization (CPC) processes used for parameter estimation. The initial solutions all had a concentration of wIL0 = 0.1009 g/g, which corresponds to a saturation temperature of Tsat = 43.7 °C. Additional process conditions are given in Appendix 7.1. The PC processes were seeded with L-Thr. The CPC processes were seeded with L- and D-Thr in Tank 1 and Tank 2, respectively. Experiments CPC2 and 3 were not used for parameter estimation. 63

Table 5.2: Optimal parameter values obtained from estimation using the six conventional PC and five coupled PC experiments (PC and CPC). The index I = E1, E2 is omitted since the parameters apply to both enantiomers. 64

Table 5.3: Final solid masses mIS and purities PuI predicted by simulation of conventional (PC) and coupled preferential crystallization (CPC) after 10 h process duration using the respective optimal parameter set. 67

Table 5.4: Final product masses and purities of three polythermal CPC experiments predicted by the simulation with the kinetic parameters found optimal for conventional PC. 68

Table 5.5: Comparison of product mass, purity and mean crystal size of experiments PC1, PC1a, PC1b and the corresponding model predictions. Values in brackets were determined based on the concentration measurement. 74

Table 5.6: Initial solution composition for conventional PC with fines dissolution (experiments PC-FD1 and PC-FD1a). 75

Table 5.7: Comparison of product mass, purity and mean crystal size of experiments PC-FD1, PC-FD1a and the corresponding model predictions. Values in brackets were determined based on the concentration measurement. 76

Table 5.8: Dimensions of the fines dissolution units (FDU) and the corresponding mean residence times at a flow rate of 50 ml/min. Design 1 was used for experiment PC-FD1, design 2 for experiment PC-FD2. 77

Table 5.9: Comparison of product mass, purity and mean crystal size obtained from experiments PC-FD2 and PC-FD2a using the second design of the FDU with conventional experiments PC2 and PC2a. Values in brackets were calculated based on the concentration measurement. 78

Table 5.10: Results of the product analysis from experiment CPC1. Tcryst = 30 °C, mseeds = 0.5 g, tstop = 19 h. Values in brackets are estimates based on the concentration signals (eq. (4.10)). 82

Table 5.11: Results of the product analysis from experiment CPC-FD1. Tcryst = 30 °C, mseeds = 0.5 g, tstop = 19 h. Values in brackets are estimates based on the concentration signals (eq. (4.10)). 85

Table 5.12: Results of the product analysis from the polythermal experiment CPC3. Tcryst = 30 °C to 20 °C (stepwise reduction), mseeds = 0.5 g, tstop = 11 h. 87

Table 5.13: Results of the product analysis of the four polythermal coupled experiments CPC4, 5, 6 and 7....... 90

Table 5.14: Mass and composition† of solid adhering to the replaced exchange filter. 90

Table 5.15: Results of the product analysis of the uncontrolled experiment CPC8 with unequal seed masses and the two experiments using the symmetry controller, CPC9 and CPC10. In all cases Tank 1 was seeded with 2 g of L-Thr and 0.5 g of D-Thr taken from batch 3 (see Table 4.2). Process duration was 10 h. 95

Table 5.16: Results of the product analysis from experiment CPC11 using constant supersaturation control. mseeds = 0.5 g, tstop = 10 h. 99

Table 5.17: Simulated results of optimized CPC showing the predicted final product masses, mIS (objective function), and purities, PuI, for different purity constraints, Pumin. 101

Table 5.18: Initial solution composition in each crystallizer for the optimized coupled processes CPC12a, CPC13 and CPC14. 102

Table 5.19: Results of the product analysis of the optimized polythermal experiments. 105

Table 5.20: Initial solution composition and operating conditions for three coupled PC and selective dissolution (CPC-D) experiments. The mass of racemic DL-Thr is denoted as mrac. 108

Table 5.21: Results of the product analysis of experiments CPC-D2 and CPC-D3, stopped after 3 h and 2.5 h, respectively. 111

Table 7.1: Process conditions of all conventional PC experiments. 132

Table 7.2: Process conditions of coupled preferential experiments. 133

Table 7.3: Experimental conditions of coupled preferential crystallization and selective dissolution (CPC-D). 134

Table 7.4: Model parameter values used for the optimization of coupled preferential crystallization (CPC). ... 137

List of publications

Journal articles

Temmel E, Eicke MJ, Lorenz H, Seidel-Morgenstern A. *A short-cut-method for the quantification of crystallization kinetics - Part 2: Experimental application.* Cryst. Growth Des. Manuscript ID: cg-2016-00789m.R1

Galan K, Eicke MJ, Elsner MP, Lorenz H, Seidel-Morgenstern A. *Continuous preferential crystallization of chiral molecules in single and coupled Mixed-Suspension Mixed-Product-Removal crystallizers.* Cryst. Growth Des. **2015**, 15 (4), 1808-1818

Eicke MJ, Levilain G, Seidel-Morgenstern A. *Efficient resolution of enantiomers by coupling preferential crystallization and dissolution. Part 2: A parametric simulation study to identify suitable process conditions.* Cryst. Growth Des. **2013**, *13* (4), 1638-1648.

Levilain G, Eicke MJ, Seidel-Morgenstern A. *Efficient resolution of enantiomers by coupling preferential crystallization and dissolution. Part 1: Experimental proof of principle.* Cryst. Growth Des. **2012**, *12* (11), 5396-5401.

Hofmann, S., Eicke, M., Elsner, M.P., Seidel-Morgenstern, A., Raisch, J., *A Worst-Case Observer for Impurities in Enantioseparation by Preferential Crystallization.* Proceedings of the 21st European Symposium on Computer Aided Process Engineering (ESCAPE-21) **2011**, *29*, 860-864.

Eicke, M.; Seidel-Morgenstern, A.; Elsner, M. P.*, Effect of fines dissolution on the performance of preferential crystallization for the production of pure enantiomers.* Chem Engineer Trans **2009,** *17*, 651-656.

Conference contributions

Jahrestreffen der Fachgruppen Kristallisation, Partikelmesstechnik, Zerkleinern & Klassieren, mit Fachgemeinschaftstag Formulierung, Magdeburg, Deutschland, 18.-20. März 2015
Galan K, Eicke MJ, Elsner MP, Lorenz H, Seidel-Morgenstern A. *Continuous enantioseparation in single and coupled MSMPR crystallizers: Experimental validation and parametric simulation study.* (Talk)

Jahrestreffen der Fachgruppe Kristallisation, Münster, Deutschland, 27.-28. März 2014
Eicke MJ, Elsner MP, Lorenz H, Seidel-Morgenstern A. *Optimized Polythermal Operation of Coupled Preferential Crystallization.* (Poster)

Jahrestreffen der Fachgruppen Kristallisation und Mischvorgänge, Magdeburg, Deutschland, 14.-15. März 2013
Eicke MJ, Levilain G, Seidel-Morgenstern A. *Coupling Preferential Crystallization and Selective Dissolution for Efficient Separation of Enantiomers.* (Poster)

12th Annual Meeting American Institute of Chemical Engineers, AIChE 2012, Pittsburg, USA, 28. Oktober-2. November 2012

Eicke MJ, Levilain G, Elsner MP, Seidel-Morgenstern A. *Coupling of crystallizers for efficient enantioseparation – Comparison of two different process strategies.* (Talk)

4th European Congress of Crystal Growth, ECCG-4, Glasgow, Schottland, 17.-20. Juni 2012

Eicke MJ, Hofmann S, Elsner MP, Seidel-Morgenstern A. *Supersaturation control and optimization of polythermal coupled preferential crystallization.* (Talk)

Levilain G, Eicke MJ, Seidel-Morgenstern A. *Resolving enantiomers by a combination of preferential crystallization and dissolution.* (Poster)

Galan K, Eicke MJ, Elsner MP, Seidel-Morgenstern A. *Crystal size distribution shaping by defined temperature trajectories.* (Poster)

18th International Symposium on Industrial Crystallization, ISIC 18, Zürich, Schweiz, 13.-16. September 2011

Eicke MJ, Elsner MP, Seidel-Morgenstern A. *Possibilities and limitations of polythermal coupled preferential crystallization.* (Poster)

10th Annual Meeting American Institute of Chemical Engineers, AIChE 2010, Salt Lake City, USA, 7.-12. November 2010

Eicke MJ, Hofmann S, Raisch J, Elsner MP, Seidel-Morgenstern A. *Separation of enantiomers by coupled preferential crystallization – Impact of initial conditions on the process performance.* (Talk)

4th International Conference on Population Balance Modelling, PBM 2010, Berlin, Deutschland, 15.-17. September 2010

Eicke MJ, Angelov I, Seidel-Morgenstern A, Elsner MP. *Combining polythermal operation and fines destruction to increase the efficiency of simple batch preferential crystallization.* (Poster)

World Congress on Particle Technology, WCPT 6, Nürnberg, Deutschland, 26.-29. April 2010

Hofmann S, Eicke MJ, Elsner MP, Raisch J, Seidel-Morgenstern A. *Innovative Control Strategies for Coupled Preferential Crystallization.* (Poster)

British Association for Crystal Growth, BACG Conference 2009, Bristol, GB, 6.-8. September 2009

Eicke MJ, Seidel-Morgenstern A, Elsner MP. *Polythermal coupled preferential crystallisation (PCPC): An easy and efficient way for the resolution of conglomerates.* (Talk)

9th International Conference on Chemical and Process Engineering, ICheaP-9, Rom, Italien, 10.-13. Mai 2009

Eicke MJ, Seidel-Morgenstern A, Elsner MP. *Effect of fines dissolution on the performance of preferential crystallization for the production of pure enantiomers.* (Talk)

Curriculum vitae

Personal Details

Name	Matthias Johannes Eicke
Date of birth	Hamburg, 09.07.1979
Address	Kirchstr. 21, 37081 Göttingen

Education

08/1989-06/1999	Gymnasium Grootmoor, Hamburg University entrance diploma
07/1995-07/1996	Roane County High School, Spencer, WV, USA University entrance diploma
09/2000-08/2005	University of Applied Sciences, Hamburg Studies of Biotechnology, Dipl.-Ing. (FH)
09/2004-01/2005	École Polytechnique, Montréal, Canada Internship
09/2005-02/2008	University of Applied Sciences, Hamburg Studies of Bioprocess engineering, M.Sc.
since 04-2010	Otto-von-Guericke-University, Magdeburg Ph.D. student

Work experience

06/2008-11/2015	Max-Planck-Institute, Magdeburg
since 05/2016	Sartorius Stedim Biotech GmbH, Göttingen

Scholarships

07/2007	Scholarship of the Max-Buchner-Forschungsstiftung

Göttingen, 06.11.2016